Precision tests of the Standard Model using lattice QCD

Bipasha Chakraborty

School of Physics & Astronomy

A dissertation submitted for the Degree of

Doctor of Philosophy

in the University of Glasgow

June 2016

Abstract

The Standard Model of particle physics successfully describes the fundamental particles and their interactions, but suffers from a few critical limitations which raise the intriguing possibility of new physics beyond it. My dissertation focuses on the study of phenomenologically important quantities in the Standard Model, particularly, involving the high-precision first-principles calculations in the low-energy ($\sim$ 1GeV) regime of Quantum Chromodynamics (QCD), the $SU(3)$ component of the Standard Model. In this regime, since the QCD coupling becomes strong and the quarks and the gluons are confined to bound states called hadrons, a perturbative expansion in the coupling constant is not possible. However, the introduction of a four-dimensional Euclidean space-time lattice allows for an ab-initio treatment of QCD and provides a powerful tool - lattice QCD to study the low energy dynamics of the hadrons using numerical simulations.

I have used existing methods of lattice QCD and developed new methods to study the pseudoscalar and the vector mesons (quark-antiquark hadrons) made of valence light (up and down), strange and charm quarks which are important final states in a number of decay processes that are studied in experiments and are sensitive to new physics. From the large time exponential behaviour of the meson correlators generated on the lattice, I have extracted the masses and the decay constants (annihilation amplitude) of the mesons. My results include the most accurate lattice QCD calculation to date of the properties of the vector mesons ϕ and ρ. In lattice QCD calculations, the

systematic uncertainty coming from the renormalisation constants relating the lattice results to the continuum results can be crucial and therefore I have determined this precisely to test expectations against perturbation theory.

Subsequently, we realised that the vector meson correlators can be used for the calculation of the hadronic vacuum polarisation (HVP) contribution to the anomalous magnetic moment of the muon, a_μ. The anomalous magnetic moment of the muon, shows a large discrepancy ($\sim 3\sigma$) between theoretical and experimental results, putting the Standard Model to one of its most stringent tests. To complement the plans for a four-fold improvement in its experimental uncertainty, this project aims to improve the dominant contributions in the theoretical uncertainty coming from the hadronic vacuum polarisation to $\sim 1\%$. I with my collaborators have developed a new lattice QCD method to calculate the HVP, making a significant progress over previous calculations by achieving an unprecedented precision ($\sim 2\%$) in the total HVP.

The quark flavour sector of the Standard Model is also a fertile ground to test any new physics effect through the Unitarity test of the Cabbibo-Kobayashi-Maskawa (CKM) matrix. Therefore, my aim was to perform a lattice QCD calculation of the scalar and the vector form factors (over a large q^2 region including $q^2 = 0$) associated with the $D \to Kl\nu$ semi-leptonic decay. The central CKM matrix element, V_{cs} in the Standard Model, is then calculated by comparing the lattice QCD results for the form factors and the experimental decay rate.

For my research I have used publicly avalilable MILC HISQ configurations with dynamical up, down, strange and charm quarks. For most of my calculations I have used HISQ valence quarks except for the renormalisation of currents where for the comparison between different lattice formalisms I have also used clover valence quarks.

To my parents, teachers, Niladri, Bidisha and the memories of my late grandparents

Acknowledgements

I will take this opportunity to thank all the people without whom this thesis would not have been possible. At first, I would like to thank my PhD supervisor, Christine Davies, for relying me with extremely important and exciting projects, for guiding me throughout my research and thesis writing, and for all the useful skills I have learnt from her.

I would like to thank Jonna Koponen for her generous help and numerous advice which were extremely useful to build up my research. I would like to thank my collaborators and colleagues in the lattice group, especially, Prof. G. Peter Lepage, Rachel Dowdall, Gordon Donald, Brian Colquhoun, Ben Galloway and Andrew Lytle for their time and patience for numerous Physics discussions. I would like to thank all the members of the PPT group for offering me such an exciting and fun place to work.

I would like to thank Glasgow University IT and administration services for providing me with every help I needed. I would also like to thank Gilmore Bequest for supporting me with a generous scholarship throughout my PhD. I am grateful to the MILC collaboration for making their gauge configurations publicly available which I used in my research. I am also grateful to the Darwin supercomputer service at the University of Cambridge for their smooth running as my entire work has been done using this facility.

I thank my family and friends for providing me with continuous support in this

journey. Especially I thank my parents and sister, Bidisha, who always believed in me and shared my concerns at times. Special thanks go to my husband, Niladri, for always motivating me to pursue a career in Physics and helping me actively throughout my PhD.

Finally, I would like to thank my teachers, especially my Physics teachers, who introduced me to the exciting world of Physics and helped me keep up my passion to pursue it.

Declaration

All work in this thesis was carried out by the author unless otherwise explicitly stated and with the exception of chapters 1 and 2 which contain introductory material.

Contents

List of Tables

List of Figures

Part I

Introduction and basics

Chapter 1

Introduction to lattice QCD

The Standard Model of particle physics is so far the most successful theory to describe the fundamental particles and their interactions. It has been supported by experiments for over four decades. In July, 2012 CERN announced the discovery of a new particle whose properties were in accordance with the Higgs boson, the last missing piece of experimental evidence, and currently all experimental data indicate that the measured particle is indeed the Standard Model Higgs. However, the inability of the Standard Model to explain certain phenomena such as the amount of matter-antimatter asymmetry in the Universe, or the hierarchical values of the masses and coupling strengths of the fermions, has led physicists to design precision tests of the Standard Model in the search for a more fundamental theory beyond it. Deviations from the Standard Model are not only detectable by the discovery of new particles at high energy colliders, but also can be unveiled in the comparison of high precision measurements of low energy ($\sim$ 1 GeV) observables in high luminosity experiments to the theoretical Standard Model predictions for those observables. Given the limitations on available experimental energies, this type of comparison at low energies provides a window through which higher energy phenomena can be glimpsed and new physics can be evidenced even before any new particle discovery in the LHC at CERN.

The Standard Model is mathematically expressed in terms of gauge theories and is represented by the gauge group $SU(3) \times SU(2) \times U(1)$. Separately, the gauge groups $U(1)$ and $SU(2)$ represent the theories of the electromagnetic and the weak interactions respectively and due to the weak couplings these interactions are calculable using the perturbation theory framework. However, the theory of strong interaction, Quantum Chromodynamics (QCD), mathematically represented by a non-abelian Lie group $SU(3)$ shows contrasting features - the coupling strength increases at low energies (~ 1 GeV). Therefore, QCD is only amenable to a perturbative treatment at energies sufficiently high ($\gg 1$ GeV) as the coupling is weak in this region and ultimately for very high energies the quarks are asymptotically free. But in the infrared region (~ 1 GeV), due to the strong self-coupling of the "coloured" gluons, the quarks and the gluons are confined inside the QCD potential to form "colourless" bound states called hadrons. Therefore, in this energy limit, the phenomenon of "colour confinement" makes it impossible to treat QCD perturbatively. We must have mathematically well-defined non-perturbative ways to approach QCD in low energies, the energy region which is very much relevant for different tests of the Stanadrd Model.

Lattice gauge theory, proposed in 1974 by K. Wilson, provides the only successful first-principle non-perturbative method to study QCD at low energies. In this chapter I will discuss about the basics of lattice QCD for which I have consulted a few texts [1–8] with additional references mentioned wherever needed.

1.1 Continuum Quantum Chromodynamics (QCD)

In QCD, the quarks are represented by the elementary matter fields and the gluons, the mediator of the interaction between the quarks, are described by the gauge fields.

The continuum QCD Lagrangian density is given by

$$\begin{aligned}\mathcal{L}_{QCD} &= -\frac{1}{4}F^{(a)}_{\mu\nu}F^{(a)\mu\nu} + i\sum_q \bar{\psi}^i\gamma^\mu(D_\mu)_{ij}\psi^j_q \\ &\quad + \sum_q m_q\bar{\psi}^i_q\psi^i_q \qquad (1.1)\\ F^{(a)}_{\mu\nu} &= \partial_\mu A^a_\nu - \partial_\nu A^a_\mu - g_s f_{abc}A^b_\mu A^c_\nu \qquad (1.2)\\ (D_\mu)_{ij} &= \delta_{ij}\partial_\mu + ig\sum_a \frac{\lambda^a_{ij}}{2}A^a_\mu. \qquad (1.3)\end{aligned}$$

Here, the $\psi^i_q(x)$ represent the quark fields (4-component Dirac spinor) for flavor q and color i, A^a_μ are the gauge fields, g represents the QCD coupling constant, f_{abc} are the structure constants and $\lambda^a_{i,j}$ are the corresponding generators of the $SU(3)$ Lie group. γ_μ are the Dirac matrices satisfying the anti-commutation relation $\{\gamma_\mu, \gamma_\nu\} = 2g_{\mu\nu}$.

The expectation value of any QCD observable $\mathcal{O}$ is given by the following path integral

$$\langle 0|\mathcal{O}|0\rangle = \frac{\int \mathcal{D}\bar{\psi}\mathcal{D}\psi\mathcal{D}A\mathcal{O}e^{iS_{\rm QCD}[\bar{\psi};\psi;A]}}{\int \mathcal{D}\bar{\psi}\mathcal{D}\psi\mathcal{D}Ae^{iS_{\rm QCD}[\bar{\psi};\psi;A]}}. \qquad (1.4)$$

Here, the path integral runs over the fermion and the gauge fields and S_{QCD} is the continuum QCD action corresponding to the QCD Lagrangian in equation 1.1.

1.2 Lattice QCD

The real four dimensional world is a Minkowski one, but QCD is also well defined in Euclidean space assuming it can be analytically continued from real time to the imaginary time. The transformation from Minkowski to Euclidean space is obtained through performing the analytical continuation by using the Wick rotation in the time direction,

$$x_0 \to -ix_4. \qquad (1.5)$$

Such a rotation replaces the oscillating complex exponential in the integration in equation 1.4 by a decaying exponential and thus allows us to use statistical methods to calculate numerically the Green's functions of QCD with a large number of degrees of freedom. Since, a back transformation is not necessarily possible we have to directly extract the results for the physical observables from Euclidean correlators which then hold in Minkowski space too.

The vacuum expectation value for an observable $\mathcal{O}$ (with the spin and the color indices suppressed) in Euclidean space, can be written as

$$\langle 0|\mathcal{O}|0\rangle = \frac{\int \mathcal{D}\bar{\psi}\mathcal{D}\psi\mathcal{D}A\mathcal{O}e^{-S_G^E[A]-S_F^E[\bar{\psi};\psi;A]}}{\int \mathcal{D}\bar{\psi}\mathcal{D}\psi\mathcal{D}Ae^{-S_G^E[A]-S_F^E[\bar{\psi};\psi;A]}} \tag{1.6}$$

where the denominator is for normalisation. $S_G^E[A]$ and $S_F^E[\bar{\psi};\psi;A]$ are the pure gauge and the fermion actions (in Euclidean space) respectively and given by

$$S_G^E[A] = \frac{1}{4}\int d^4x F_{\mu\nu}F^{\mu\nu} \tag{1.7}$$

$$S_F^E[\bar{\psi};\psi;A] = \int d^4x\bar{\psi}\left(\gamma^\mu D_\mu + m\right)\psi. \tag{1.8}$$

In equation 1.6, the path integral is over all possible configurations where each configuration denotes the values of the quark and the gluon fields at all the space-time points in the continuum where the fields are defined. Therefore, solving this path integral in a continuum theory is equivalent to solving an infinite number of integrals. From now on, for Euclidean actions I will drop the superscipt index 'E'.

In lattice QCD, this problem is removed by discretising the QCD action on a hypercubic lattice with sites $x = an$, where a is the lattice spacing and $\mathbf{n} \in \mathbf{Z^4}$. We consider a finite volume four-dimensional space-time lattice of length L on which the gluon fields are placed along the links and the fermions are restricted to the sites. Therefore, the physics we can extract from this lattice will be in the energy scale $1/L$ to $1/a$ which automatically regularises the theory. In our calculation we consider lattices on which $m_\pi L \gg 1$ where m_π is the mass of the lightest propagating particle

in the theory, the pseudoscalar meson π. Note that we usually consider lattices with the same L in three spatial directions and a larger L in the time direction to determine accurately the time dependence of correlation functions.

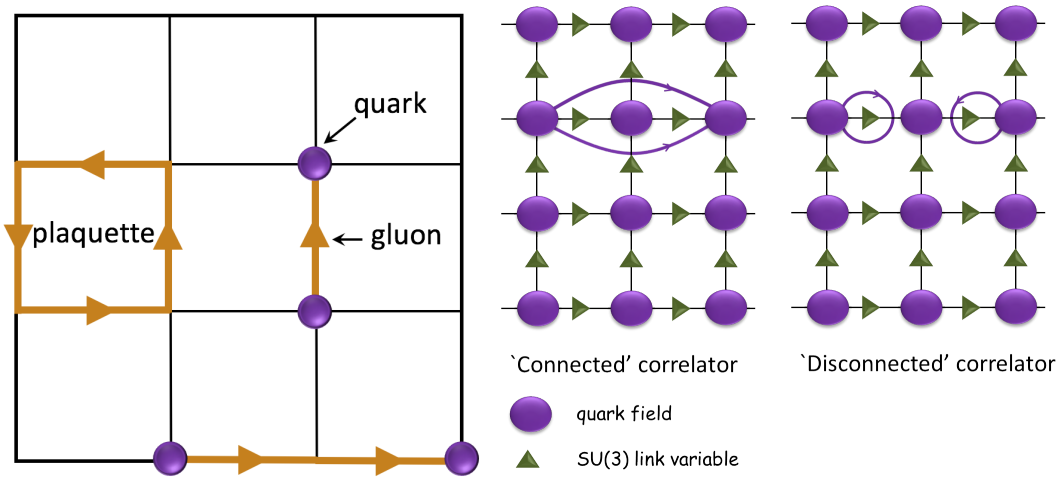

Figure 1.1: The fermions are placed at the sites and gauge field are along the links in a space-time lattice.

1.3 Non-Abelian Gauge Fields on the Lattice

In lattice QCD simulations we need to preserve the characteristics of continuum QCD such as gauge invariance and this can not be done by considering the continuum gauge fields $A_\mu(x)$. Instead the lattice gauge fields are chosen to be a set of $SU(3)$ matrices $U_\mu(x)$ known as the "link" variables connecting x and $x+\hat{\mu}$ in the μ direction where μ can be any of the four space-time directions. These matrices are related to the continuum gauge fields A^b_μ by

$$U(x, x+\hat{\mu}) \equiv U_\mu(x) = e^{iag\lambda^b A^b_\mu\left(x+\frac{\hat{\mu}}{2}\right)} \tag{1.9}$$

and

$$U(x, x-\hat{\mu}) \equiv U_{-\mu}(x) = e^{-iag\lambda^c A^c_\mu\left(x-\frac{\hat{\mu}}{2}\right)} = U^\dagger(x-\hat{\mu}, x). \tag{1.10}$$

Here, a is the distance between two lattice sites or the lattice spacing (assuming homogeneous lattice) and $\hat{\mu}$ is the unit vector along the μ direction.

Now, the pure gauge action can be written in terms of the gauge invariant closed loops of Us. The simplest gauge action is called the "plaquette action" or"Wilson action" and written as

$$S_G = \frac{6}{g^2} \sum_x \sum_{\mu,\nu} \mathrm{Re}\,\mathrm{Tr}\,\frac{1}{3}(1 - W_{\mu\nu}^{1\times1}) \tag{1.11}$$

where g is the bare coupling in the continuum QCD action and the Wilson loop $W_{\mu\nu}^{1\times1}$ or the 1×1 plaquette, is

$$W_{\mu\nu}^{1\times1} = U_\mu(x)U_\nu(x+\hat{\mu})U_\mu^\dagger(x+\hat{\nu})U_\nu^\dagger(x). \tag{1.12}$$

For smooth fields the lattice gauge action in equation 1.11 differs from the continuum action by terms $\sim \mathcal{O}(a^2)$. One can add larger Wilson loops e.g. 2×1 loops of the gauge links with the right coefficients to cancel the $\mathcal{O}(a^2)$ error in equation 1.11. For my calculations I have used publicly available gauge configurations generated by the MILC collaboration which are improved through $\mathcal{O}(\alpha_s a^2)$ [9].

1.4 Fermions on the Lattice

To form the simplest fermion action on the lattice, the continuum derivative in the Dirac action is replaced by symmetrised finite difference with appropriate gauge links inserted to maintain the gauge invariance.

$$\bar{\psi}D\psi = \frac{1}{2a}\bar{\psi}(x)\sum_\mu \left[U_\mu(x)\psi(x+\hat{\mu}) - U_\mu^\dagger(x-\hat{\mu})\psi(x-\hat{\mu})\right] \tag{1.13}$$

where all the variables are dimensionless and constructed from the continuum variables by scaling with a.

$$m_q^{\mathrm{cont}} \rightarrow \frac{1}{a}(m_q a) \tag{1.14}$$

$$\psi^{\mathrm{cont}}(x) \rightarrow \frac{1}{a^{3/2}}\psi(n) \tag{1.15}$$

$$\bar{\psi}^{\mathrm{cont}}(x) \rightarrow \frac{1}{a^{3/2}}\bar{\psi}(n). \tag{1.16}$$

Thus we can construct the following form of the simplest discretised version of the fermion action called the "naive" action.

$$\begin{aligned} S_F^N &= am_q \sum_x \bar{\psi}(x)\psi(x) + \frac{1}{2}\sum_x \bar{\psi}(x)\gamma_\mu \\ &\quad \times \left[U_\mu(x)\psi(x+\hat{\mu}) - U_\mu^\dagger(x-\hat{\mu})\psi(x-\hat{\mu})\right] \qquad (1.17) \\ &\equiv \sum_x \bar{\psi}(x) M_{xy}^N[U]\psi(y). \qquad (1.18) \end{aligned}$$

where the interaction matrix M^N is

$$M_{i,j}^N[U] = am_q\delta_{ij} + \frac{1}{2a}\sum_\mu \left[\gamma_\mu U_{i,\mu}\delta_{i,j-\mu} - \gamma_\mu U_{1-\mu,\mu}^\dagger \delta_{i,j+\mu}\right]. \qquad (1.19)$$

Though the "naive" action preserves the chiral symmetry, it suffers from the "fermion doubling" problem (discussed in the next section) and an $\mathcal{O}(a^2)$ discretisation error in the continuum limit.

The path integral in equation 1.6 is expressed on the lattice in terms of the lattice fields $\psi, \bar{\psi}$ and U. Then, $\int \mathcal{D}[\bar{\psi}, \psi]$ denotes the Grassmann integration over all the colour and the spin components of the fermionic fields at all the lattice points. And

$$\int \mathcal{D}[U] = \int \Pi_x \Pi_\mu dU_\mu(x) \qquad (1.20)$$

stands for the integration over all the link variables with the "Haar measure". Using the correct boundary conditions on the lattice with the rules of Grassmann integration the fermionic part of the path integral can easily be calculated.

$$\int \mathcal{D}[\bar{\psi}, \psi] e^{-S[\bar{\psi},\psi]} = \det M. \qquad (1.21)$$

After performing the Grassmann integral explicitly the path integral becomes

$$\langle \mathcal{O} \rangle = \frac{\int \mathcal{D}[U]\mathcal{O}[M^{-1}[U], U]\det(M[U])e^{-S_G^{\text{latt}}[U]}}{\int \mathcal{D}[U]\det(M[U])e^{-S_G^{\text{latt}}[U]}}. \qquad (1.22)$$

On the lattice the equation 1.22 represents a multi-dimensional integral over real numbers and can be calculated using the numerical techniques of Monte-Carlo integration.

1.4.1 Fermion doubling problem

The naive fermion action has an exact symmetry under the following transformation known as the "doubling transformation":

$$\psi(x) \to \tilde{\psi}(x) \equiv \gamma_{5\rho}(-1)^x_\rho \psi(x) \quad (1.23)$$

$$= \gamma_{5\rho} \exp(ix_\rho \pi)\psi(x). \quad (1.24)$$

Here, ρ denotes any of the space-time directions and $\gamma_{5\rho} = i\gamma_5\gamma_\rho$. The Dirac γ-matrix conventions in Euclidean space are described in section 2.2.1. As a consequence of the symmetry transformation in equation 1.24, any low energy mode $\psi(x)$ of the naive fermion is equivalent to another mode $\tilde{\psi}(x)$ with the maximum allowed momentum on the lattice, π/a. Since the doubling transformation is multiplicative and commutative, in the continuum limit, the "naive" fermion action gives a propagator with $2^4 = 16$ poles for each of the flavours i.e. 16 fermions referred as the "doublers". This is referred by the "fermion doubling problem" and the doublers are referred to as extra "tastes" of the fermions. The "doublers" can be realised by looking at the free fermion propagator in momentum space given by

$$M^{-1} = [i\gamma_\mu \sin(ap_\mu)/a + m]^{-1} \quad (1.25)$$

$$= \frac{-i\gamma_\mu \sin(ap_\mu)/a + m}{\sum_{\mu=0}^{3} \sin^2(ap_\mu)/a^2 + m^2} \quad (1.26)$$

where p_μ is the discretised lattice momentum in the μ direction and lies between $-\frac{\pi}{a}$ and $\frac{\pi}{a}$. Therefore the lattice fermion momenta are restricted to the periodic Brillouin zone which is a 4D torus.

In equation 1.26, the sinusoidal functions vanish at the 16 points in a Brillouin zone assigned by the following momenta $p^{(1)} = (0,0,0,0)$, $p^{(2)} = (\pi,0,0,0)$, ..., $p^{(16)} = (\pi,\pi,\pi,\pi)$. Therefore, we get the continuum limit ($a \to 0$) of the equation 1.26 by expanding its right hand side in a Taylor series around those momenta given by $p = p^{(n)} + k$, where k is an integral multiple of $2\pi/a$. This gives,

$$M^{-1}(p) = \frac{-i\gamma_\mu^{(n)} k_\mu + m}{k^2 + m^2} + O(a^2). \quad (1.27)$$

Here, $\gamma_\mu^{(n)} = \pm\gamma_\mu$.

It shows that in the continuum a naive fermion with momenta close to the maximum momenta allowed on the lattice gives rise to a total of sixteen low energy tastes of the fermion.

1.4.2 Wilson Fermions

To remove the doublers, Wilson's solution was to add a dimension five operator $ar\bar{\psi}\Box\psi$ to the "naive" fermion action and thus to give infinitely heavy mass to the extra fifteen "taste" species in the continuum limit such that they decouple. Accordingly, the Wilson fermion action is written as [10]

$$\begin{aligned}
S_F^W &= m_q \sum_x \bar{\psi}(x)\psi(x) \\
&+ \frac{1}{2a}\sum_{x,\mu} \bar{\psi}(x)\gamma_\mu \left[U_\mu(x)\psi(x+\hat{\mu}) - U_\mu^\dagger(x-\hat{\mu})\psi(x-\hat{\mu})\right] \\
&- \frac{r}{2a}\sum_{x,\mu} \bar{\psi}(x)\gamma_\mu \left[U_\mu(x)\psi(x+\hat{\mu}) - 2\psi(x) - U_\mu^\dagger(x-\hat{\mu})\psi(x-\hat{\mu})\right] \quad (1.28) \\
&= \frac{(m_q a + 4r)}{a}\sum_x \bar{\psi}(x)\psi(x) + \frac{1}{2a}\sum_{x,\mu}\bar{\psi}(x) \\
&\quad \times \left[(\gamma_\mu - r)U_\mu(x)\psi(x+\hat{\mu}) - (\gamma_\mu + r)U_\mu^\dagger(x-\hat{\mu})\psi(x-\hat{\mu})\right] \quad (1.29) \\
&\equiv \sum_{x,y} \bar{\psi}_x M_{xy}^W \psi_y. \quad (1.30)
\end{aligned}$$

The interaction matrix M^W is written as

$$M_{x,y}^W[U] = \delta_{xy} - \kappa\sum_\mu \left[(r-\gamma_\mu)U_{x,\mu}\delta_{x,y-\mu} + (r+\gamma_\mu)U_{x-\mu,\mu}^\dagger\delta_{x,y+\mu}\right] \quad (1.31)$$

with the rescaling

$$\begin{aligned}
\kappa &= \frac{1}{(2m_q a + 8r)} \quad (1.32) \\
\psi^L &= \sqrt{m_q a + 4r}\,\psi = \psi/\sqrt{2\kappa}. \quad (1.33)
\end{aligned}$$

The quark mass on the lattice can be given in terms of the lattice parameter κ as

$$m_q a = \frac{1}{2}\left[\frac{1}{\kappa} - \frac{1}{\kappa_c}\right] \quad (1.34)$$

where κ is called the "hopping parameter" and the "critical hopping parameter" is $\kappa_c = 1/(8r)$. This means that in free theory the quark mass becomes zero at the critical value of the hopping parameter κ_c. However, κ_c depends on the lattice spacing a in case of an interacting theory where $U_\mu(x) \neq 1$.

The dimension five operator i.e. the term proportional to r in the Wilson fermion action explicitly breaks the chiral symmetry at $\mathcal{O}(a)$, but removes the doublers. Due to the addition of a term proportional to 'r' with the mass term, the quark mass contains an additive renormalisation along with the usual multiplicative renormalisation. This is implied by the fact that the renormalisation of κ_c does not depend on the renormalisation of κ. There are a lot of ways to remove $\mathcal{O}(a)$ discretisation errors without spoiling Wilson's fix for the doublers. One such remedy is the construction of the clover lattice fermion action.

1.4.3 The Sheikholeslami-Wohlert (Clover) Fermions

The clover action was proposed by Sheikholeslami-Wohlert [6] to remove the $\mathcal{O}(a)$ artifacts in the Wilson fermion action S_{W} without spoiling Wilson's fix for the doublers by adding another dimension five operator, the magnetic moment S_{W}. And the resulting clover action is

$$S_{\mathrm{SW}} = S_{\mathrm{W}} - \frac{iaC_{\mathrm{SW}}\kappa r}{4}\bar{\psi}(x)\sigma_{\mu\nu}F_{\mu\nu}\psi(x). \tag{1.35}$$

The clover coefficient C_{SW} can be calculated using perturbative or nonperturbative techniques. For my project, I have been using the tadpole-improved clover action with $C_{\mathrm{SW}} = \frac{1}{u_0^4}$ where the tadpole factor u_0 is chosen to be the fourth root of the plaquette. In this case, the quark mass on the lattice can be written as:

$$m_q a = \frac{1}{u_0}\left(\frac{1}{\kappa} - \frac{1}{\kappa_c}\right). \tag{1.36}$$

1.4.4 Staggered fermions

Staggering the "naive" fermion action by the trick of spin-diagonalisation [11] can reduce the sixteen-fold doubling problem to four. The staggered fermion fields $\chi(x)$ are defined by the local transformation

$$\begin{aligned} \psi(x) &= \Omega(x)\chi(x) && (1.37)\\ \bar{\psi}(x) &= \bar{\chi}(x)\Omega^{\dagger}(x) && (1.38) \end{aligned}$$

known as the "staggering" transformation. Here each component of $\chi(x)$ is exactly equivalent to every other component. And,

$$\Omega(x) = \gamma_4^{x_4}\gamma_1^{x_1}\gamma_2^{x_2}\gamma_3^{x_3}. \tag{1.39}$$

Here, the γ matrices have been applied at the lattice site x whose space-time coordinates are described by x_1, x_2, x_3, x_4. This gives

$$\begin{aligned} 1 &= \Omega^{\dagger}(x)\Omega(x), && (1.40)\\ \alpha_\mu(x) &= \Omega^{\dagger}(x)\gamma_\mu\Omega(x \pm \vec{\mu}) && (1.41)\\ &= (-1)^{x_\mu^<} && (1.42) \end{aligned}$$

where

$$x_\mu^< = x_0 + x_1 + ... + x_{\mu-1}. \tag{1.43}$$

In terms of $\chi(x)$ the fermion action can be written as

$$\begin{aligned} S_F^S &= am_q\sum_x \bar{\chi}(x)\chi(x) + \frac{1}{2}\sum_{x,\mu}\bar{\chi}_x\eta_{x,\mu}\left(U_{\mu,x}\chi_{x+\hat{\mu}} - U^{\dagger}_{\mu,x-\hat{\mu}}\chi_{x-\hat{\mu}}\right) && (1.44)\\ &\equiv \sum_{x,y}\bar{\chi}(x)M^S_{xy}\chi(y) && (1.45) \end{aligned}$$

with the matrix M^S given by

$$M^S_{x,y}[U] = am_q\delta_{xy} + \frac{1}{2}\sum_\mu \eta_{x,\mu}\left[U_{x,\mu}\delta_{x,y-\mu} - U^{\dagger}_{x-\mu,\mu}\delta_{x,y+\mu}\right]. \tag{1.46}$$

The fermion action has now been diagonalised in the spin space as all components of $\chi(x)$ are equivalent to each other. Here, the γ matrices are replaced by the phases

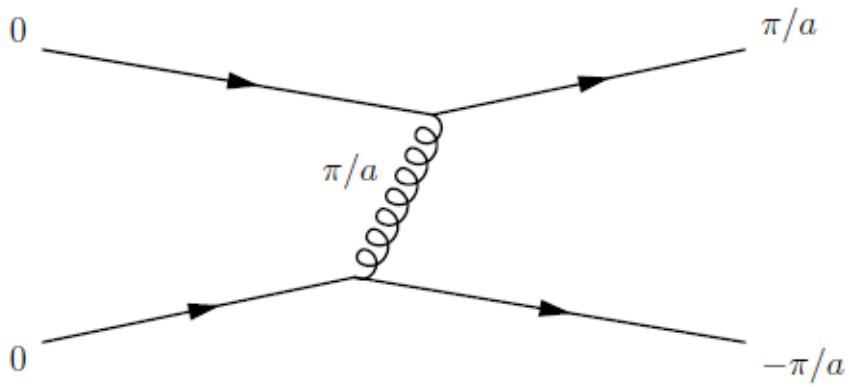

Figure 1.2: This plot depicts the taste-changing interaction; a gluon with a momentum π/a is emitted by one low energy quark and absorbed by another, therefore both the quarks get tastes changed in this interaction.

$\eta_{x,\mu} = (-1)^{\sum_{\nu<\mu} x_\nu}$. Since these phases depend only on the site indices and the direction and do not have a spinor index, the different spin components of $\chi(x)$ are decoupled. Due to these phase factors, the staggered action has translational invariance under the shift by $2a$. Thus, in the continuum limit, a 2^4 hypercube is mapped to a single point and the sixteen "taste" degrees of freedom reduces to four. Though the staggered fermion action preserves chiral symmetry, this formalism suffers from $\mathcal{O}(a^2)$ discretisation errors at the tree level due to the discretisation of the derivative in the action and the taste-exchange interactions.

By adding a correction term $\sim a^2$, called the "Naik term", to the derivative in the staggered action, the finite difference approximation can be corrected [12]

$$\Delta_\mu \longrightarrow \Delta_\mu - \frac{a^2}{6}\Delta_\mu^3. \tag{1.47}$$

The Symanzik improvement procedure removes the taste-exchange interactions (depicted in Figure 5.1) in the staggered quarks at the lowest order in the perturbation theory. In this procedure the the gauge link between two consecutive lattice sites is replaced by a fattened link which includes a combination of 3-link, 5-link and 7-link paths (shown in Figure 1.3) [13–16]. In effect, the gluon-quark vertex $\bar{\psi}\gamma_\mu U_\mu \psi + ...$, in the original action, is modified by a form factor $f_\mu(q)$ that vanishes for the taste-changing

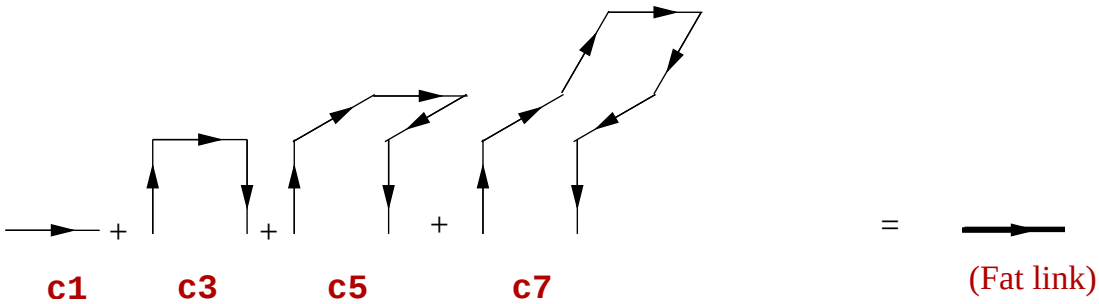

Figure 1.3: Fat link smearings to remove the taste-change interactions in the staggered quark action needed to form the Asqtad action - 1-link, 3-link, 5-link and 7-link path (from left to right).

gluons. Such a form factor can be introduced in the action by replacing the links $U_\mu(x)$ with fattened links $\mathcal{F}_\mu U_\mu(x)$ where $\mathcal{F}_\mu$ is the smearing operator defined by

$$\mathcal{F}_\mu = \prod_{\rho\neq\mu}\left(1+\frac{a^2\delta_\rho^{(2)}}{4}\right)\Big|_{\rm symm}. \tag{1.48}$$

Here $\delta_\rho^{(2)}$ works as an approximation to the covariant derivative and gives

$$\begin{aligned}\delta_\rho^{(2)}U_\mu(x) &\equiv \frac{1}{a^2}\left(U_\rho(x)U_\mu(x+a\hat{\rho})U_\rho^\dagger(x+a\hat{\mu})-2U_\mu(x)\right)\\ &+ \frac{1}{a^2}U_\rho^\dagger(x-a\hat{\rho})U_\mu(x-a\hat{\rho})U_\rho(x-a\hat{\rho}+a\hat{\mu}).\end{aligned} \tag{1.49}$$

This kind of link smearing is known as the "Fat 7" smearing. However, this kind of link smearing gives rise to additional lattice artifacts. To remove the artifacts additional 5-link term, known as "Lepage term" [15]-

$$\mathcal{F}_\mu^{\rm Asqtad} = \mathcal{F}_\mu - \sum_{\rho\neq\mu}\frac{a^2(\delta_\rho)^2)}{4} \tag{1.50}$$

is included in the smearing, where

$$\begin{aligned}&\delta_\rho U_\mu(x)\\ \equiv\ &\frac{1}{a}\left(U_\rho(x)U_\mu(x+\hat{\rho})U_\rho^\dagger(x+\hat{\mu})-U_\rho^\dagger(x-\hat{\rho})U_\mu(x-\hat{\rho})U_\rho(x-\hat{\rho}+\hat{\mu})\right).\end{aligned} \tag{1.51}$$

This results in what is known as the "Asqtad" (a^2 tadpole improved) action given by

$$S^{\rm Asqtad} = \sum_i \bar{\psi}(i)[\gamma_\mu(\Delta_\mu(V)-\frac{1}{6}\delta_\mu^3(V))+m]\psi(i) \tag{1.52}$$

where

$$V_\mu(x) = F_\mu^{\text{Asqtad}} U_\mu(x). \tag{1.53}$$

However, it is not sufficient to just remove the $\mathcal{O}(\alpha_s)$ taste-changing errors. We need to suppress the one-loop errors too as they become important in the study of the heavy quarks. Multiple smearings of the links guarantee suppression of the one-loop correction to the taste-change interactions, but introduce new $\mathcal{O}(a^2)$ discretisation errors which grow with additional smearings and lead to a huge growth in the size of the two-gluon vertices. To remove these problems while removing the taste-change interactions from the one-loop, one uses the re-unitarised doubly smeared link operator given as

$$\begin{aligned} U_\mu(x) \quad &\longrightarrow \quad \left(\mathcal{F}_\mu - \sum_{\rho \neq \mu} \frac{a^2 (\delta_p)^2}{2} \right) \mathcal{U} \mathcal{F}_\mu U_\mu(x) && (1.54) \\ &\equiv \quad \mathcal{F}_\mu^{\text{HISQ}} U_\mu(x) && (1.55) \end{aligned}$$

where the operator $\mathcal{U}$ unitarizes whatever it is applied on.

Therefore, the new "Highly Improved Staggered Quark (HISQ)" discretisation [17] of the fermion action is

$$\sum_x \bar{\psi}(x)(\gamma.\mathcal{D}^{\text{HISQ}} + m)\psi(x) \tag{1.56}$$

where

$$\begin{aligned} \mathcal{D}^{\text{HISQ}} &\equiv \Delta_\mu(W) - \frac{a^2}{6}(1+\epsilon)\Delta_\mu^3(X) && (1.57) \\ & && (1.58) \end{aligned}$$

with

$$\begin{aligned} W_\mu(x) \quad &\equiv \quad \mathcal{F}_\mu^{\text{HISQ}} U_\mu(x) && (1.59) \\ X_\mu(x) \quad &\equiv \quad \mathcal{U} \mathcal{F}_\mu U_\mu(x). && (1.60) \end{aligned}$$

In Chapter 3, I will show in comparison with the clover action, how small discretisation errors are from the HISQ action. In Chapter 4, I will compare some results from

another lattice collaboration, European Twisted Mass, to show further how using the HISQ action we have a much smaller discretisation error in compared to their twisted-mass formalism [18].

Chapter 2

Lattice formulation with staggered quarks

In this chapter I will discuss some details about a practical calculation of important hadronic quantities (in this case, mesonic quantities). I have referred to a few books and articles [1–7, 11, 19–21] to prepare this chapter of my dissertation with additional references mentioned wherever appropriate.

Any standard lattice calculation to extract expectation values of mesonic observables involves the following few steps.

2.1 Generation of the gauge field configurations

The numerical simulation starts from generating a large number (~ 1000) of independent gauge configurations in a Monte-Carlo process. The gauge configurations include the background gauge fields with the effect of dynamical quarks embedded in them. The starting point is to explicitly perform the Grassmann integration over the fermion fields in the equation 1.22. The i-th gauge configuration is generated with the

probability density

$$p[U_i] \propto (\Pi_f \det M_f[U_i]) e^{-S_G[U_i]} \tag{2.1}$$

for a large ensemble, where M_f is the lattice fermion action for a flavor f of the dynamical quarks. To obtain the expectation value of an observable the gauge configurations are averaged over. Updating the gauge fields in the Markov process requires an iterative solution for an equation involving the fermion action which makes the inclusion of the dynamical quarks in the simulation expensive. Therefore, sometimes for less expensive calculations, the determinant of the fermion action is taken as a constant (preferably, 1) and the effects of the dynamical quarks are neglected which is known as the "quenched approximation". However, the exclusion of the dynamical quarks leads to large systematic uncertainties.

For this dissertation, I have used publicly available gauge configurations generated by the MILC collaboration [22] using the one-loop Symanzik Improved gauge action [23] and the HISQ [17] fermion action. These ensembles include the effects of up, down, strange and charm dynamical quarks though the masses of up/down (light) quarks are taken to be the same ($N_f = 2 + 1 + 1$). The MILC configurations have three major characteristics that make them excellent- huge statistics, dynamical quarks at physical masses and vacuum polarisation effects from the c quarks included. I have mainly used three lattice spacings $a \sim 0.09$ fm (fine), ~ 0.12 fm (coarse) and ~ 0.15 fm (very coarse) for my projects (not all of them for all calculations; particular cases will be discussed separately). The lattice spacings have been set using the Wilson flow parameter w_0 [24, 25]. Also, on each lattice spacing I have used the light quark masses down to the physical one ($m_l \equiv m_u = m_d \simeq m_s/27$) and up to $m_l = 0.2m_s$ and multiple volumes at one particular m_l and a. The details of these gauge configurations are depicted in Figure 2.1 and are described in Table 2.1.

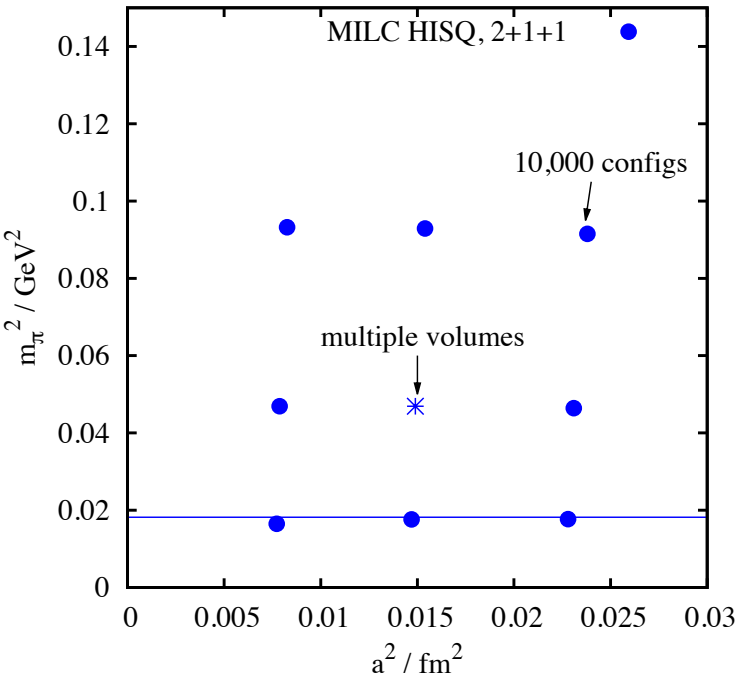

Figure 2.1: This plot depicts the MILC HISQ $N_f = 2 + 1 + 1$ ensembles used in my calculations; the horizontal axis shows the square of the lattice spacings used and the vertical axis gives the square of the pion masses which are proportional to the dynamical light quark (up/down) masses used in the simulation.

2.1.1 Autocorrelation

While generating the gauge configurations, to get the equilibrium distribution of independent ensembles, one has to take care of the "thermalisation" to achieve equilibrium in the Monte-Carlo process. This affects the beginning of the Monte-Carlo chain and cuts-off some starting configurations. Another important aspect affecting reliable calculations is the presence of "autocorrelation" among the configurations. By definition, the "autocorrelation" is the correlation of a given time series r_t with itself at a time separation T, given by the following equation

$$R(T) = \frac{\langle (r_t - \langle r_t \rangle)(r_{t+T} - \langle r_{t+T} \rangle) \rangle}{\langle r_t \rangle \langle r_{t+T} \rangle}. \tag{2.2}$$

In any stationary random process we expect the autocorrelations to fall off exponentially with T/τ, $R(T) \sim e^{-T/\tau}$ where τ is known as the "autocorrelation time" which is

Table 2.1: Sets of MILC configurations used here with their $\beta = 6/g^2$ [22], w_0/a for $w_0 = 0.1715(9)$ fm fixed from f_π [25] (w_0/a values were determined by Craig McNeile), L_s/a, L_t/a, (HISQ) sea quark masses- m_l, m_s and m_c in lattice units [22].

Set	β	w_0/a	L_s/a	L_t/a	$N_{\rm conf}$	$am_l^{\rm sea}$	$am_s^{\rm sea}$	$am_c^{\rm sea}$
1	5.8	1.1119(10)	16	48	9947	0.01300	0.0650	0.838
2	5.8	1.1272(7)	24	48	1000	0.00640	0.0640	0.828
3	5.8	1.1367(5)	36	48	997	0.00235	0.0647	0.831
4	6.0	1.3826(11)	24	64	1053	0.01020	0.0509	0.635
5	6.0	1.4029(9)	24	64	1020	0.00507	0.0507	0.628
6	6.0	1.4029(9)	32	64	1000	0.00507	0.0507	0.628
7	6.0	1.4029(9)	40	64	331	0.00507	0.0507	0.628
8	6.0	1.4149(6)	48	64	998	0.00184	0.0507	0.628
9	6.3	1.9006(20)	32	96	1000	0.0074	0.037	0.44
10	6.3	1.9330(20)	48	96	1000	0.00363	0.0363	0.430
11	6.3	1.9518(7)	64	96	660	0.00120	0.0363	0.432

different for different observables. The autocorrelation among the gauge configurations can be reduced by blocking the series and averaging over the configurations in a block. The autocorrelation is not a significant issue in my calculations as I have not used finer than ~ 0.09 fm lattices and this has been tested in references [26, 27].

2.1.2 Rooted staggered dynamical quarks

As previously discussed, the staggered quark action gives rise to four different tastes of the quarks, which is also true for the dynamical quarks. This adds more complication in simulating the fermion determinant as the effect of multiple tastes has to be considered. To eradicate the extra three tastes, it is a practice to take the fourth-root of the fermion determinant which is known as "rooting".

The fermion matrix M in the presence of the taste-changing interactions is a 4×4 matrix in the taste-space. The justification of the rooting comes from the fact that in the continuum limit the tastes should represent the same fermion and for the improved staggered quarks the taste-changing interactions are small. Under these conditions, the fermion matrix M is diagonal in taste-space with all the diagonal elements the

same, and represented as

$$M = \begin{bmatrix} M_1 & 0 & 0 & 0 \\ 0 & M_1 & 0 & 0 \\ 0 & 0 & M_1 & 0 \\ 0 & 0 & 0 & M_1 \end{bmatrix} \tag{2.3}$$

so that

$$\sqrt[4]{\det M} = \det(M_1). \tag{2.4}$$

There have been numerous tests that show the staggered quarks work as expected [17, 28, 29].

2.2 Choice of the lattice fermion action and the operators

I have used the relativistic Highly Improved Staggered Quark (HISQ) action to describe all the dynamical and the valence quark flavours in my simulations. Using staggered quarks has its advanteges - reducing the number of the "tastes" to four, with added bonus of having a remnant chiral symmetry which forbids the generation of an additive mass renormalisation. Another reason for low-cost simulations is, of course, that we deal with one spinor component here instead of four. In Chapter 3 I will compare the HISQ action with an unstaggered quark action, clover, by studying some of the properties of the vector meson ϕ.

2.2.1 Point-split operators

All the four staggered tastes propagate in the staggered quark loop. To form a meson we need to choose the staggered operators carefully such that all the γ matrices cancel out to give an overall ± 1 phase in front of the staggered correlator. Therefore, sometimes we need to use non-local meson operators, for example, point-split operators

which uses gauge links to connect two different lattice sites. The gauge links in the operator are gauge-fixed in the MILC code (Coulomb gauge, in our case), although the operators are gauge-invariant.

The spin of the operator, γ_n determines what J^{PC} it couples to and the total γ matrix content representing the staggering transformation is given by the taste operator γ_s. γ_n represents the complete set of spinor matrices given by

$$\gamma_n \equiv \prod_{\mu=0}^{3} (\gamma_\mu)^{n_\mu} \tag{2.5}$$

where $n_\mu = x_\mu \mathrm{mod} 2$ and x_μs are the space-time indices of the lattice site x. Similarly, γ_s can be any of the γ_ns with or without implicit gauge links representing point-split operators and local operators respectively. The spin-taste operator for the staggered quark is represented by $\gamma_n \otimes \gamma_s$[1].

We have used the Dirac γ matrices with the following convention

$$\gamma_t = \begin{bmatrix} 1 & 0 \\ 0 & -1 \end{bmatrix}; \qquad \gamma_i = \begin{bmatrix} 0 & \sigma_i \\ \sigma_i & 0 \end{bmatrix}. \tag{2.6}$$

The Dirac matrices are traceless and satify the following properties.

$$\gamma_\mu^\dagger = \gamma_\mu, \tag{2.7}$$
$$\gamma_\mu^2 = 1, \tag{2.8}$$
$$\{\gamma_\mu, \gamma_\nu\} = 2\delta_{\mu\nu}, \tag{2.9}$$
$$\gamma_5^2 = 1 \tag{2.10}$$

where

$$\gamma_5 = \gamma_4\gamma_1\gamma_2\gamma_3. \tag{2.11}$$

From equation 2.8, we get

$$\Omega(i + 2\hat{\mu}) = \Omega(i) \tag{2.12}$$

for any direction $\hat{\mu}$. This means the staggering transformation depends only on the site and whether it is an even or odd site.

[1]The notation $\otimes$ is only used as a notation here and does not represent an outer product. Also, the two matrices γ_n and γ_s act on two different spaces and they remain decoupled.

2.3 Generation of quark propagators

I have used publicly available MILC codes (versions 7.7.5, 7.7.10, 7.7.10*a* and 7.7.11) to calculate the lattice propagators, specifically using the *KS_spectrum* application to handle the HISQ quarks and *clover_invert2* to handle the clover quarks. MILC uses the γ_5 diagonal Weyl basis of the γ matrices and its sign convention of γ_2 is minus the standard convention along with the opposite convention for the projectors. This gives,

$$\psi_{\text{MILC}} = \gamma_5 \psi_{\text{usual}}. \tag{2.13}$$

The mesons are generated combining a quark propagator and an antiquark propagator, which we obtain by starting from a source (say η). Then we solve the inhomogeneous Dirac equation: $Mx = \eta$ with certain boundary conditions using the Congugate Gradient (CG) [30] method. There are a wide variety of options for the source in the MILC code. The propagators are generated in a succession of steps- defining a base source and then modifying it with appropriate source operators to achieve the correct source interpolating operator. It is followed by the inversion of the many-millions by many-millions fermion matrix ($2 \times 2\times$ spin indices $\times$ color indices $\times$ spatial indices $\times$ time indices) such that the propagator started from the source propagates to the sink point. At the end appropriate operators are multiplied at the sink to achieve the correct sink interpolation operator and a complete correlator.

Since, the staggered fermion field $\chi(x)$ is diagonal in spin space, we have

$$\chi(x)\bar{\chi}(y) = g(x,y)\mathbf{1}_{\text{spinor}}, \tag{2.14}$$

where $g(x,y)$ is the staggered fermion propagator with one-spinor component.

Relating the staggered fermion propagator with to naive fermion propagator we have

$$\langle \psi(x)\bar{\psi}(y)\rangle_\psi = g(x,y)\Omega(x)\Omega^\dagger(y). \tag{2.15}$$

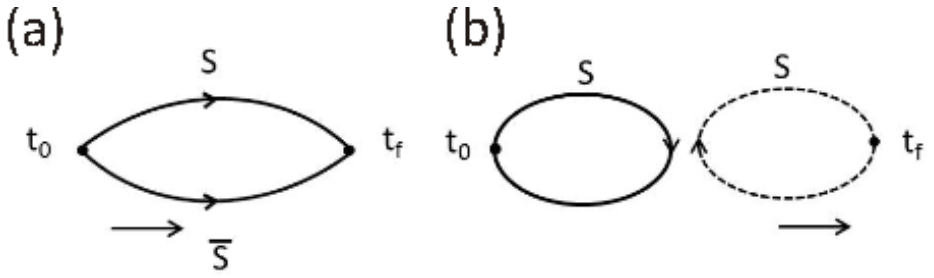

Figure 2.2: Two-point meson correlators: a) quark-line connected, b) quark-line disconnected.

This result indicates the complete gauge field independence of the naive-quark spinor structure. For naive quarks, if the quark propagator from x to y is denoted by $G(x, y)$ then the antiquark propagator from x to y is expressed as $\gamma_5 G^\dagger(x, y)\gamma_5$. For the staggered quarks, if $g(x, y)$ denotes the quark propagator from point x to y, then the antiquark propagator from x to y is denoted by $(-1)^{\sum_\mu y_\mu} gg^\dagger(x, y)$. Here, y_μ denotes the site index at point y for a direction μ.

2.4 Computation of the correlation functions

This step involves combining the appropriate quark propagators and other structures in spin-space to form the optimal mesonic correlation functions corresponding to the particles and the matrix elements which are being studied.

2.4.0.1 Two-point meson correlation function

Different topologies of the quark paths between the source and the sink give rise to two kinds of diagrams (not Feynman diagrams) for the two point correlation function (depicted in Figure 2.2): the quark-line connected and the quark-line disconnected diagrams. The disconnected diagrams are only obtained for flavour singlet mesons. A general (naive) two-point meson correlator can be written as the expectation value

of the product of the meson interpolating fields $\phi_B(x)$ and $\bar{\phi}_A(x_0)$ i.e.

$$G^{2\mathrm{pt}}_{BA}(t;\vec{p}) \;=\; \sum_x e^{-i\vec{p}.(\vec{x}-\vec{x_0})}\langle 0|\phi_B(x)\bar{\phi}_A(x_0)|0\rangle \tag{2.16}$$

Here, $\bar{\phi}_A(x_0)$ creates a meson at the lattice site A represented by the space-time indices x_0, then the meson propagates to the lattice site B represented by the space-time indices x; at B the meson is annihilated with the field $\phi_B(x)$.

In case of mesons, the interpolating operators are given by

$$\phi_B(x) \;=\; \bar{\psi}_2(x)\Gamma_B\psi_1(x) \tag{2.17}$$
$$\bar{\phi}_A(x_0) \;=\; \bar{\psi}_1(x_0)\Gamma_A\psi_2(x_0). \tag{2.18}$$

And the two-point correlator in terms of the fermionic fields can be written as

$$\begin{aligned} & G^{2\mathrm{pt}}_{BA}(t;\vec{p}) \\ =\; & \sum_x e^{-i\vec{p}.(\vec{x}-\vec{x_0})}\langle\bar{\psi}_2(x)\Gamma_B\psi_1(x)\bar{\psi}_1(x_0)\Gamma_A\psi_2(x_0)\rangle & (2.19)\\ =\; & \sum_x e^{-i\vec{p}.(\vec{x}-\vec{x_0})}\langle(\bar{\psi}_2(x))^a(\Gamma_B)^{ab}(\psi_1(x))^b(\bar{\psi}_1(x_0))^c(\Gamma_A)^{cd}(\psi_2(x_0))^d\rangle. & (2.20)\end{aligned}$$

We get the equation by writing it as a matrix multiplication, where summations over all matrix indices, 'a,b,c,d' are implied. Now by rearranging the matrix elements we can write

$$\begin{aligned} & G^{2\mathrm{pt}}_{BA}(t;\vec{p}) \\ =\; & \sum_x e^{-i\vec{p}.(\vec{x}-\vec{x_0})}\langle(\psi_2(x_0))^d(\bar{\psi}_2(x))^a(\Gamma_B)^{ab}(\psi_1(x))^b(\bar{\psi}_1(x_0))^c(\Gamma_A)^{cd}\rangle & (2.21)\\ =\; & \sum_x e^{-i\vec{p}.(\vec{x}-\vec{x_0})}\langle {S_2}^{da}(x_0,x)(\Gamma_B)^{ab}{S_1}^{bc}(x,x_0)(\Gamma_A)^{cd}\rangle. & (2.22)\end{aligned}$$

Here, S_1 and S_2 are naive quark propagators, related to staggered quarks propagators by equation 2.15.

Equation 2.22 now generates a trace over the colours and the spins and can be written as (for simplicity, take $x_0 = 0$ as the correlators are invariant with respect to translation)

$$G^{2\mathrm{pt}}_{BA}(t;\vec{p}) \;=\; -\sum_x e^{-i\vec{p}.\vec{x}}\langle \mathrm{Tr}\,(S_2(0,x)\Gamma_B S_1(x,0)\Gamma_A)\rangle \tag{2.23}$$

Equation 2.19 generates only the connected correlator $C^{\rm 2pt}_{\rm BA}(t;\vec{p})$ if $\psi_1(x) \neq \psi_2(x)$ i.e. the two quark flavours are different. Otherwise, the equation 2.19 can be Wick-contracted to give the disconnected correlator as well which can be written as

$$D^{\rm 2pt}_{BA}(t;\vec{p}) = -\sum_x e^{-i\vec{p}.\vec{x}} \langle {\rm Tr}\left(S_2(0,0)\Gamma_B\right) {\rm Tr}\left(S_1(x,x)\Gamma_A\right)\rangle. \tag{2.24}$$

For staggered quarks we can make a correlator with local operators only if $\Gamma_A = \Gamma_B = \Gamma$, where Γ is any local operator. We can use different Γ_A and Γ_B if one of them is non-local, for example, point-split operators. For the correlators made from staggered quarks the spin part gives only a phase factor depending on the site.

Since staggered quark loops carry four tastes, they have to be divided by a factor of 4 before any analysis is performed. Also, in our calculations, for each staggered propagator, the correlator is multiplied by a factor of 2 as the MILC code has a factor of 2 missing from the symmetric finite difference operator in the HISQ action, so all the propagators are a factor of 2 too large. The 2 factors cancel with the inverse of number of taste in a meson correlation function made of staggered quark and antiquark.

2.4.1 The staggered operator phases

The correlation function using staggered quarks needs to have a total taste 1 i.e. when written in terms of naive quarks the γ matrix trace is not zero. That is achieved by choosing appropriate spin-taste operators at the source and the sink. The spin part of the staggered quark correlator gives an overall position-dependent phase which can be calculated systematically by the Wick-contraction and taking γ matrix traces for the naive correlator.

For example, the local pion (or any local pseudoscalar Goldstone meson) correlator is generated by tying two propagators, both of which are generated with a $\gamma_5 \otimes \gamma_5$

source operator. In the naive quark basis this correlator becomes

$$\langle J_5(x)J_5(0)\rangle = 4\mathrm{Tr}(|g(x,0|^2) \tag{2.25}$$

where the trace is on colours; $g(x,0)$ is the staggered quark propagator from x to 0 and the overall phase of the correlator is positive with no position dependence.

For the local ρ meson (or any local vector meson) using $\gamma_i \otimes \gamma_i$ operator, the staggered quark correlator becomes

$$\langle J_i(x)J_i(0)\rangle = 4(-1)^{x_i}\mathrm{Tr}(|g(x,0|^2). \tag{2.26}$$

For calculating the disconnected diagrams for the vector meson (flavour singlet vector meson) we have to use the one-link point-split vector as it is the taste-singlet operator in this case. The connected correlator made from $\gamma_i \otimes 1$ gives an overall phase $(-1)^{\sum_\mu (x_\mu + i)}$ in the MILC code, whereas the disconnected correlator gives an overall phase of $(-1)^{x_\mu^<}$. $x_\mu^<$ has been defined in equation 1.43. μ represents the direction of the link in the point-split operator and ν represents all space-time directions with indices smaller than μ.

2.4.2 Random wall source

As previously mentioned, the inverter for the fermion matrix solves an inhomogeneous Dirac equation: $Mx = \eta$ for $x(j)$ where M is the fermionic matrix $M(i,j)$ and $\eta(i)$ is the source vector. The solution

$$x(j) = \sum_i g(i,j)\eta_i \tag{2.27}$$

describes the fermion propagation from all points i (source) to any point j (sink) on the lattice with $g(i,j)$ as the inverse fermion matrix or the propagator. The simplest source used in the simulation is a point source, which is basically a delta function at one point on one time slice t_0/a on the lattice. For increased statistics, I have used a random color wall source [31, 32] which is spread over all the sites on a single

time slice (equivalent to $(L/a)^3$ number of point sources). Furthermore, multiple such independent time slices have been used to improve the statistics.

The random wall source at the time slice t_0/a is defined as

$$\eta(i_t) = \begin{cases} e^{i\theta} & \text{for } i_t = t_0, \\ 0 & \text{for } i_t \neq t_0. \end{cases}$$

where θ is a uniform random phase. That means, the random colour wall is a random number with modulus one for each colour for each site on a time-slice.

Using the random wall source with staggered quarks, the correlator becomes

$$\langle x^\dagger(j)x(j)\rangle = \sum_i g(i,j)\eta_i \sum_k g^\dagger(k,j)\eta_k^\dagger \tag{2.28}$$

since

$$\langle \eta^\dagger(i')\eta(i)\rangle = \delta_{ii'}. \tag{2.29}$$

The source random numbers when combined with themselves for $i' = i$ contributes to the signal. For all other sites the average is zero and contributes only to the noise in the correlator. In the MILC code, the random wall source is used as the base source and then the appropriate phases and operators as described before are multiplied with the base source to produce the modified source. This is then used as the source vector for the calculation of the propagators. I have used the subset 'corner' mask with the random wall source for specific calculations where I dealt with the clover-staggered combined correlators. The subset corner mask has the support at the origins of the 2^4 hypercubes inside the lattice, meaning, at all other points the source is null. Whereas this reduces the statistics (still good enough for our calculation), we do not need to worry about the position dependent staggering transformations and the overall phases of the operators as only the even sites contribute.

2.4.3 Twisted boundary condition

In lattice simulations, historically, periodic boundary conditions (PBC) have been used to realise non-zero momenta. A fermion field $\psi(p)$ satisfying the PBC in the $\hat{\mu}$

direction is defined as:

$$\psi(p + L_\mu \hat{\mu}) = \psi(p) \tag{2.30}$$

where L_μ is the spatial length of the lattice in the $\hat{\mu}$ direction. Using the PBC the momentum change achieved is quantised by an amount $2\pi n_\mu / L_\mu$ where n_μ is an integer.

However, to study the momentum dependent form factors where one needs to simulate the non-zero momentum propagators with tuned momenta, it became more essential to achieve an arbitrary momentum. It is done by defining a fermion field which satisfies the twisted boundary condition [33, 34] (TBC) given by

$$\psi(p + L_\mu \hat{\mu}) = e^{i\theta_\mu} \psi(p). \tag{2.31}$$

Now, this allows us to access any momentum θ_μ / L_μ in the μ direction with an arbitrary shift.

The momentum twist to the propagator is reflected in the two-point correlator as follows

$$\begin{aligned} C^{\rm 2pt}_{BA}(t;\vec{0}) &= \sum_x e^{-i\vec{p}.\vec{x}} \langle \bar{\psi}_2^{\theta_2}(x) \Gamma_B \psi_1^{\theta_1}(x) \bar{\psi}_1^{\theta_1}(0) \Gamma_A \psi_2^{\theta_2}(0) \rangle & (2.32) \\ &= -\sum_x e^{-i\vec{p}.\vec{x}} \langle {\rm Tr} \left(\tilde{S}_2^{\theta_2}(0,x) \Gamma_B \tilde{S}_1^{\theta_1}(x,0) \Gamma_A \right) \rangle. & (2.33) \end{aligned}$$

Usually the Dirac matrix inverters in the simulation code use the PBC for simplicity, therefore, the question is how to realise the TBC in the correlators using PBC Dirac inverters.

We can find one such fermionic field, $\psi(p)$, satisfying the PBC which can be related in the following way to the field, $\psi'(p)$, satisfying the TBC:

$$\psi'(p) = e^{i\theta_\mu p_\mu / L_\mu} \psi(p). \tag{2.34}$$

To realise the correlators in terms of $\psi'(p)$, the relation 2.34 has to be implemented in the fermion action and the matrix inversion.

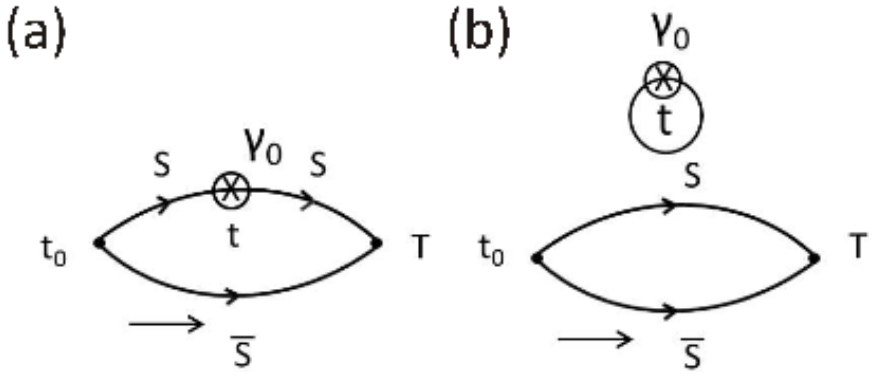

Figure 2.3: Three-point meson correlators: a) quark-line connected, b) quark-line disconnected.

The momentum introduced by the TBC can be tested by studying the dispersion relation. Unlike the zero-momentum correlators for the pseudoscalar mesons made of a single quark flavour, the correlators generated with momentum have oscillating pieces. More complications arise while smearing the twisted fields or combining momentum twist with a point-split operator using staggered quarks [35].

2.4.4 Three-point correlation functions

A general three-point correlation function of meson operators and bilinear currents has the form

$$\begin{aligned} & G^{\rm 3pt}_{CBA}(\vec{q}, t_y; \vec{p}, t_x) \\ = & \sum_{x,y} e^{-i(q.y+p.x)} \langle \bar{\psi}_3(y) \Gamma_C \psi_2(y) \bar{\psi}_2(x) \Gamma_B \psi_1(x) \bar{\psi}_1(0) \Gamma_A \psi_3(0) \rangle \qquad (2.35) \\ = & \sum_{x,y} e^{-i(q.y+p.x)} \langle {\rm Tr}\,(S_3(0,y) \Gamma_C S_2(y,x) \Gamma_B S_1(x,0) \Gamma_A) \rangle. \qquad (2.36) \end{aligned}$$

The three-point functions also have two topologically different diagrams- the quark-line connected and the quark-line disconnected diagrams as shown in the figure 2.3. The cases I studied did not have the quark-line disconnected diagrams. I have used the "sequential source technique" [36] to make the three-point correlators which will be discussed in more detail in Chapters 3 and 5.

2.5 Operator renormalisation

Before we can extract the expectation values of physical meson observables from lattice operator matrix elements, we have to properly match them to a continuum regularisation scheme. This is because the renormalisation depends on the scheme and scale, and the lattice and continuum regularisation schemes are different. The $\overline{MS}$ scheme [37] with dimensional regularisation are used as the most common renormalisation techniques in continuum QCD, whereas the lattice itself plays the role of the ultraviolet regulator in lattice QCD. The lattice spacing puts a cutoff on the allowed momenta and higher than π/a_μ momenta are discarded where a_μ is the lattice spacing in the μ direction. To convert any lattice operator $\hat{O}_{\text{latt}}$ to the corresponding continuum operator $\hat{O}_{\text{cont}}$ we need a matching factor Z.

$$Z\hat{O}_{\text{latt}} = \hat{O}_{\text{cont}}. \tag{2.37}$$

For lattice actions preserving symmetries, the renormalisations are simplified. For example, the staggered quarks have both the vector current renormalisation Z_V for the conserved vector current and the partially conserved axial vector current renormalisation Z_A equal to 1 because they have enough chiral and flavour symmetry for that. Indeed all the lattice actions have enough symmetry for Z_V equal 1 for some vector current.

The staggered action posseses a remnant chiral symmetry, i.e. symmetry under the following transformation

$$\psi \to e^{i\theta(\gamma_5 \otimes \gamma_5)}\psi. \tag{2.38}$$

As a consequence, on the lattice the HISQ action has a temporal axial current that obeys the PCAC relation [38]. The PCAC relation is,

$$\partial_\mu A^\mu = (m_{q_1} + m_{q_2})P \tag{2.39}$$

with m_q as the bare valence quark mass and P local pseudoscalar density. Since

$m_q P$ is conserved, the corresponding current does not require any renormalisation and consequently the decay constants are absolutely normalised.

Historically, the lattice renormalisation factors have been calculated using lattice perturbation theory [39,40], but it leads to significant systematic uncertainties. With the reduction of the other sources of errors such as the discretisation effects and the chiral extrapolation, it is now one of the limiting factors in the accuracy obtained from lattice QCD calculations. Therefore, I have used completely non-perturbative techniques to calculate the vector current and the axial vector current renormalisations for the HISQ and the clover actions using the automatically normalised staggered pseudoscalar currents. This will be discussed in detail in Chapter 3.

2.6 Analysis of the correlation functions

The time-dependent two-point correlation functions can be analysed by fitting them to known fit forms and thus the meson mass and the decay constant can be extracted. A general two-point function is expressed as the expectation value of the product of the operators.

$$G^{\rm 2pt}_{BA}(t;\vec{p}) \;=\; \sum_{\vec{x}} e^{-i\vec{p}.(\vec{x}-\vec{x_0})}\langle 0|\chi_B(x)\bar{\chi}_A(x_0)|0\rangle \tag{2.40}$$

where the source-sink time separation, $t > 0$.

Now by inserting a complete set of normalised energy eigenstates

$$|0\rangle\langle 0| + \sum_{n\neq 0,\vec{q},s} |n,\vec{q},s\rangle\langle n,\vec{q},s| = 1 \tag{2.41}$$

in equation 2.40 we get the two-point correlator as

$$G^{\rm 2pt}_{BA}(t;\vec{p}) \;=\; \sum_{x} e^{-i\vec{p}.\vec{x}}\langle 0|\chi_B(x)|n,\vec{q},s\rangle\langle n,\vec{q},s|\bar{\chi}_A(x_0)|0\rangle. \tag{2.42}$$

Here, $\langle n,\vec{q},s|$ represents the n-th eigenstate with momentum $\vec{q}$ and spin s. Using the time evolution in the equation 2.42 we end up with

$$G^{\rm 2pt}_{BA}(t;\vec{p}) \;=\; \sum_{n,s} e^{-E_n(t-t_0)}\langle 0|\chi_B(x_0)|n,\vec{p},s\rangle\langle n,\vec{p},s|\bar{\chi}_A(x_0)|0\rangle. \tag{2.43}$$

Therefore, from equation 2.43, for the same interpolating field $\chi_A = \chi_B$ the general form of the two-point function is [1–3]

$$G^{\rm 2pt}(t;\vec{p}) = \sum_n a_n^2 e^{-E_n(t-t_0)} \tag{2.44}$$

after absorbing the normalisation factors in the n-th state amplitude a_n. Here, n represents the number of the excited state and $n = 0$ represents the ground state of the meson. The correlator amplitude for the n-th energy state, a_n can be related to the decay constant of the meson, f, when properly normalised and E_n gives the energy of the n-th excited state, E_0 being the mass of the meson, m, if the meson is at rest. Ideally the series has infinite number of states, but the data are not generally good enough to extract the heavier state masses accurately.

We are mostly interested in the extraction of the ground state properties from the two-point fits and the heavier states are included to improve the accuracy of the ground-state.

The actual fit forms I have dealt with are a lot more complicated than that in equation 2.44. Due to the use of periodic boundary conditions the two-point correlator becomes of the form

$$G^{\rm 2pt}(t;\vec{p}) = \sum_n a_n^2 [e^{-E_n t} + e^{-E_n(T-t)}]. \tag{2.45}$$

where T/a is the time length of the lattice. The second term in equation 2.45 represents the meson propagation from the time boundary in the opposite direction as the first term.

2.6.1 Staggered quark oscillations

The two-point correlator form is further complicated due to the presence of oscillations from one time slice to the next time slice on the lattice in the case of staggered quarks. This oscillation shows up from time doublers arising in the doubling transformation

(in equation 1.24). Since the summation in the correlator expession is on the spatial indices, the extra $(-1)^x_\rho$ vanishes for the spatial coordinates when averaged over odd and even sites. But the $(-1)^t$ phase still remains in the correlator expression and produces the oscillation. This extra state couples to the opposite parity state to that of the non-oscillating state. Therefore, the full two-point correlator function in the presence of PBC and staggered quark oscillations has the following form

$$\begin{aligned} G^{\rm 2pt}(t;\vec{p}) &= \sum_n a_n^2 (e^{-E_n t} + e^{-E_n (T-t)}) \\ &\quad + (-1)^t \sum_{n_o} a_{n_o}^2 (e^{-E_{n_o} t} + e^{-E_{n_o}(T-t)}). \end{aligned} \tag{2.46}$$

Here, n_o numbers the oscillating states present in the correlator. a_{n_o} and E_{n_o} are the corresponding amplitudes and energies respectively.

This oscillation is present in any two-point correlators made up of two staggered quarks with an exception of the pseudoscalar mesons made of one type of quark only (for example, a neutral pion) at rest.

In a similar way, the three-point correlators also contain oscillating pieces and their general form for staggered quark correlators is

$$\begin{aligned} G^{\rm 3pt}(t;T) &= \sum_{n_1,n_2} a_{n_1} a_{n_2} V^{nn}_{n_1 n_2} (e^{-E_{n_1} t} + e^{-E_{n_2}(T-t)}) \\ &\quad + (-1)^t \sum_{n_1 o, n_2} a_{n_1 o} a_{n_2} V^{on}_{n_1 o n_2} (e^{-E_{n_1 o} t} + e^{-E_{n_2}(T-t)}) \\ &\quad + (-1)^T \sum_{n_1, n_2 o} a_{n_1} a_{n_2 o} V^{no}_{n_1 n_2 o} (e^{-E_{n_1} t} + e^{-E_{n_2 o}(T-t)}) \\ &\quad + (-1)^{t+T} \sum_{n_1 o, n_2 o} a_{n_1 o} a_{n_2 o} V^{oo}_{n_1 o n_2 o} (e^{-E_{n_1 o} t} + e^{-E_{n_2 o}(T-t)}). \end{aligned} \tag{2.47}$$

Here, t is the current insertion time on the lattice and T is the separation between the source and the sink (see Figure 2.3). The three-point correlators have oscillations at both ends and, n and o indices in the three-point amplitude V indicate whether the amplitude corresponds to the non-oscillating or the oscillating state. The three-point amplitude is needed for my calculations of the renormalisation constants in Chapter 3 and the form factor calculation in Chapter 5.

2.6.2 Fitting correlators

To extract the mass and the amplitudes from the correlators my strategy was to use the constrained curve fitting [41] method using Bayesian Statistics. I have used publicly available fitting packages written by G. Peter Lepage, the "Corrfitter" and the "lsqfit", to analyse the two-point and the three-point correlators.

The basic principle is to minimise χ^2 defined by

$$\chi^2 = \sum_{t_1,t_2} \frac{\delta G(t_1)\delta G(t_2)}{\sigma^2_{t_1 t_2}}. \tag{2.48}$$

Here,

$$\delta G(t) = \bar{G}(t) - G(t) \tag{2.49}$$

where $G(t)$ is the fit function and $\bar{G}(t)$ is the correlator data and

$$\sigma^2_{t_1 t_2} = \langle G(t_1)G(t_2)\rangle - \bar{G}(t_1)\bar{G}(t_2) \tag{2.50}$$

represents the correlation matrix.

However, I had to deal with multiexponential (multiple energy states) fits of a large number of fit parameters a_n, E_n and, V^{nn}, V^{on}, V^{no}, V^{oo}. Minimising the χ^2 naively leads to very unstable fit results. Therefore, we take a different approach by specifying reasonable priors (coming from earlier works or particle data listing or from general physics arguements) for all the fit parameters and then construct an augmented χ^2 by trusting these priors as additional data.

$$\chi^2_{\text{aug}} \equiv \chi^2 + \chi^2_{\text{prior}} \tag{2.51}$$

where,

$$\chi^2_{\text{prior}} \equiv \sum_{\text{parameters}} \frac{(\text{fit value} - \text{fit prior})^2}{\text{prior width}^2}. \tag{2.52}$$

Then, χ^2_{aug} is minimised to get the best fit. The test of whether the data knows anything about a parameter is whether it returns a result that is more accurate

than the prior information. Generally, I have fitted up to seven exponentials (i.e. the 7th energy state) to get a stable result (mean value) for the ground and lower excited states with χ^2/degree of freedom < 1 typically, though in most of the cases the result is stable after the 2nd or 3rd exponential. Even if we are allowed to consider any arbitrary number of exponentials with their priors, the higher excited states are allowed to take unrealistic masses and typically not determined at all.

Another measure of a good fit is the "quality of the fit" or the "Q-value". Assuming the null hypothesis is valid, the "Q-value" represents the probability that, given a model, the observed sample result is at least as far off the prediction as the real data is -

$$Q = \frac{\int_{\chi^2/2}^{\infty} t^{n/2-1} e^{-t} dt}{\int_0^{\infty} t^{n/2-1} e^{-t} dt}. \tag{2.53}$$

For a good quality fit the accepted $Q \in [0.1, 1]$.

I have used simultaneous fits of the two-point and the three-point correlators to extract the three point amplitudes. The simultaneous fits of the correlated data let us take into account the correlation correctly and calculate a complete error budget. I will discuss more about fitting later for specific cases.

2.6.3 Effective mass

The ground state meson mass can be estimated by looking at the "effective mass" using the meson correlator. The effective mass is defined as

$$m_{\text{eff}}(t) = \ln \left[\frac{G^{\text{2pt}}(t)}{G^{\text{2pt}}(t+1)} \right]. \tag{2.54}$$

For large t, we expect the excited state contamination in the meson two-point correlators to go away and only the ground state to dominate. Therefore, the effective mass plot with t shows a plateau after the first few time slices on the lattice. This value of the effective mass at the plateau is estimated as the mass of the meson which is then used as the ground state meson energy (at rest) prior in the fitting.

2.7 Determining lattice uncertainties

In a lattice calculation, it is crucial to give a reliable total uncertainty to physical observables. The lattice uncertainties are broadly classified into two categories - the statistical uncertainty and the systematic uncertainty. The statistical uncertainties arise from stochastic evaluation of the path integrals in the Monte-Carlo simulations and can be estimated from the fitting code. These statistical uncertainties fall off as $1/\sqrt{N}$, where N is the number of independent gauge configurations, therefore, they can be reduced by simply generating a larger ensemble size. To reduce the correlation coming from the random sampling, while generating the gauge configurations (generated by the MILC collaboration in this case), it is usual to skip a few configurations in-between two accepted configurations and/or generate uncorrelated configurations using different random number seeds in the Monte-Carlo process.

In a lattice QCD calculation, apart from the statistical uncertainties introduced by the Monte-Carlo simulation, systematic uncertainties also appear due to different lattice artifacts, which can also be estimated from the data. For a reliable estimation of the lattice uncertainties, we have to consider and estimate all of the lattice artifacts described below.

2.7.1 Finite lattice Spacing

Lattice actions have discretisation effects due to the finite lattice spacing. To reduce this artifact, one can choose smaller and smaller lattice spacings, but ends up with the problem of "critical slowing-down" [42–44]. The computation time needed for generating the independent gauge configurations for the finer lattices with a constant physical volume increases rapidly.

A much more cost-effective way is to carry on our simulation on multiple lattice spacings which allows us to achieve a controlled continuum extrapolation (to $a \to 0$)

and extract the continuum physical results. Also, we formulate highly improved lattice actions (such as the HISQ action [17] as discussed before) with smaller discretisation effects, by adding higher dimensional operators.

To know the correct extrapolation fit form we can determine the order at which the lattice artifacts appear by studying the expansion in powers of the lattice spacing of the discretised action. This is done with the help of the *Symanzik effective field theory* where the Symanzik Lagrangian is formed by combining the continuum Lagrangian and the lattice artifacts.

$$\mathcal{L}_{\text{Sym}} = \mathcal{L}_{\text{QCD}} + \mathcal{L}_{\text{disc}} \tag{2.55}$$

where $\mathcal{L}_{\text{disc}}$ contains all the local higher order operators O_p allowed in the lattice action by its symmetries.

$$\mathcal{L}_{\text{disc}} = \sum_p a^{d_p-4} c_p O_p. \tag{2.56}$$

Here, d_p is the dimension of the operator O_p and c_p is the coupling and scale dependent dimensionless short-range coefficient. Now, for an example, let us consider a dimension-five operator in the lattice action, which in fact breaks the chiral symmetry of the lattice action. We can see from the equation 2.56 that a discretisation term $\sim \mathcal{O}(a)$ is present in the lattice action in this case. Therefore, for chirally symmetic lattice actions, no $\mathcal{O}(a)$ discretisation is present.

Similarly, using the Symanzik effective theory order-by-order we can deduce the continuum extrapolation form for the HISQ action -

$$\langle \mathcal{O}(a) \rangle = \langle \mathcal{O}(0) \rangle + \sum_i c_i a^{2i}. \tag{2.57}$$

Therefore, for the HISQ, the discretisation effects come in as even powers of a with $\langle \mathcal{O}(0) \rangle$ as the expectation value of the observable in the continuum.

2.7.2 Unphysically heavy light quark masses

In lattice simulations with the dynamical quarks, the computation cost is dominated ($\sim 90\%$) by the inversion of the fermion matrix which is $\mathcal{O}(10^6 \times 10^6)$. The computation time grows inversely with some power of quark mass and the computation speed is governed by the light quark (up/down) masses. Therefore, for easier computation, we use heavier than physical light quark masses with almost physical strange and charm quark masses in the sea. In some cases, the observables have strong dependence on the light quark mass, which introduces large systematic uncertainties in the calculation. Therefore, I have taken u and d quarks with several masses ($m_u = m_d$ with estimated isospin effects) down to the physical ones ($m_l \equiv m_u = m_d \simeq m_s/27$) and up to $m_l = 0.2m_s$. With all the different m_l we can interpolate smoothly to the physical (chiral) limit using chiral perturbation theory (ChPT), an effective theory [45–47] of QCD at low energies, to correct for small mistunings in m_l and m_s. Simultaneously, the finite lattice spacing effects can be included in the ChPT Lagrangian.

2.7.3 Finite lattice volume

The effects of finite volume can be reduced significantly by using a larger volume, especially for lighter quarks. For a single hadron in a periodic box of size much larger than itself, the finite size effect falls off asymptotically as $e^{-m_\pi L}$ [48] where m_π is the mass of the pion. Ideally, we should take $m_\pi L > 4$ for any hadron to fit its Compton wavelength inside the lattice and make the finite volume effects negligible. The study of finite volume effects can be performed systematically using ChPT for a finite box [49, 50]. I will discuss more on this in Chapter 4 for the calculation of the hadronic vacuum polarisation contribution to the anomalous magnetic moment of the muon.

Part II

Non-perturbative renormalisation of currents and meson spectroscopy

Chapter 3

Non-perturbative renormalisation of currents and meson spectroscopy

3.1 Motivation

The precise calculation of the weak decay matrix elements of heavy-light mesons from lattice QCD is crucial for the flavour physics program of overdetermining the Cabbibo-Kobayashi-Maskawa (CKM) matrix elements [51,52]. Any violation of CKM unitarity would indicate the existence of new physics beyond the Standard Model. A good test of lattice QCD is the comparison of the results using different quark formalisms. The results for the B and B_s meson decay constants for different quark formalisms are summarised in Figure 3.1, and the tension with experiment for f_B is shown. Heavy quarks have been extensively studied using non-relativistic formalisms, although relativistic formalism for these quarks are now possible. Two of the most used nonrelativistic methods are the NRQCD [53] and the Fermilab [54] formalisms. The HPQCD collaboration have obtained separate results using NRQCD b quarks [55] and HISQ b quarks [56], both combined with HISQ light quarks, whose f_{B_s} values are consistent within their $\sim 2\%$ uncertainties. The systematic uncertainties for the

two methods are very different, with the NRQCD b quark case having a significant contribution from the uncertainty in the current renormalisation. By contrast, the HISQ action has a remnant chiral symmetry which means that its temporal axial current is normalised. There is hence no such uncertainty for HISQ b quarks. However, in this case the total systematic uncertainty is dominated by the discretisation errors. An alternative method from the Fermilab lattice/MILC collaborations uses heavy clover b quarks [57, 58]. This method also gives a reasonably consistent result but with much larger uncertainties. Here we test the method [59] for determining the current renormalisation in this formalism to see if the estimate of the uncertainties from that source is robust.

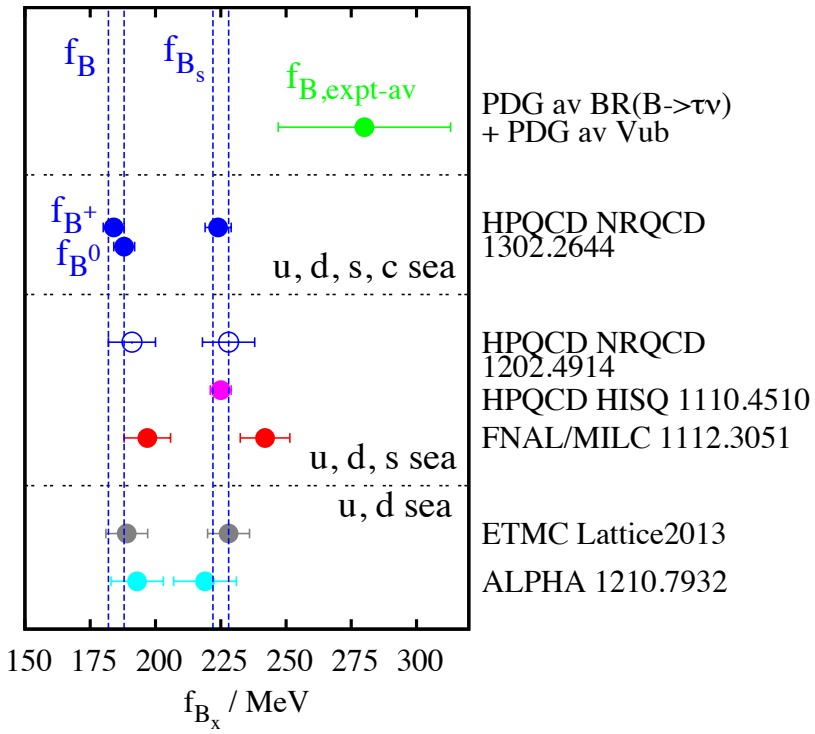

Figure 3.1: In this plot the lattice results for the B and B_S meson decay constants f_B and f_{B_s} using different formalisms with two, three and four flavours of sea quarks have been compared with the experimental average for f_B. The dotted vertical lines represent the the world averages of all the lattice results for f_B and f_{B_s}. This plot has been borrowed from a talk by Prof. Christine Davies.

3.2 Background

The renormalisation constant (Z) needs to be calculated as accurately as possible for the currents which are not conserved in any particular lattice formalism. The renormalisation constant beyond the tree-level is an ultraviolet quantity as it allows for the difference between the gluon radiation in the continuum and on the lattice where the lattice works as an ultraviolet regulator. Therefore, Z can be calculated using QCD perturbation theory and practically up to $\mathcal{O}(\alpha_s)$ by equating the one-loop scattering amplitude between on-shell quark states in the continuum and on the lattice [60].

In the Fermilab formalism [54] while generating the heavy-light mesons (for example, B and D) [57, 58] a heavy quark generated with the Fermilab action is tied in a two-point correlator with another light quark generated using the clover [57] or the Asqtad [58] action. In doing these calculations for the Fermilab heavy quarks it was noticed [61] that the heavy-light current renormalisation differed very little at $\mathcal{O}(\alpha_s)$ from the geometric mean of the appropriate heavy-heavy (hh) and light-light (ll) vector currents. Specifically, the Fermilab Lattice/MILC collaborations calculated the temporal axial current renormalisation (Z_{A^4}) in one-loop perturbation theory and the local vector current renormalisation (Z_{V^4}) using non-perturbative techniques. They claimed

$$Z_{A^4{}_{hl}} = \rho\sqrt{Z_{V^4{}_{hh}} Z_{V^4{}_{ll}}} \tag{3.1}$$

i.e. the heavy-light temporal-axial current renormalisation is equal to the geometric mean of the heavy-heavy and light-light temporal vector current renormalisations with a multiplication factor ρ, with ρ very close to 1.

ρ can be expanded in the following perturbation series,

$$\rho = 1 + \rho^{(1)}\alpha_s + \rho^{(2)}\alpha_s^2 + \ldots \tag{3.2}$$

From one-loop perturbation theory Fermilab/MILC found $\rho^{(1)}$ to be very small

(typically it is $< 4\pi \times 0.01$) if the heavy quark mass is not too large (see Figure 3.4). Because of this they further assumed that $\rho^{(2)}$ and higher orders were also small making ρ close to unity. The renormalisations $Z_{V^4{}_{hh}}$ and $Z_{V^4{}_{ll}}$ can be determined fully non-perturbatively in lattice QCD by demanding that the vector form factor is unity between two identical mesons at rest. Thus equation 3.1 gives rise to the possibility that $Z_{A^4{}_{hl}}$ could be determined with small uncertainties if it can be shown that ρ is indeed close to 1 to all orders in perturbation theory. In practice the region of small values of $\rho^{(1)}$ extends up to the b quark mass in the Fermilab formalism for at least the fine lattices with $a < 0.1$ fm. That means essentially the relations 3.1 and 3.2 hold good for "light" heavy quarks and in this limit the Fermilab action becomes the standard tadpole-improved clover action.

However, for the hypothesis that ρ is very close to 1 to be true, each term in the perturbation series beyond one-loop needs to be determined. A large part of the perturbative Z comes from the self energy of the individual quark legs and this part will cancel in ρ. This only guarantees that beyond one-loop all the ρ coefficients will have a reasonably small value, but not that they should be as small as $\rho^{(1)}$. If this hypothesis is not true to all orders of the ρ coefficients it can limit the precision of the heavy quark observables in the Fermilab lattice simulation by a significant amount (since Fermilab assumed it to limit their uncertainty).

It will be more useful if we can show that the hypothesis does not depend on a particular light quark formalism. Therefore, my aim was to test completely non-perturbatively how much ρ differs from 1. The 'heavy-light' current in my calculation has been made of a clover quark (representing the Fermilab formalism) and a HISQ quark (state-of-the-art staggered quark) [17], both tuned accurately to the strange quark mass [25, 56], following the suggestion in [51]. We use the absolute normalisation for the HISQ-HISQ temporal axial current (as a consequence of the remnant chiral symmetry of the HISQ action) to renormalise both the HISQ-clover and the clover-clover

temporal axial currents. We do it by claiming the physical meson properties to be the same for all the lattice quark formalisms. Then by determining the appropriate vector currents in equation 3.1 we can extract a non-perturbative value for ρ in equation 3.2 in this case and test it against the hypothesis that it should be close to unity. We are also able to study the clover-clover renormalisation factors and compare Z_{A^4} and Z_{V^4} for this case.

From the same s quark propagators generated for this calculation we can also make the ϕ ($s\bar{s}$ vector meson) correlators. And we can study the ϕ meson mass and decay constant for the cases where the ϕ is made purely of the clover quarks or purely of HISQ quarks, or made of one of each. We can then compare the approach to the continuum limit of each of the results. This tests whether the same continuum limit is reached and how the discretisation errors in the clover and the HISQ formalisms compare.

3.3 Formalism

In our calculation for determining Z_{A^4} for the clover-clover (cl-cl) and HISQ-clover (H-cl) currents I have made the cl-cl and the H-cl η_s mesons from binding two clover or one clover and one HISQ strange quarks (as depicted in Figure 3.2). The η_s is a pseudoscalar meson made of a strange and an anti-strange quark which does not exist in the real world. [1] The η_s is particularly easy to make on the lattice [25] and we do not allow it to decay there by only including the connected correlator, making it an ideal pseudoscalar meson for testing and tuning purposes. The two-point HISQ-HISQ (H-H) η_s correlators are also generated (Figure 3.2), with both the local Goldstone operator with spin-taste $\gamma_5 \otimes \gamma_5$ for the pseudoscalar current and the nongoldstone

[1] In the real world the η_s can annihilate, and therefore, mixes with light-light pseudo scalar mesons. The results are two particles called the η and η'. We do not allow the annihilation to happen on the lattice. So, it is well-defined there.

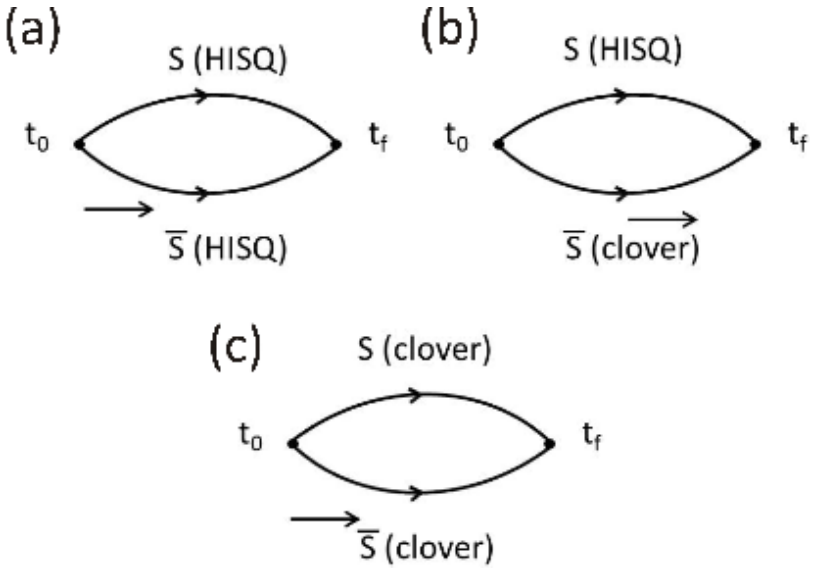

Figure 3.2: In the diagram 'a' two strange HISQ quarks are generated at time t_0 on the lattice with a pseudoscalar or a temporal axial current. They propagate to a later time t on the lattice and are destroyed at that time with another current with the same 'taste'. Similarly, in the diagram 'b' and 'c' the clover-clover and HISQ-clover correlators are represented.

opertaor with spin-taste $\gamma_5\gamma_4 \otimes \gamma_5\gamma_4$ [2] for the local temporal axial current. We need the same operator at both the source and the sink to make the two-point correlator.

Due to the presence of the PCAC (partially conserved axial current) relation [62], the appropriate (non-local) H-H temporal axial current is absolutely normalised and so is the decay constant (f_{η_s}) derived from the $\gamma_5 \otimes \gamma_5$ pseudoscalar operator. We get the temporal axial cl-cl and H-cl current renormalisation factors $Z_{A^4_{\rm cl-cl}}$ and $Z_{A^4_{\rm H-cl}}$ using the relations

$$Z_{A^4_{\rm cl-cl}} f^{\rm cl-cl}_{\eta_s} = f^{\rm H-H}_{\eta_s}, \tag{3.3}$$

$$Z_{A^4_{\rm H-cl}} f^{\rm H-cl}_{\eta_s} = f^{\rm H-H}_{\eta_s}. \tag{3.4}$$

An alternative method, but one that we do not use, would be to set the cl-cl decay constant corresponding to the physical value of 181.14 MeV obtained in [25]. Because

[2] Staggered mesons contain different tastes; by definition the taste operator γ_5 corresponds to the Goldstone operator. All other taste operators are known as the non-Goldstone operators for the pseudoscalar. In the spin-taste operator notation the cross product $\otimes$ is traditionally used and it only implies general matrix multiplication.

the discretisation effects seen in the H-H values of f_{η_s} are so small this would make little difference, at most 0.5% on set '1' in Table 3.1. Another definition can be

$$Z^{\rm alt}_{A^4_{\rm cl-cl}} m^{\rm cl-cl}_{\eta_s} f^{\rm cl-cl}_{\eta_s} = m^{\rm H-H}_{\eta_s} f^{\rm H-H}_{\eta_s}. \tag{3.5}$$

$$Z^{\rm alt}_{A^4_{\rm H-cl}} m^{\rm H-cl}_{\eta_s} f^{\rm H-cl}_{\eta_s} = m^{\rm H-H}_{\eta_s} f^{\rm H-H}_{\eta_s}. \tag{3.6}$$

This definition is the one in which we choose the matrix element of the axial current to match.

In the H-cl case, because the η_s mass m_{η_s} is not exactly the same as the tuned value there is a difference between matching decay constants and matching matrix elements. Because the difference in mass is a discretisation effect we have chosen to match the decay constants. The differences between doing this and matching the matrix element $f_{\eta_s} m_{\eta_s}$ are as large as 6% on set '1' in Table 3.1 and act in the direction of making Z_{A^4} smaller than that quoted.

The decay constant of a meson is defined as the matrix element between the meson and the vacuum of the temporal axial current that couples to the W boson when the meson is at rest and, therefore, for the η_s (on the lattice) the decay constant is given by

$$\langle 0|A^4|\eta_s(0)\rangle = m_{\eta_s} f_{\eta_s}. \tag{3.7}$$

From this equation we can extract the decay constant f_{η_s} as

$$f_{\eta_s} = a_0 \sqrt{\frac{2}{m_{\eta_s}}} \tag{3.8}$$

where a_0 is the ground state amplitude for the temporal axial current operator.

The temporal axial current is absolutely normalised for the H-H current and due to the PCAC relation it is related to the local pseudoscalar current density $\langle P\rangle$ as follows

$$\partial_4 A^4 = (m_s + m_s)\langle P\rangle. \tag{3.9}$$

Here, m_s is the lattice valence strange quark mass. Let us consider the matrix elements for both sides of equation 3.9 between the η_s state and the vacuum. Then we apply equation 3.7 and the following equation:

$$\langle 0|P|\eta_s(0)\rangle = b_0\sqrt{2m_{\eta_s}} \tag{3.10}$$

where b_0 is the ground state amplitude for the local pseudoscalar operator.

Thus we obtain f_{η_s} in the H-H case as follows

$$f_{\eta_s}^{\mathrm{H-H}} = \frac{2m_s b_0^{\mathrm{H-H}}}{m_{\eta_s}^{\mathrm{H-H}}}\sqrt{\frac{2}{m_{\eta_s}^{\mathrm{H-H}}}}. \tag{3.11}$$

m_{η_s}, a_0 and b_0 are extracted from the two-point correlator fits described later in this chapter.

In the absence of the PCAC relation for the clover action, we use the temporal axial current and then the un-normalised decay constants for the cl-cl and the H-cl mesons can be defined as

$$f_{\eta_s}^{\mathrm{cl-cl}} = a_0^{\mathrm{cl-cl}}\sqrt{\frac{2}{m_{\eta_s}^{\mathrm{cl-cl}}}}, \tag{3.12}$$

$$f_{\eta_s}^{\mathrm{H-cl}} = a_0^{\mathrm{H-cl}}\sqrt{\frac{2}{m_{\eta_s}^{\mathrm{H-cl}}}} \tag{3.13}$$

To obtain the renormalisations for the H-H, cl-cl, and H-cl temporal vector currents, we demand that the vector form factors between two identical hadronic states at rest (zero momentum transfer) would be unity i.e.

$$Z_{V_{qq}^4}\langle H_q|V_{qq}^4|H_q\rangle = 2M_H \times f_+(0) = 2M_H. \tag{3.14}$$

We force the vector form factor $f_+(0)$ to be 1 in this case in this equation.

Here, V_{qq}^4 is the lattice version of the local temporal vector current, $|H_q\rangle$ is the hadronic state. The matrix element is extracted by fitting the two-point and three-point correlators simultaneously. Together with the previously discussed two-point correlators, we calculate the three-point correlators described in Figure 3.3 using the same HISQ and the same clover strange propagators.

The three point correlators are generated using a local temporal vector current operator γ_4 inserted between two clover propagators or one clover and one HISQ propagator and $\gamma_4 \otimes \gamma_4$ inserted between two HISQ propagators at time t on the lattice. These three-point correlators are generated using the "sequential source technique". The clover spectator s quark (the bottom one in Figure 3.3 with no current insertion) is generated at the source time t_0 and propagates to the sink time $t_0 + T$. At this sink timeslice the generated propagator is treated as the source and an extended s propagator (HISQ or clover) is generated back in time to any time slice t on the lattice. Then a third HISQ or clover s quark generated from the same t_0 source and propagated to time t is tied with the extended propagator via a local temporal vector current to make the three-point correlator. Here, $t_0 < t < T$ and $T \ll L_t$ where L_t is the temporal length of the lattice. The detailed derivation of the three-point correlator generated using the "sequential source technique" and a random wall source at t_0 will be given in chapter 5.

Here, an important point is that we have chosen the spectator quark to be an unstaggered quark which is the clover in this case. This is because if we use all three staggered propagators to form the three-point correlators we need to take the tastes into account and must have the total taste 1. Since, we want to use the local operators only, using the local temporal vector current operator would not give a total taste 1 for the same mesons at either end and the three-point function would vanish. For all the three currents- H-H, cl-cl and H-cl, the interpolating fields are the same (Goldstone η_s) at both the source and the sink.

Using a relativistic normalisation of states, the matrix element of the lattice temporal vector current between the ground state η_s mesons at rest is given by $2E_0V_{00}$ where V_{00} is the ground state nonoscillating-nonoscillating three point amplitude from

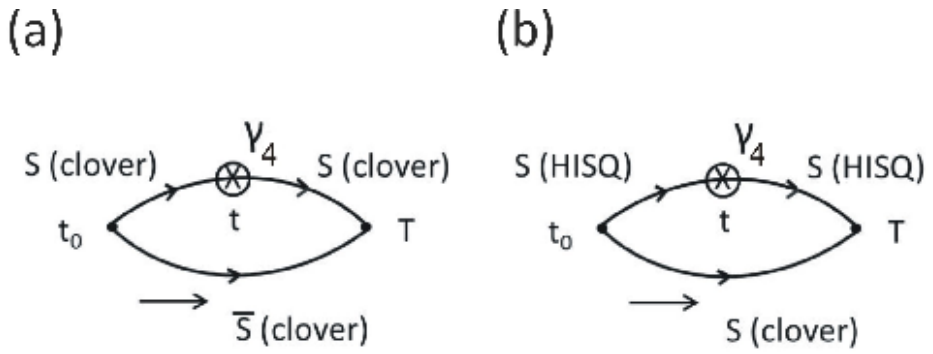

Figure 3.3: Different three-point meson correlators we need to calculate: the clover spectator s quark is generated at the source time t_0 and propagates to the sink time $t_0 + T$. At this sink timeslice the generated propagator is treated as the source and an extended s propagator (HISQ or clover) is generated back in time to any time slice t on the lattice. Then a third HISQ or clover s quark generated from the same t_0 source and propagated to the time t is tied with the extended propagator via a local temporal vector current to make the three-point correlator. Here, $t_0 < t < T$ and $T \ll L_t$, where L_t is the temporal length of the lattice.

the fit and E_0 is the ground state energy of the meson. Therefore, we get

$$\frac{\langle H_q|V^4_{qq}|H_q\rangle}{2m_{\eta_s}} = V_{00}. \tag{3.15}$$

And,

$$Z_{V^4} = \frac{1}{V_{00}}. \tag{3.16}$$

Once we obtain the relevant Z_{A^4}s and Z_{V^4}s accurately we can calculate ρ completely non-perturbatively from equation 3.2 and test the Fermilab hypothesis precisely.

In addition to making the pseudoscalar meson η_s we can use the same s propagators to make a vector meson ϕ with the vector current operator $\gamma_i \otimes \gamma_i$ for the H-H case and γ_i for the cl-cl and H-cl case. Here i denotes the spatial direction of the current and we average over all three independent directions for better statistical precision. From analysing the ϕ two-point correlators we can extract the mass m_ϕ and the ground state amplitude a_0^ϕ, and from them the decay constant f_ϕ of the ϕ meson using

$$f_\phi = a_0^\phi \sqrt{\frac{2}{m_\phi}}. \tag{3.17}$$

We can also make these correlators with the H-H, the cl-cl and the H-cl currents and at the continuum limits of m_ϕ and f_ϕ we can compare the different lattice formalisms, HISQ and clover, and their approach to the continuum.

3.4 Lattice simulation

The lattice simulation was done on the MILC HISQ (same action as used for the valence quarks [17]) $N_f = 2 + 1 + 1$ ensembles of gauge configurations at widely differing values of the lattice spacings_0.15 fm, 0.12 fm and 0.09 fm as described in Table 2.1 and in Figure 2.1 in chapter 2. They include the effects of the u, d, s and c quarks in the sea using the HISQ formalism ($m_u = m_d$) and also use a gluon action improved fully through $\mathcal{O}(\alpha_s a^2)$ [22]. We can therefore expect the gluon fields to have very small 'intrinsic' discretisation errors, which is useful for studying the discretisation errors of the meson correlation functions made on these configurations using different quark formalisms. For the calculation of the renormalisation constants we use a subset of these ensembles with three different lattice spacings, namely, sets '1', '4' and '9' with heavier than physical dynamical light (u/d) quarks.

For the complete calculation of the ϕ properties using the H-H ϕ I have used a more complete set of ensembles including three ensembles with three different lattice spacings and physical dynamical light quarks (sets '3', '8', and '11'). I have also tested for the finite volume effects on the three emsembles with different volumes at a dynamical light quark mass in between the first two and at a specific lattice spacing (set '5', '6', and '7'). The relative lattice spacings were fixed using the w_0 parameter and f_π was used to fix the overall scale [25].

For the Z factor calculation, we have chosen the ensembles which have $m_l/m_s \approx 0.2$, and therefore a relatively modest lattice size of around 3.5 fm to achieve an acceptable numerical speed. Since we are going to calculate the meson correlation functions made

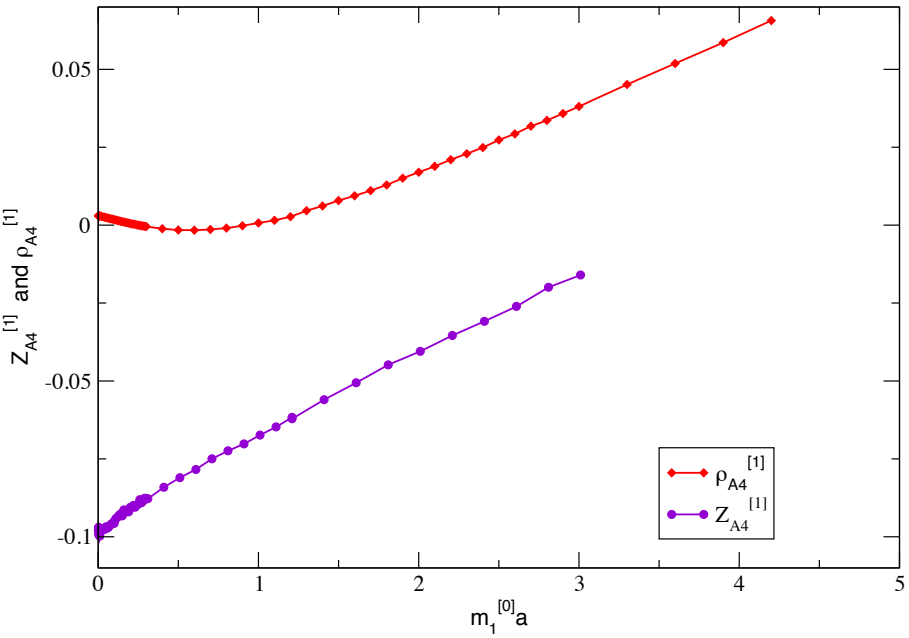

Figure 3.4: The one-loop coefficient of ρ_{A^4} and the temporal axial current renormalisation factor from the one-loop perturbative series $Z_{A^4}^{[1]}$ for the clover-Asqtad case plotted against the clover quark mass $m_1^{[0]}a$ (plot taken from Fermilab/MILC paper [63]). In this plot, in the unit of $m_1^{[0]}a$, the masses of the valence strange quarks we use fall in the range $0.03 - 0.07$.

purely of strange quarks, the fact that m_l/m_s is larger than the physical value is not an issue. We expect the sea quark mass effects to be small and the same for the different valence quarks we use, so this should not affect our comparison.

We have chosen the strange quark as the valence quark as its mass falls within the light quark mass region where the claim for the smallness of the one-loop coefficient of ρ holds. This can clearly be seen from Figure 3.4 [63]. On these ensembles we have carefully tuned the s quark mass for the HISQ quarks through an analysis of the fictitious pseudoscalar meson known as the η_s. However it can be studied on the lattice and its properties, the mass and the decay constant, can be related to the properties of the K and π [25]. From these studies, we find the mass of the η_s in the continuum and the chiral limits to be $m_{\eta_s} = 0.6885(22)$ GeV. On every ensemble we tune the valence HISQ quark mass to give this value for the η_s meson mass, given the

Table 3.1: This table lists the parameters used for calculating the propagators. the configuration details for the sets are given in Table 2.1 in chapter 2. We call sets 1 and 3 as 'very coarse'; sets 4-8 as 'coarse' and set 9 and 11 as 'fine'. In this table the second column gives the tuned valence s quark masses; the third column lists the clover u_0 values; the fourth and the fifth columns give the tuned κ values for clover quarks, and the last two columns denote the number of time sources used on each configuration n_t and the source-sink separation used for generating the three-point correlators T for each t_0.

Set	$am_s^{\text{HISQ,val}}$	u_0	$\kappa_s^{\text{Clover,val}}$	$1-6\times u_0\times\kappa$	n_t	T/a
1	0.0705	0.85535	0.14082	0.277298	12	9, 12, 15, 18
3	0.0678	-	-	-	12	-
4	0.0541	0.86372	0.13990	0.274993	16	12, 15, 18, 21
5	0.0533	-	-	-	16	-
6	0.0533	-	-	-	16	-
7	0.0533	-	-	-	16	-
8	0.0527	-	-	-	16	-
9	0.0376	0.874166	0.13862	0.272939	16	16, 19, 22, 25
11	0.0360	-	-	-	16	-

value of the lattice spacing described in Table 2.1. The tuned values of the valence s quark masses on each ensemble are listed in Table 3.1.

For the clover simulation, I started with the same tuned strange valence mass on each ensemble that was used for the HISQ propagators. Then the hopping parameter κ (defined in Section 1.4.2) on each ensemble was tuned accurately to get $m_{\eta_S} = 0.689$ GeV.

We have,

$$m_{\eta_s}^2 \propto \left(\frac{1}{\kappa} + C\right) \tag{3.18}$$

where, C is a constant. I have chosen three κ values initially and then from the $m_{\eta_s}^2$ vs. $1/\kappa$ plot (given in Figure 3.5), I have obtained the required tuned κ values precisely on each ensemble which are given in Table 3.1 along with the other simulation parameters,

$$m_{\eta_s}^2 \propto m_s \tag{3.19}$$

$$am_s = \frac{1}{u_0}\left(\frac{1}{\kappa} - \frac{1}{\kappa_c}\right). \tag{3.20}$$

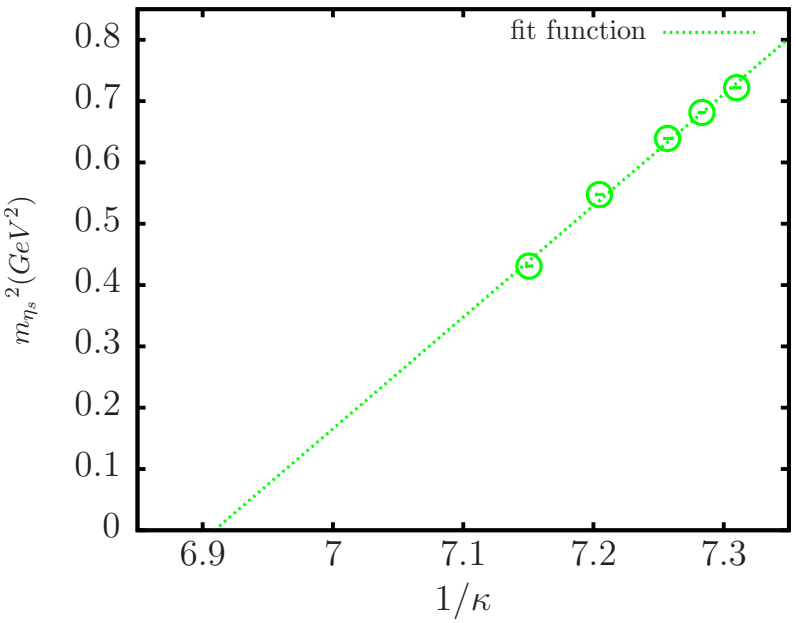

Figure 3.5: Determination of the κ_c for the clover action on the lattice using the coarse lattice; $m^2_{\eta_s}$ vs. $1/\kappa$ plot.

I have used the delta function random color wall sources with the subset corner mask and the point sink. The corner mask restricts the values of the source on each lattice site after the source is constructed by setting the nonzero values only on the corners of each 2^4 hypercubes. To increase the statistics we use many (listed in Table 3.1, n_t being its number) evenly-spaced time sources per configuration. The starting time slice of these sources are chosen randomly and differently for each configuration to reduce the autocorrelation in the meson correlators. Moreover, we can reduce the autocorrelation by binning the correlators between adjacent configurations. This has been tested for our data, but finally was not required [26]. Since the clover quark simulation is four time more expensive than the HISQ simulation, we have used only half as many configurations in the clover case compared to that of the HISQ case (listed in Table 2.1). Furthermore, we calculated the three-point correlators for multiple values of the source-sink time separation T, both odd and even, (given in

Table 3.1) to increase the statistics, as this increases the amount of the data without increasing the number of the parameters. It also lets me get T dependence as well as t dependence.

To generate the clover propagators the standard tadpole-improved space-time symmetric clover action [3] has been used. In the clover action the gluon fields, U_μ, are divided by a tadpole parameter [64], u_0, for which we use the fourth root of the plaquette. The values of u_0 are listed in the Table 3.1 with the other simulation parameters.

To generate the mixed H-cl correlators, the HISQ quarks with only one spin component have been converted back to a naive propagator with four spin components. This was done by the reverse staggering transformation while generating the extended source at the time T. Then the naive propagator could be simply tied to a clover propagator to generate the mixed three-point correlators. The complication in this reverse transformation can arise from the site-dependent staggering matrices. However, this complication has been removed by using a subset corner mask which caused only the origins of the 2^4 hypercubes to contribute in the correlators and always gave a unity reverse transformation Ω matrix.

3.5 Data analysis and fits

The two-point Goldstone η_s correlators have zero imaginary parts i.e. they can be obtained by simply squaring the modulus of the propagators and then summing over a time-slice (taken care of by the random wall formalism) to project onto zero momentum. The properties of the meson such as the mass and the decay constant are extracted from the multi-exponential fits of the two-point correlators using Bayesian techniques [65]. In these fits, the fit parameters are the logarithm of the ground state energy, the logarithms of energy differences (both for the oscillating

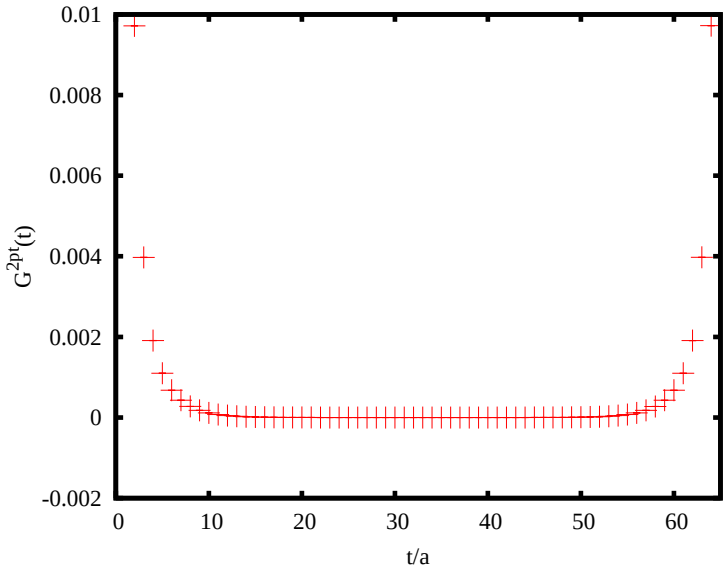

Figure 3.6: An average two-point correlator for H-H η_s on the $m_l/m_s = 0.2$ coarse lattice.

and the non-oscillating states) and amplitudes which are allowed to be of either sign. In general, for the relativistic staggered quarks, the fit function is mathematically expressed as a sum of two functions, one of hyperbolic nature and another with oscillations [26], and is given by equation 2.46.

But, in the case of the Goldstone η_s meson, no oscillations were observed due to the equal masses of the valence quark and the antiquark. So, in our case we can write the H-H η_s two-point correlators (example shown in Figures 3.6 and 3.7 for the coarse ensemble) in a simplified form as given by the equation 2.45.

In this calculation we have obtained very high statistics which is clear from the effective mass plot in Figure 3.8. The non-goldstone H-H η_s correlators and the H-H ϕ correlators have oscillating opposite parity contributions, therefore, they still follow the more general fit form in equation 2.46.

For the fitting, we have chosen the full time range except the first and the last 3 to

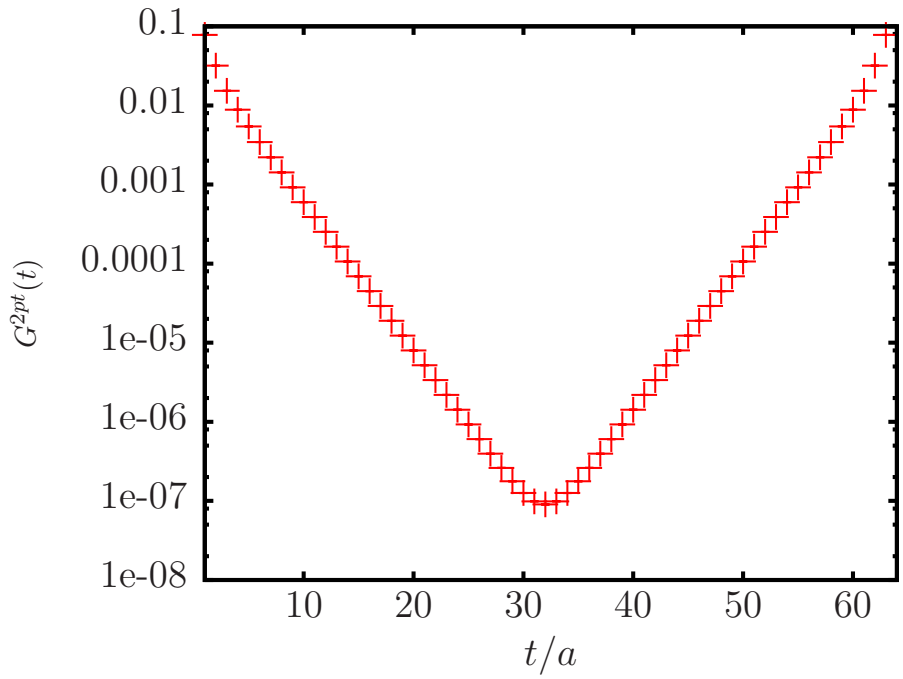

Figure 3.7: An average two-point correlator for H-H η_s on the $m_l/m_s = 0.2$ coarse lattice in vertical logscale.

5 timeslices to minimise the excited state contamination in the ground state energy and amplitude.The parameters we fit are the energy, the amplitude and the difference in the energies for the oscillating and the non-oscillating states (wherever applicable). As priors I have assigned a log-normal distribution to the energy parameter biased via χ^2_{aug} which forces the parameters to be positive and thus, significantly improves the stability of the fit. We fit up to the 7th exponential and the final results are taken from this, although the ground state fits are reasonably stable after the 3rd exponential. The mean values of the fit results with N exponentials are used as priors for the fit with $N + 1$ exponentials.

In the case of the cl-cl and the H-cl η_S mesons, we generated a 2×2 matrix of two-point correlators (shown in Figures 3.9 and 3.10), using four combinations of the operators γ_5 and $\gamma_5\gamma_4$ at the source and the sink. Fitting the 2×2 matrix of correlators simultaneously with multiexponential Bayesian [65] fitting methods helps

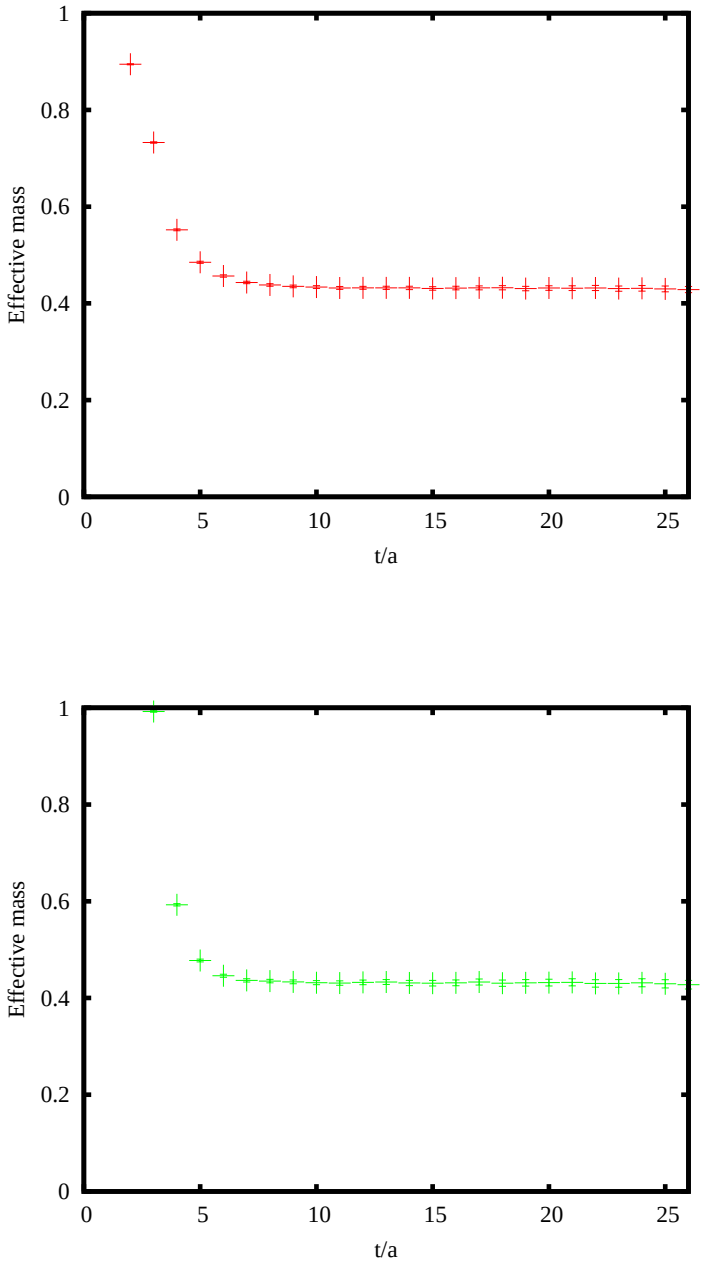

Figure 3.8: Example plots for the effective mass of the H-H (top) and the cl-cl (bottom) η_s mesons on the $m_l/m_s = 0.2$ coarse lattice.

us to obtain a more precise η_s ground state. The ground state amplitude of the η_s meson is extracted from the symmetric correlators arising from the use of the operator $\gamma_5\gamma_4$ at both ends which relates to the temporal axial current. The general fit form for the cl-cl symmetric η_S correlators is the same as in equation 2.45, while for the antisymmetric correlators (with γ_5 at one end and $\gamma_5\gamma_4$ at the other) it is

$$G(t) = \sum_{k=0}^{n_{\rm exp}} a_k^1 a_k^2 (e^{-E_k t} - e^{-E_k(T-t)}). \tag{3.21}$$

Here E_k, t and T carry the same meanings as before. a_k^1 and a_k^2 give the amplitudes at the source and sink respectively for the k-state of the meson. In addition to these symmetric and antisymmetric correlators, the H-cl η_S mesons include oscillations and the fit form for the oscillating symmetric correlators becomes the same as in equation 2.46.

The antisymmetric H-cl η_S correlator is similarly fitted with the form

$$\begin{aligned} G(t) &= \sum_{k=0}^{n_{\rm exp}} a_k^1 a_k^2 (e^{-E_k t} - e^{-E_k(T-t)}) \\ &\quad -(-1)^{t/a} \sum_{ko=0}^{n_{\rm exp}} a_{ko}^1 a_k^2 o(e^{-E_{ko} t} - e^{-E_{ko}(T-t)}). \end{aligned} \tag{3.22}$$

The cl-cl and the H-cl ϕ mesons are built with only symmetric operator combinations at both ends with the operator being the local vector. The H-cl ϕ meson correlators contain oscillations whereas the cl-cl ϕ does not. Therefore, the fit form for the cl-cl ϕ correlators is the same as for the cl-cl symmetric η_s and is given by the equation 2.45. Similarly, the H-cl ϕ is fitted with the equation 2.46, the same fit form used for the H-cl η_s.

The amplitudes of the three-point correlators are extracted from the simultaneous fits of the two-point and three-point correlators. For the H-H three-point current we have a H-cl η_s at both the source and the sink. Therefore, this three-point correlator

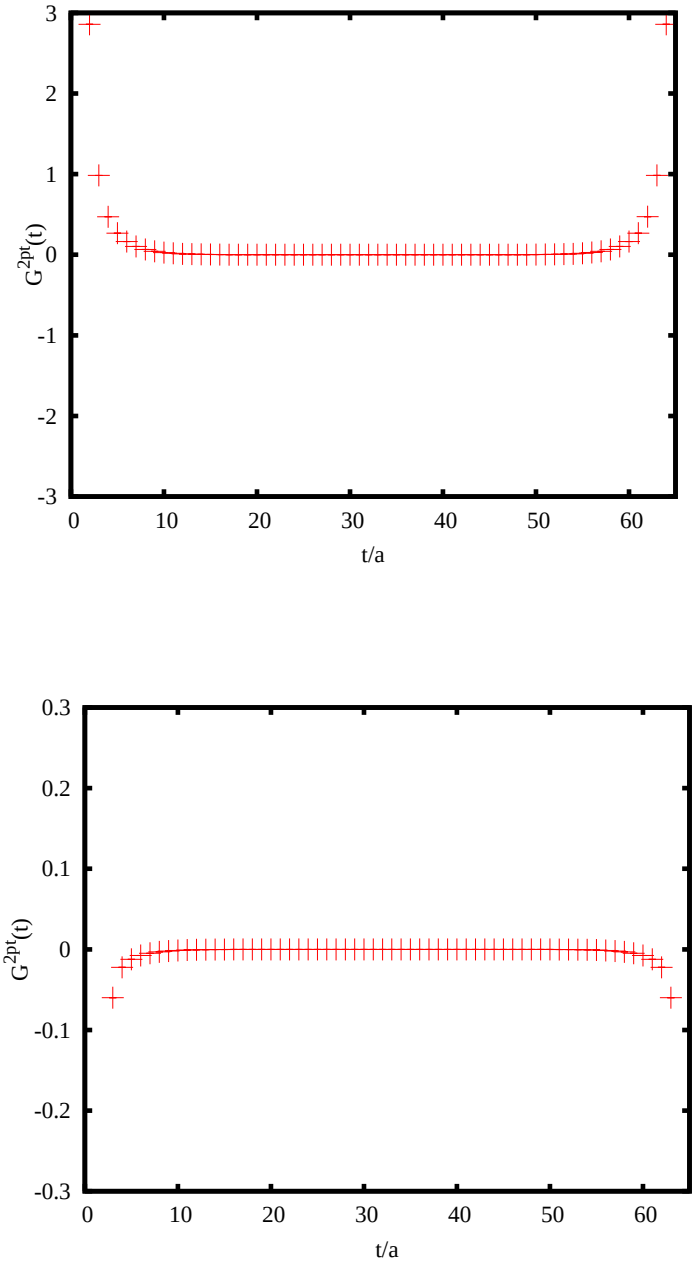

Figure 3.9: Average two-point correlators using clover fermion action for η_s meson: for both source and sink γ matrices are γ_5 (top); and $\gamma_5\gamma_4$ (bottom). These are symmetric correlators.

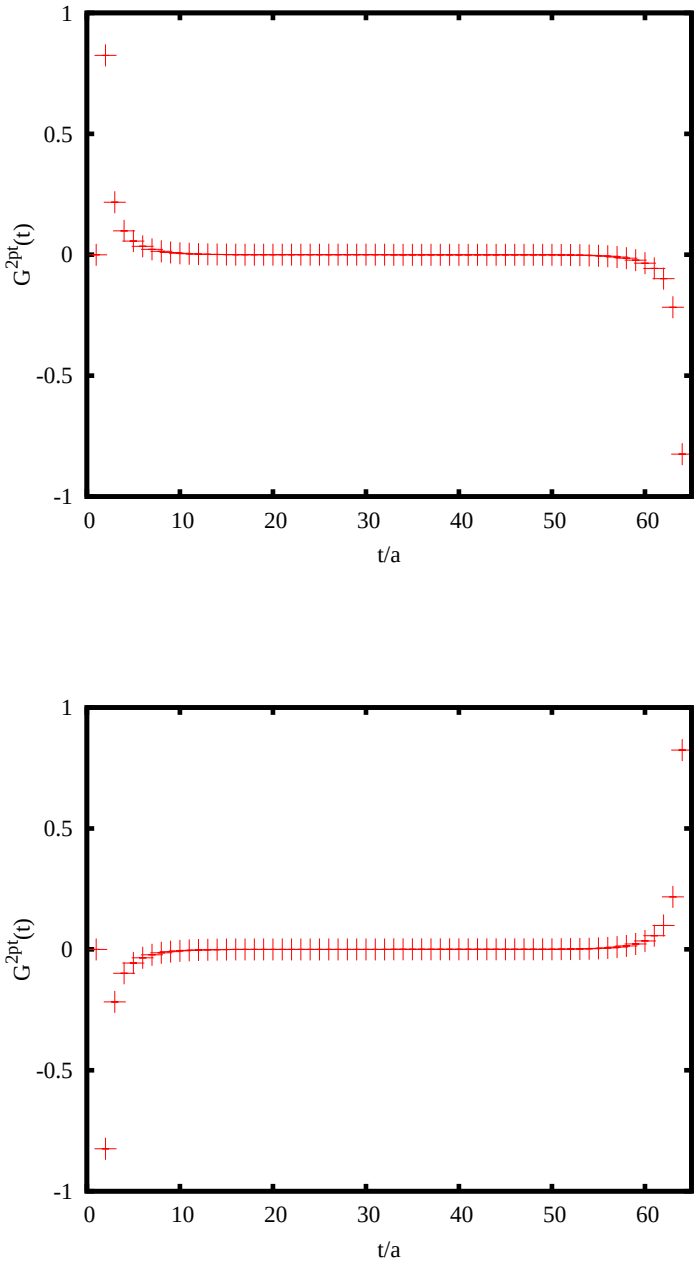

Figure 3.10: Average two-point correlators using clover fermion action for η_s meson: γ_5 at the source and $\gamma_5\gamma_4$ at the sink (top); $\gamma_5\gamma_4$ at the source and γ_5 at the sink (bottom). These are antisymmetric correlators.

has oscillations at both its ends and its fit form can be written in similar way to equation 2.47.

$$\begin{aligned} G^{\rm 3pt}(t;T) &= \sum_{i,j} a_i b_j V_{ij}^{nn}(e^{-E_{a,i}t} + e^{-E_{b,j}(T-t)}) \\ &- (-1)^{t/a} \sum_{i',j'} ao_{i'} b_{j'} V_{i'j'}^{on}(e^{-Eo_{a,i'}t} + e^{-Eo_{b,j'}(T-t)}) \\ &- (-1)^{t/a} \sum_{i',j'} a_{i'} bo_{j'} V_{i'j'}^{no}(e^{-E_{a,i'}t} + e^{-Eo_{b,j'}(T-t)}) \\ &+ (-1)^{t/a} \sum_{i',j'} ao_{i'} bo_{j'} V_{i'j'}^{oo}(e^{-Eo_{a,i'}t} + e^{-Eo_{b,j'}(T-t)}). \end{aligned} \tag{3.23}$$

The notations used in this equation are as follows. By, i, j we denote the number of exponentials ($n_{\rm exp}$) for the normal states of the mesons a at the source and b at the sink, whereas i', j' denote $n_{\rm exp}$ for the oscillating meson states. a and b are the normal state amplitudes at the source and sink and for oscillating state amplitudes we use ao and bo. When used as subscripts a and b denote whether we are talking about source or sink. E and Eo are the energies of the normal and oscillating states of the mesons and their subscripts in the equation are self-explanatory. V represents the three-point amplitudes and the superscripts n and o represent non-oscillating and oscillation states at the source and sink and we have a 2×2 combination for that.

For the cl-cl currents the three point correlators do not show any oscillations and the fit function in the simplest form [51] is given by

$$G_{\rm 3pt} = \sum_{i,j} a_i b_j V_{ij}(e^{-E_{a,i}t} + e^{-E_{b,j}(T-t)}). \tag{3.24}$$

The three-point correlators in case of the H-cl local vector current has an oscillatory contribution at the sink (H-cl η_s), but not at the source (cl-cl η_s). The fit function in this case (for H-cl η_s at the sink and cl-cl η_s at the source) can be mathematically expressed as

$$\begin{aligned} G^{\rm 3pt}(t;T) &= \sum_{i,j} a_i b_j V_{ij}^{nn}(e^{-E_{a,i}t} + e^{-E_{b,j}(T-t)}) \\ &- (-1)^{t/a} \sum_{i',j'} a_{i'} bo_{j'} V_{i'j'}^{no}(e^{-E_{a,i'}t} + e^{-Eo_{b,j'}(T-t)}) \end{aligned} \tag{3.25}$$

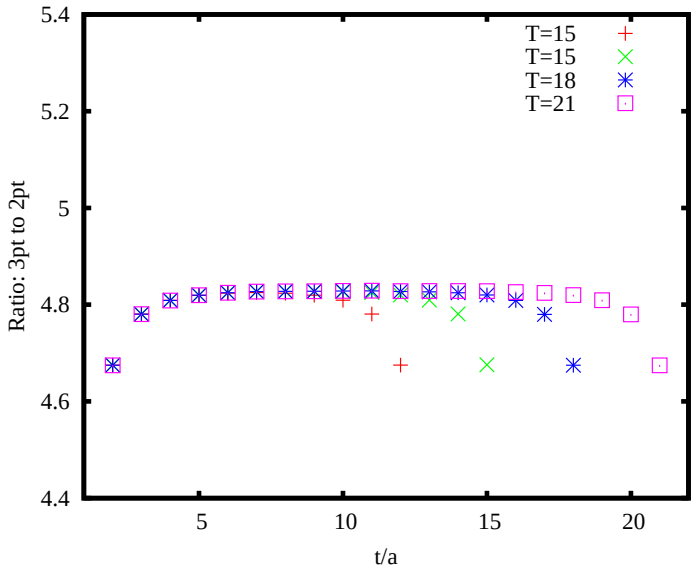

Figure 3.11: The ratios of the average three-point correlator to the average two-point correlator show a plateau at the same value for four different Ts, $T = 12, 15, 18, 21$ (using cl-cl current on the $m_l/m_s - 0.2$ coarse ensemble)

where the distance between the source and the sink is taken as T and the local vector current is inserted between the source and the sink at a distance t from the source. a_i and b_j are the same two-point amplitudes used earlier and the same for the cl-cl and the H-H cases. All other notations carry the usual meanings as described earlier. We end up with $a_i = b_i$ for the H-H and cl-cl currents since we have the same η_s at both the ends. The part V_{ij} of the three-point amplitude corresponds to the matrix element of the local vector current between the mesons at the source and the sink. Note that we shift the source time to $t = 0$ for all correlators.

$Z_{V^4_{qq}}$ is well-defined since the ratio of the average three-point correlator to the average two-point correlator gives a plateau with the same value over a time range T (the cl-cl case is shown in Figure 3.11 with a plateau value of ~ 4.81) for all the four T values used in the simulation for each t_0. Thus Z_{V^4} was obtained for the cl-cl, the H-H and the H-cl local vector currents and listed in Table 3.6.

I have used the same η_S priors for all the three cases - H-H, cl-cl and cl-H _ since we expect all lattice formalisms to give similar results on the lattice for physical quantities (small differences may arise from the discretisation effects). The η_s priors (energies in units of GeV; the prior widths in the paranthesis) for the non-oscillating piece used in the fits are given by

$$\begin{aligned} \log(E^{\eta_s}_{(0)}) &= \log(0.65(22)) && (3.26)\\ \log(E^{\eta_s}_{(n)} - E^{\eta_s}_{(n-1)}) &= \log(0.48(24)) \quad (n > 0) && (3.27)\\ a^{\eta_s}_{(0)} &= 0.01(1.0). && (3.28) \end{aligned}$$

where $\log(E^{\eta_s}_{(0)})$ and $\log(E^{\eta_s}_{(n)} - E^{\eta_s}_{(n-1)})$ are respectively the ground state energy and the energy difference between two consecutive states fed as log-normal distributions in the fit. And $a^{\eta_s}_{(0)}$ is the ground state amplitude. The priors are same for all lattice spacings.

For the H-cl oscillating priors for η_s, following a similar notation, I have used

$$\begin{aligned} ao^{\eta_s}_{(0)} &= 0.01(0.5) && (3.29)\\ \log(Eo^{\eta_s}_{(n)} - Eo^{\eta_s}_{(n-1)}) &= \log(0.48(24)) \quad (n > 0) && (3.30)\\ \log(Eo^{\eta_s}_{(0)}) &= \log(E^{\eta_s}_{(0)}) + (0.33(22)). && (3.31) \end{aligned}$$

For the three point amplitudes we assign

$$V^{nn} = 0.01(5.0), V^{on} = 0.01(1.0), V^{oo} = 0.01(1.0). \quad (3.32)$$

The ϕ priors for the H-H, the cl-cl and the cl-H currents using a similar notation as before are given as follows

$$\begin{aligned} \log(E^{\phi}_{(0)}) &= \log(1.10(4)) && (3.33)\\ \log(E^{\phi}_{(n)} - E^{\phi}_{(n-1)}) &= \log(0.76(38)) \quad (n > 0) && (3.34)\\ a^{\phi}_{(0)} &= 0.01(1.0) && (3.35)\\ ao^{\phi}_{(0)} &= 0.01(1.0) && (3.36)\\ \log(Eo^{\phi}_{(n)} - Eo^{\phi}_{(n-1)}) &= \log(0.76(38)) \quad (n > 0) && (3.37)\\ \log(Eo^{\phi}_{(0)}) &= \log(E^{\phi}_{(0)}) + (0.55(22)). && (3.38) \end{aligned}$$

In most of the fits I have used an svdcut [3] of 10^{-8}, though I used an svdcut of 10^{-6} for fitting the cl-cl three-point functions. I have obtained excellent fits with a χ^2 per degree of freedom [4] between $0.5 - 0.9$ and p-values between $0.7 - 0.9$ using the above mentioned priors and fit range described before.

3.6 Results

3.6.1 The properties of the η_s and the discretisation effects

The valence strange quark masses and the clover κ have been tuned accurately to get the correct η_s mass. We have also used the same HISQ and clover propagators for making the H-cl correlators. From this procedure we get a different (slightly higher) η_s mass which is a discretisation effect and so this difference should vanish in the continuum. Table 3.2 lists the η_s masses, the ground state amplitudes and the decay constants for all three correlator formalisms and on all three ensembles relevant to the calculation of the Z factors. The lattice spacing dependence of the η_s mass difference between the Goldstone H-H case and the H-cl case is shown in Figure 3.12 and extrapolated to the $a = 0$ continuum limit where the difference vanishes (up to the uncertainty).

In Figures 3.13 and 3.14 the effective amplitudes, i.e. the ratios of the correlator to its ground state for the Goldstone H-H and cl-cl η_s, have been compared on two different lattice spacings. We can clearly see from these plots that the excited states of the two-point correlators almost die down from around lattice time ~ 10 as the effective amplitude approaches unity. At small times the H-H and cl-cl have different

[3] In a least squares fitting technique, for the Singular Value Decomposition (SVD) of the correlation matrix, if an eigen value of the matrix is smaller than an assigned number called svdcut then that eigen value is substituted by the svdcut and the matrix becomes more singular.

[4] The number of degrees of freedom in a least square Bayesian fit equals the number of fit parameters subtracted from the total number of the pieces of data and the priors.

Table 3.2: The lattice results for the two point correlator fits for HISQ, clover and H-cl mixed actions : the mass (m_{η_s}) and the ground state two-point amplitudes a_0 (for temporal axial current in the cl-cl and H-cl case) and b_0 (for pseudoscalar current in the H-H case) on each ensemble. The H-H results are from 1004 configurations where cl-cl and H-cl results are from $\sim$ 500 configurations. Also, HISQ results are from the simultaneous fits of the HISQ Goldstone (i.e. γ_5 at source and sink) and nongoldstone (i.e. $\gamma_5\gamma_4$ at source and sink) fits. Clover results are given from combined clover and HISQ 2×2 correlator fits since we calculated the Z factors in this fit. H-cl results are also obtained in a similar way. Column 6 gives the η_s decay constant in lattice units for the H-H case where it is absolutely normalised. Column 7 gives the un-normalised η_s decay constant for the cl-cl and H-cl cases. Column 8 gives the Z factors for the cl-cl and H-cl cases from setting the decay constant equal to that in the H-H case. They are obtained from simultaneous fits to the two sets of correlators so that correlated uncertainties are taken into account.

Set	Action	am_{η_s}	m_{η_s}(MeV)	a_0	f_{η_s}	f_{η_s}/Z_A	Z_A
1	HISQ	0.540243(151)	691.15(20)	0.2839(2)	0.1426(1)	-	-
	clover	0.540100(300)	690.96(40)	1.5471(31)	-	0.1965(3)	0.7275(21)
	H-cl	0.573330(400)	733.49(52)	0.5659(7)	-	0.1629(5)	0.8775(34)
4	HISQ	0.431329(91)	686.16(15)	0.2111(1)	0.1140(1)	-	-
	clover	0.431400(200)	686.28(33)	1.1499(9)	-	0.1522(3)	0.7487(14)
	H-cl	0.446800(300)	710.78(49)	0.4314(4)	-	0.1293(3)	0.8817(23)
9	HISQ	0.313879(76)	681.44(17)	0.1370(1)	0.0829(1)	-	-
	clover	0.313200(200)	679.98(44)	0.7332(7)	-	0.1066(2)	0.7777(18)
	H-cl	0.318122(150)	690.66(33)	0.2877(3)	-	0.0933(1)	0.8879(13)

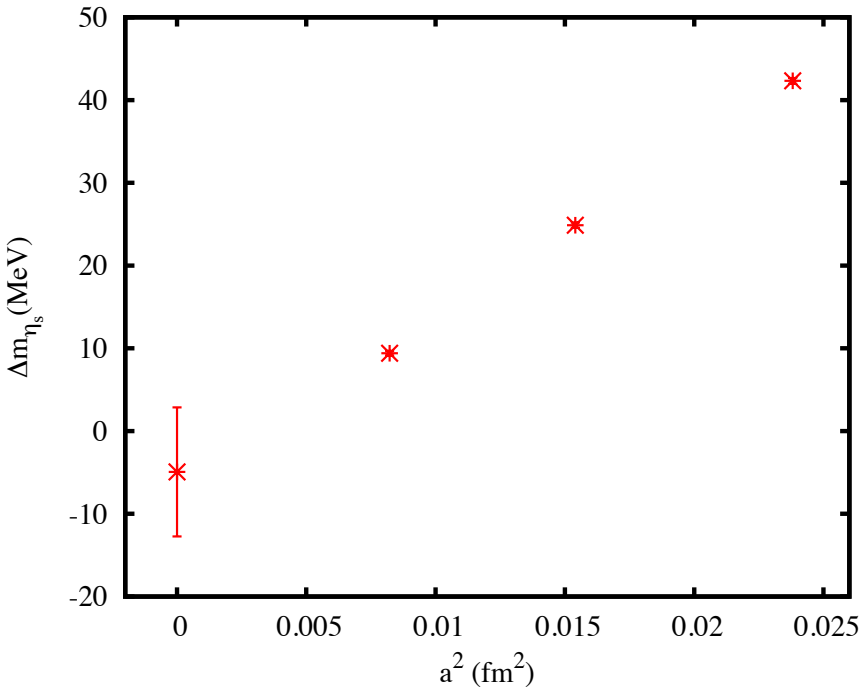

Figure 3.12: This plot shows the difference in mass between the Goldstone H-H η_s and the H-cl η_s is a discretisation effect which goes away in the continnum.

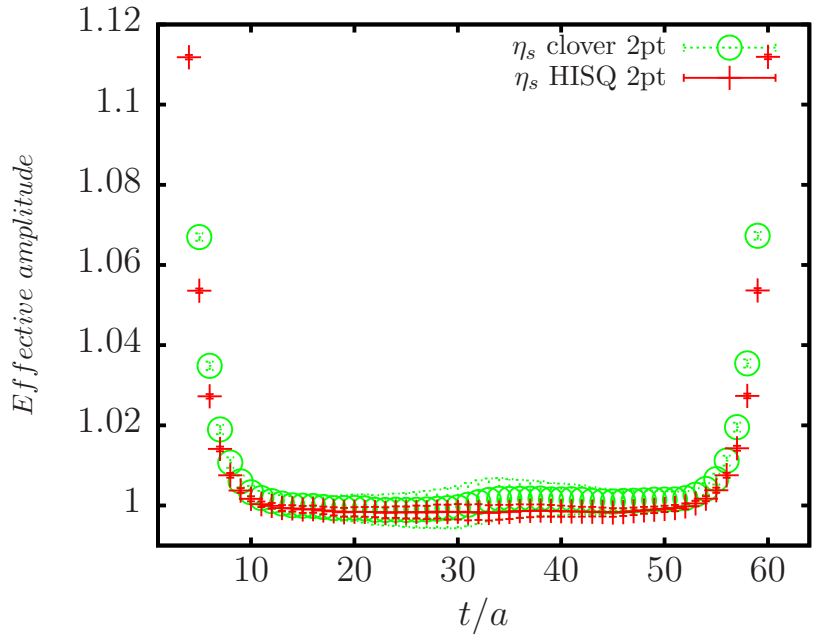

Figure 3.13: This plot compares the effective amplitude i.e. the ratio of the correlator to its ground state for the Goldstone H-H and the cl-cl η_S on the ensemble set '4'. We can clearly see from here that ground state in both correlators dominates for large lattice time ≥ 10.

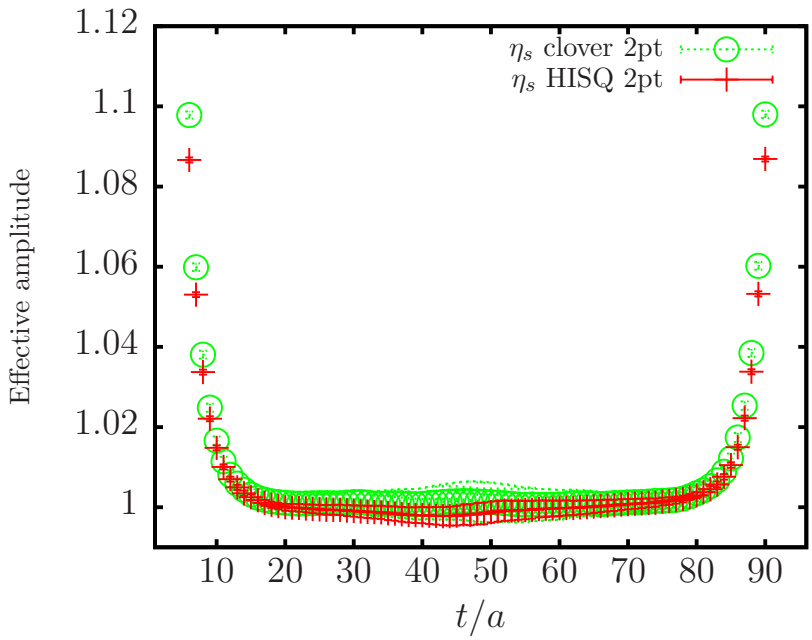

Figure 3.14: This plot compares the effective amplitude i.e. the ratio of the correlator to its ground state for the Goldstone H-H and the cl-cl η_S on the ensemble set '9'. We can clearly see from here that ground state in both correlators dominates for large lattice time ≥ 10.

effective amplitudes, they become equivalent at larger times. And the fact that they match with each other away from the mid-plateau region confirms that the excited state contributions enter both sets of correlators in a similar way. Note that the H-H correlators are more precise because for the cl-cl calculation on these ensembles only half of the configurations compared to the H-H calculation have been used. If we use same number of configurations in the H-H and cl-cl case, the uncertainties would be similar and we do not gain more precision from the fact that clover quarks have four spin components.

From the plots in Figures 3.13 and 3.14, another interesting observation is that the statistical uncertainties in the correlators i.e. the noise increases with the increasing source-sink time separation. The variance of the meson correlator is a correlator made

Table 3.3: The results for the properties of the H-H Goldstone η_S on the physical point lattices: the lattice mass, the mass in GeV, the ground state amplitude and the lattice decay constant (only statistical uncertainties are given).

Set	am_{η_s}	m_{η_s} (MeV)	a_0	af_{η_s}
3	0.526517(59)	688.62(363)	0.2776(1)	0.1393(1)
8	0.423049(37)	688.71(363)	0.2059(1)	0.11150(3)
11	0.304839(30)	684.83(366)	0.13320(3)	0.08060(1)

of two quarks and two antiquarks. For two different quark flavors a and b

$$\begin{aligned} \text{Signal} &\sim \exp\left(-M_{ab}t\right) \\ \text{Noise} &\sim \exp\left(-\frac{(M_{aa}+M_{bb})}{2}t\right) \\ \frac{\text{Signal}}{\text{Noise}} &\sim \exp\left(-(M_{ab}-\frac{M_{aa}+M_{bb}}{2})t\right) \end{aligned} \tag{3.39}$$

Therefore, the noise increases with the number of time slices when there is a mass difference between the two quarks. But it is usually expected that the signal-to-noise ratio is constant for a pseudoscalar meson containing quarks of the same mass, for example, η_s. However, when the quark masses are the same the Wick contraction has both direct and crossed terms. If we ignore the effects of crossed terms and the interaction between the two mesons then the ground state energy of this system is equal to twice the mass of the meson which controls the signal. But the two effects i.e. no cross terms and no interaction between the mesons, cause the mass controlling the noise to fall below the mass controlling the signal, thus giving an exponential fall in the signal-noise ratio even in case of η_s [26].

For H-H correlators, the η_s and the ϕ have been studied on a more complete set of ensembles. On ensembles with physical dynamical light quarks the η_s results are given in Table 3.3 and the three different volume results are shown in Table 3.4. We should note that even if we use the PCAC relation and relate the pseudoscalar current operator to the temporal axial current operator, we do not actually form an η_s using the PCAC temporal axial current. This current for HISQ is point-split, therefore

Table 3.4: The results for the properties of the H-H η_S for three volumes on $m_l/m_s = 0.1$ coarse ensemble: tuned valence strange quark masses, the lattice mass, the mass in GeV, the ground state amplitude, the lattice decay constant and the decay constants in GeV.

Set	$m_s^{\text{val,tuned}}$	am_{η_s}	m_{η_s} (MeV)	$a_0(\eta_s)$	af_{η_s}	f_{η_s} (MeV)
5	0.0533	0.42665(9)	689.0(1)	0.20810(12)	0.11257(4)	184.5(1)
6	0.0507	0.41572(14)	671.3(2)	0.20767(40)	0.11110(17)	179.4(3)
6	0.0533	0.42637(6)	688.5(1)	0.20763(8)	0.11243(5)	181.6(4)
6	0.0534	0.42687(15)	689.3(2)	0.20736(48)	0.11230(19)	183.7(3)
7	0.0533	0.42641(4)	688.6(1)	0.20777(7)	0.11249(3)	181.7(1)

Table 3.5: The results for the properties of the local non-Goldstone H-H η_s meson (taste $\gamma_5\gamma_4$): lattice mass, un-normalised decay constant and the temporal axial current renormalisation.

Set	Action combination	am_{η_s}	af_{η_s}/Z_{A^4}	Z_{A^4}
1	H-H $(\gamma_5\gamma_4 \otimes \gamma_5\gamma_4)$	0.5605(3)	0.14094(19)	1.0147(37)
4	H-H $(\gamma_5\gamma_4 \otimes \gamma_5\gamma_4)$	0.4396(2)	0.11355(15)	1.0039(13)
9	H-H $(\gamma_5\gamma_4 \otimes \gamma_5\gamma_4)$	0.3157(1)	0.08303(8)	0.9981(11)

very complicated to calculate and also unnecessary as we can form the pseudoscalar current easily. However, to explicitly test the temporal axial current we use the local non-Goldstone operator as discussed in earlier sections. The masses of these mesons are slightly heavier than the masses of the Goldstone mesons, though both are formed with the same tuned s quark mass. The masses and the un-normalised decay constants for these non-Goldstone η_s mesons are given in Table 3.5. From comapring these un-normalised decay constants with the ones from H-H Goldstone η_s decay constants we have extracted the temporal axial current renormalisations given in Table 3.5.

3.6.2 Results for Z factors

The results of the Z_{A^4} and Z_{V^4} factors for the H-H, the cl-cl and the H-cl currents are given in Table 3.6. We see from Table 3.6, that the values of Z_{A^4} and Z_{V^4} are close to each other for the H-H, cl-cl and H-cl formalisms. Since the HISQ action posseses a remnant chiral symmetry, the equality of Z_{A^4} and Z_{V^4} for the H-H case is natural. However, the clover action does not have chiral symmetry, yet the difference of these two renormalisations is negligibly small on the very coarse lattice. Another point to note is that Z_{A^4} calculated from equations 3.3 and 3.5 differ slightly which is a discretisation effect.

3.6.3 Results for ρ factors

In Table 3.6 we have now all the ingredients for testing ρ_{A^4} and ρ_{V^4}. Using our results for $Z_{A^4_{\mathrm{H-cl}}}$ and $Z_{V^4_{\mathrm{H-H/cl-cl}}}$ and equation 3.1 we can determine $\rho_{A^4_{\mathrm{H-cl}}}$. We have extracted $\rho_{V^4{}_{\mathrm{H-cl}}}$ also from a similar relation written as $Z_{V^4{}_{\mathrm{H-cl}}} = \rho_{V^4{}_{\mathrm{H-cl}}} \sqrt{Z_{V^4{}_{\mathrm{cl-cl}}} Z_{V^4{}_{\mathrm{H-H}}}}$. Our results of $\rho_{A^4{}_{\mathrm{H-cl}}}$ and $\rho_{V^4{}_{\mathrm{H-cl}}}$ are listed in Table 3.6. They are indeed close to 1, with a maximum deviation of $\sim 3\%$ on the very coarse lattice. This is consistent with the Fermilab hypothesis and $\rho_{A^4{}_{\mathrm{H-cl}}}$ and $\rho_{V^4{}_{\mathrm{H-cl}}}$ are even closer to each other on the finer lattices.

Our results for $\rho_{A^4{}_{\mathrm{H-cl}}}$ have been compared to the Fermilab/MILC results for the clover-Asqtad mixed action using their one-loop perturbative coefficients at two different values of the clover quark masses (shown in Figure 3.15). The equivalent perturbative results for the H-cl could be different because the asqtad and the HISQ are different formalisms. Therefore, we can only compare our results with the Fermilab results qualitatively. We find that ρ_{A^4} and ρ_{V^4} from our calculation and the Fermilab calculation have similar values and behave in the similar way with respect to lattice spacings. On the finer lattices, our non-perturbative result agrees with the perturbative

Table 3.6: Our results for f_{η_s}, Z_{A^4}, Z_{V^4}, ρ_{A^4} and ρ_{V^4} for the H-H, cl-cl and the H-cl cases on the ml/ms = 0.2 gauge emsembles; the operator is $\gamma_5\gamma_4$ at the source and the sink for which the renormalisation is considered. The local Pseudoscalar current has been used in the H-H case for renormalisation of the non-Goldstone current which is why $Z_{A^4}^{H-H}$ is not exactly equal to unity. For the all the quantities the uncertainties are given in the parentheses and should be read in the last digits.

Set	Combinations	af_{η_s}	Z_{A^4}	Z_{V^4}	ρ_{A^4}	ρ_{V^4}
1	H-H	0.140942(193)	1.0147(37)	0.9872(39)	-	-
	Cl-Cl	0.697776(1128)	0.7275(21)	0.7261(7)	-	-
	Cl-H	0.306971(918)	0.8670(8)	1.0365(46)	1.0240(23)	
4	H-H	0.113547(146)	1.0039(13)	0.9932(22)	-	-
	Cl-Cl	0.544045(936)	0.7487(14)	0.7402(4)	-	-
	Cl-H	0.244357(607)	0.8817(23)	0.8734(15)	1.0283(28)	1.0187(21)
9	H-H	0.083028(80)	0.9981(11)	0.9946(17)	-	-
	Cl-Cl	0.384396(789)	0.7777(18)	0.7629(21)	-	-
	Cl-H	0.177261(262)	0.8879(13)	0.8898(19)	1.0194(23)	1.0215(28)

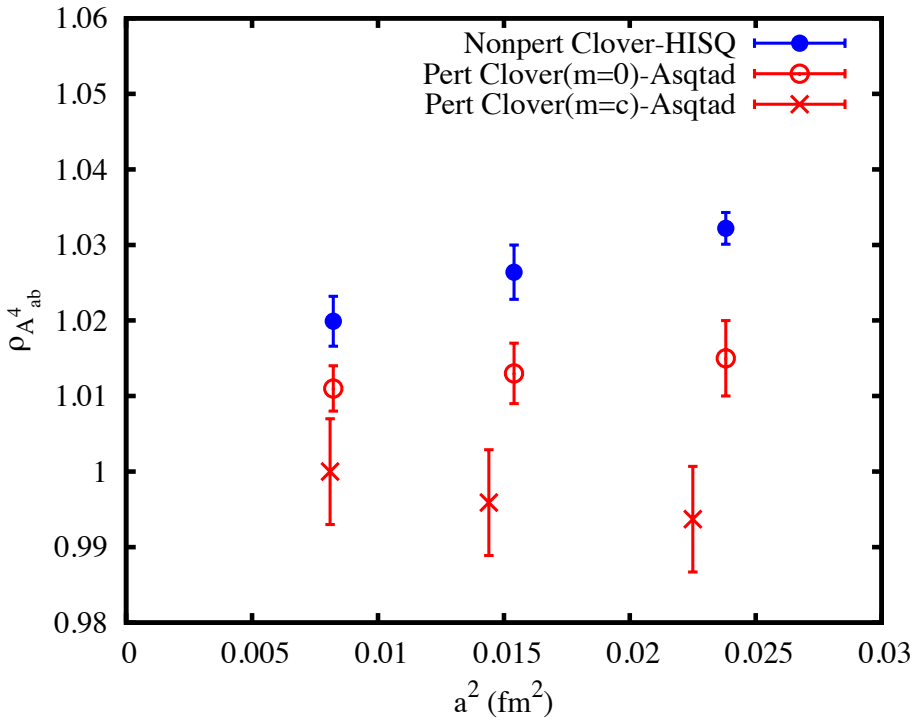

Figure 3.15: Our results for $\rho_{A^4{}_{H-cl}}$, plotted against the square of the lattice spacings are compared to the one-loop results from the Fermilab-MILC for the mixed clover-Asqtad currents with the clover charm (crosses) and the clover light (open circles) quarks.

result to within 1%, whereas our result is 2% away and the perturbative result is 1% away from unity. Assuming that the H-cl perturbative results will behave in the same way to the clover-Asqtad case, we have confirmed that all higher order ρ coefficients should be small.

We performed a similar analysis and the comparison of the non-perturbative results for $\rho_{V^4{}_{\mathrm{H-cl}}}$ with Fermilab/MILC results is depicted in Figure 3.16. We draw a similar conclusion that in this case also the ρ coefficients are small for each order in the perturbation series.

We used two completely independent lattice formalisms, HISQ and clover, to get Z_A^4 and Z_V^4 or ρ_A^4 and ρ_V^4. Therefore, our results are completely robust.

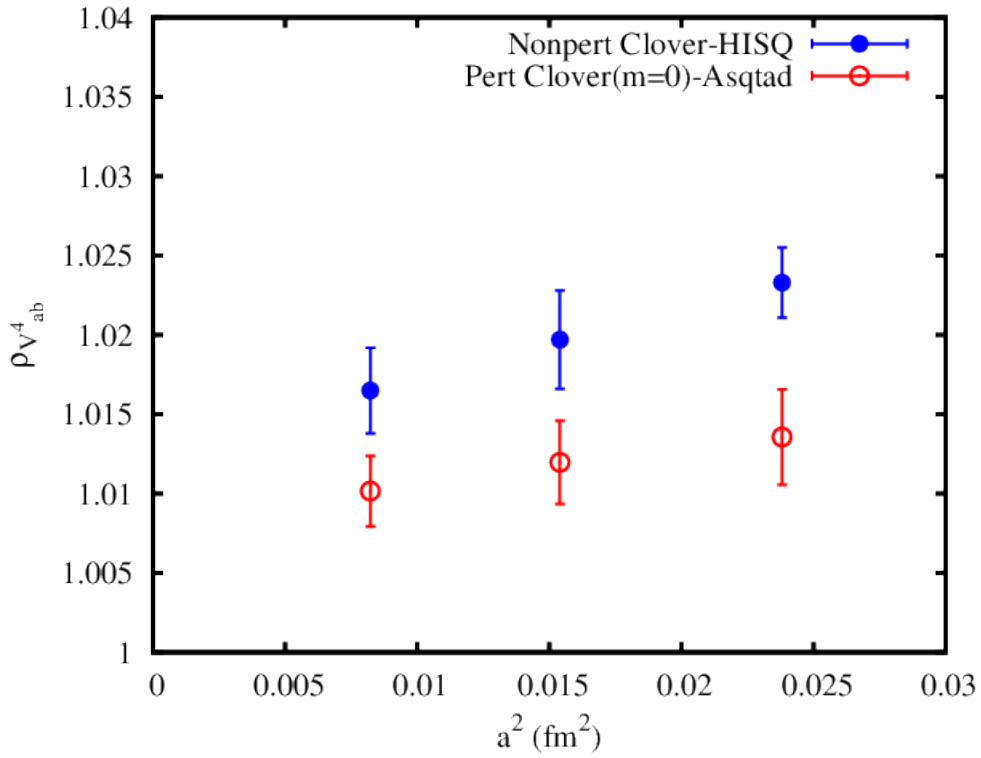

Figure 3.16: Our results for $\rho_{V^4{}_{H-cl}}$, plotted against the square of the lattice spacing, are compared to the one-loop results from the Fermilab-MILC for the mixed clover-Asqtad currents.

3.6.4 Mass and decay constant for the ϕ

So far I have used two different independent relativistic formalisms HISQ and clover, combining them into three correlators. It is worth comparing the discretisation errors coming from these fomalisms and for this purpose I have made the vector meson ϕ from one valence $s\bar{s}$ pair where both of them are HISQ quarks, both of them are clover quarks and then mixing one HISQ and one clover quark. I have used the same strange propagators as in the case of the η_s and studied the two-point ϕ correlators as before to extract the mass of the ϕ meson (m_ϕ) on each ensemble. We calculate the decay constant f_ϕ using the equation

$$f_\phi = Z_{V^4} \times a_0 \sqrt{\frac{2}{m_\phi}} \tag{3.40}$$

where a_0 is the ground state amplitude of the two-point correlators. Since these are vector correlators, we do find oscillations in the case of the pure HISQ formalism unlike for the η_s. The ϕ correlators are a lot noisier than the η_s correlators, giving rise to larger uncertainties in the ϕ meson properties compared to the η properties. m_ϕ and f_ϕ are listed in Table 3.7 as calculated on the $m_l/m_s = 0.2$ ensembles. To test the effects of the masses of the light dynamical quarks in our ϕ results we also use a more complete set of ensembles for the H-H case: the ϕ results on the physical m_l ensembles are given in Table 3.8. The results for the ϕ on the three volumes with $m_l/m_s = 0.1$ are given in Table 3.9 showing negligible volume dependence. Figure 3.17 indicates negligible finite volume dependence of the η_s and ϕ masses. Therefore, we do not need to worry about the finite volume correction in this case whereas later we will see this becomes important in case of the vector mesons made of light valence quarks.

Table 3.7: The results for the mass of the ϕ meson (m_ϕ) and its decay constant f_ϕ: columns 1 and 2 indicate the gauge configuration set number and the corresponding lattice spacing squared; columns 3, 4, 5 and 6 respectively give the mass of ϕ meson, the ground state amplitude, the un-normalised ϕ decay constant and the normalised ϕ decay constant in lattice units; columns 7 and 8 list the ϕ decay constants and the difference in the masses of the ϕ and η_s mesons in physical units of MeV (uncertainities given in the parantheses and should be read in the last digits) for three ensembles using H-H, cl-cl and H-cl formalisms.

Set	a^2 (fm^2)	Action	am_{ϕ_s}	$a_0(\phi)$	af_{ϕ_s}/Z_V	af_{ϕ_s}	f_{ϕ_s}(MeV)	$m_{\phi_s} - m_{\eta_s}$ (MeV)
1	0.02379	HISQ	0.8166(38)	0.1260(28)	0.19722(41)	0.1947(40)	249.1(53)	353.5(52)
		clover	0.7804(18)	0.6519(67)	1.0440(98)	0.2135(20)	273.1(29)	308.0(29)
		H-cl	0.8023(23)	0.2807(37)	0.4434(52)	0.2040(24)	260.9(34)	293.0(34)
4	0.01539	HISQ	0.6517(25)	0.0871(14)	0.15294(23)	0.1519(23)	239.3(55)	343.9(49)
		clover	0.6299(26)	0.4387(96)	0.7817(155)	0.1619(32)	257.6(53)	315.8(45)
		H-cl	0.6414(24)	0.1921(37)	0.3392(61)	0.1567(28)	249.3(46)	309.4(42)
9	0.00826	HISQ	0.4733(13)	0.0547(7)	0.1124(13)	0.1118(13)	242.7(32)	346.0(35)
		clover	0.4650(15)	0.2658(34)	0.5513(68)	0.1166(14)	253.0(33)	331.1(32)
		H-cl	0.4683(16)	0.1171(18)	0.2420(32)	0.1134(15)	246.1(36)	325.9(40)

Table 3.8: The results for ϕ mass and decay constant on the physical point lattices for the H-H case : columns 1 and 2 indicate the gauge configuration set number and the corresponding lattice spacing squared; columns 3, 4, 5 and 6 respectively give the mass of ϕ meson, the ground state amplitude, the un-normalised ϕ decay constant and the normalised ϕ decay constant in lattice units; columns 7 and 8 list the ϕ decay constants and the difference in the masses of the ϕ and η_s mesons in physical units of MeV (uncertainities given in the parantheses and should be read in the last digits).

Set	a^2 (fm^2)	am_{ϕ_s}	a_0	af_{ϕ_s} (without Z_V)	af_{ϕ_s}	f_{ϕ_s}(MeV)	$m_{\phi_s} - m_{\eta_s}$ (MeV)
3	0.02276	0.7969(9)	0.1230(6)	0.1949(14)	0.1924(11)	251.6(19)	353.6(22)
8	0.01469	0.6337(9)	0.0849(6)	0.1508(11)	0.1498(10)	243.8(21)	343.0(23)
11	0.00772	0.4557(8)	0.0511(3)	0.1070(6)	0.1064(6)	239.8(24)	339.0(26)

Table 3.9: The results for ϕ on three volumes at $m_l/m_s = 0.1$ and $a = 0.1222$fm with $m_s^{\text{tuned}} = 0.0533$ for the H-H case : columns 1 indicates the gauge configuration set number; columns 2, 4, 5 and 6 respectively give the mass of ϕ meson, the ground state amplitude, the un-normalised ϕ decay constant and the normalised ϕ decay constant in lattice units; columns 3 and 7 list the ϕ mass and decay constants in physical units of MeV (uncertainities given in the parantheses and should be read in the last digits).

Set	am_{ϕ_s}	m_{ϕ_s} (MeV)	$a_0(\phi)$	af_{ϕ_s} (without Z_V)	af_{ϕ_s}	f_{ϕ_s} (MeV)
5	0.6384(35)	1030.9(57)	0.0846(27)	0.1498(44)	0.1488(44)	240.3(70)
6	0.6394(12)	1032.5(20)	0.0860(8)	0.1522(13)	0.1512(12)	244.1(20)
7	0.6423(8)	1037.2(13)	0.0875(5)	0.1546(9)	0.1535(8)	247.8(13)

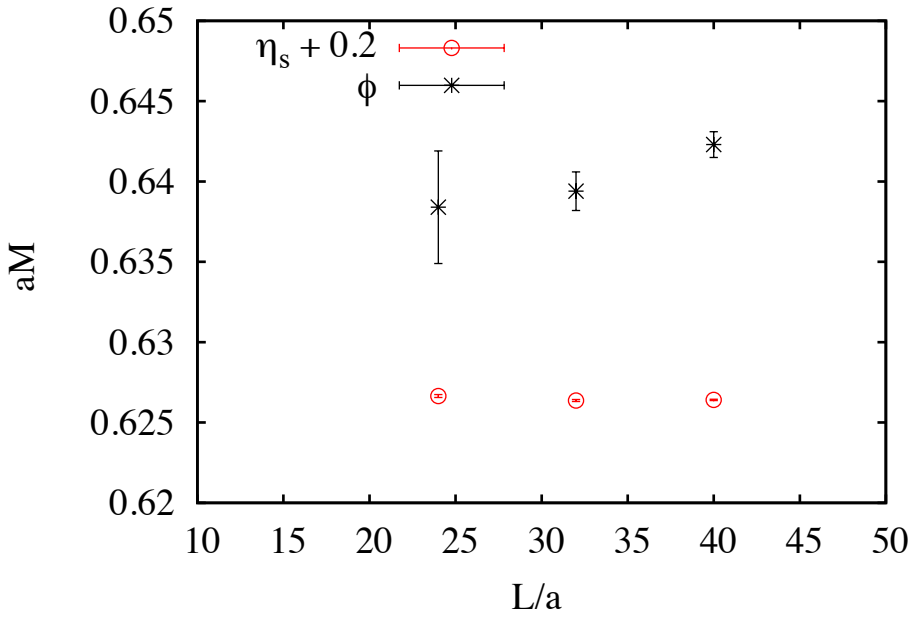

Figure 3.17: This figure shows negligible finite volume dependence of the η_s and ϕ masses on the $m_l/m_s = 0.1$ ensemble. Here 0.2 has been added to m_{η_S} so that it can be shown clearly on the same plot with m_ϕ.

3.6.5 Continuum extrapolation of ϕ properties

A good way to compare the discretisation errors is to study the mass gaps between the η_s and the ϕ with the lattice spacing for different formalisms and then to perform the continuum ($a = 0$) extrapolation to test whether all the schemes give the same physical result.

The fit function used to extrapolate the results from the H-H case is

$$f = c_0 + c_l \times m_{ls} + c_s \times \Delta m_{\eta_s} + c_2 \times (\lambda a)^2 + c_4 \times (\lambda a)^4 + c_6 \times \mathcal{O}(\lambda a)^6). \quad (3.41)$$

Here, the fit parameters are the coefficients c_0, c_l, c_s, c_2, c_4, and c_6. The fit form (in powers of lattice spacing) replicates the form of the discretised action. For example, in this case there are no odd powers of the lattice spacing in the fit function as the HISQ action does not contain them. Also, in the fit results we can find c_2 is negligibly small as HISQ action is $\mathcal{O}(a^2)$-improved. λ is the relevant QCD scale in our calculation which has been taken between $200 - 400$ MeV to get the best fit. The

priors for c_0 has been taken as 0.24(12) and for the rest of the coefficients in equation 3.41 the priors were taken as 0(1). The best fit results have been obtained with a $\chi^2 = 0.3 - 0.5$ and p-value of $0.5 - 0.7$.

Here,

$$m_{ls} = \frac{((2 \times m_l^{\rm sea} + m_s^{\rm sea}) - (2 \times m_l^{\rm phys} + m_s^{\rm phys}))}{m_s^{\rm phys}}; \quad (3.42)$$

$$\Delta m_{\eta_s} = m^2_{\eta_s,{\rm phys}} - m^2_{\eta_s,{\rm obtained}}. \quad (3.43)$$

The term 'm_{ls}' in the fit corrects for the heavier than physical sea light quark mass effects and the term 'Δm_{η_s}' corrects for the valence s quark mass mistuning effects (difference from the physical mass), though they are very small. We do not have any term in the fit $\sim \mathcal{O}(\alpha_s a)$ since the HISQ action is improved to have no $\mathcal{O}(\alpha_s a)$ discretisation and we tested for it by intentionally adding this term.

For the cl-cl and H-cl cases, in the fit function, we need to add odd powers of (λa) as well. The fit function in these cases looks like

$$\begin{aligned} f &= c_0 + c_l \times m_{ls} + c_s \times \Delta m_{\eta_s} + c_\alpha \times \alpha_s a + c_2 \times (\lambda a)^2 \\ &\quad + \alpha_s (\lambda a)^3 + c_4 \times (\lambda a)^4 + c_6 \times \mathcal{O}(\lambda a)^6). \end{aligned} \quad (3.44)$$

The priors are similar to the H-H case. Here, the major contributions come from the terms $\mathcal{O}(\alpha_s a)$ and $\mathcal{O}(\alpha_s a^3)$. Here also, the best fits have been obtained with a $\chi^2 = 0.3 - 0.5$ and p-value of$0.5 - 0.7$. The uncertainties we get in the extrapolations are correlated and account for both the fitting uncertainties and the statistical uncertainties.

From the extrapolation plot of $m_\phi - m_{\eta_s}$ in Figure 3.18 we see all the three methods of calculating correlators agree in the continuum limit as expected. The H-H discretisation errors are much smaller than the cl-cl and the H-cl discretisations. The accurate H-H results show a value in the continuum limit which is higher than the experimental value. The ϕ is not a "gold-plated meson" [5], having a strong decay

[5]Gold-plated mesons are well-characterised in experiments as they have narrow width with no strong two-body decay mode.

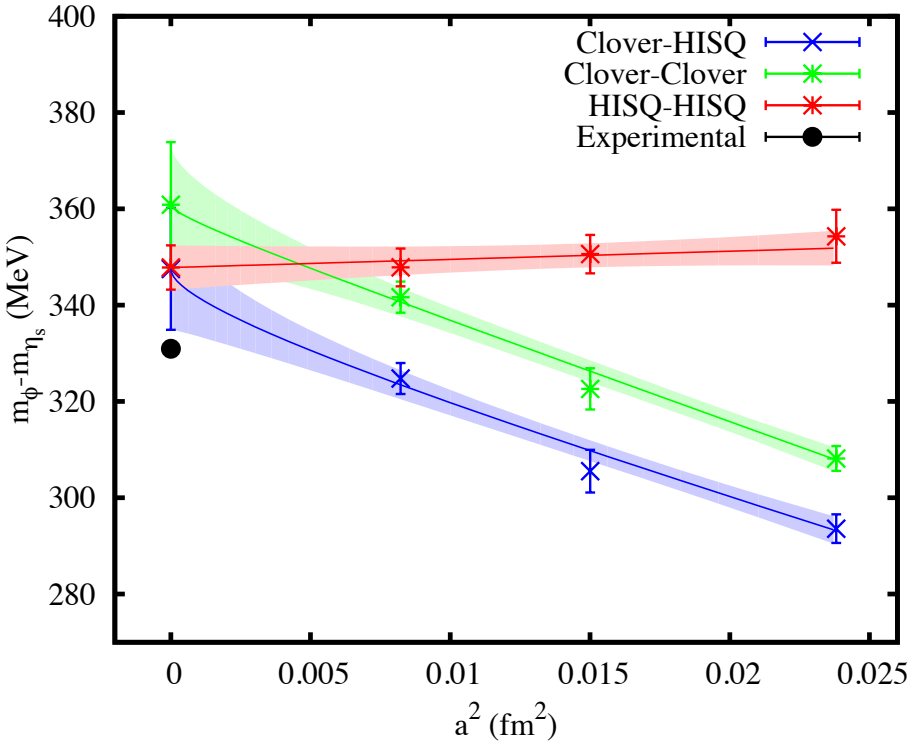

Figure 3.18: $m_\phi - m_{\eta_s}$ calculated with the different quark formalisms and extrapolated to $a = 0$.

to $K\overline{K}$ and further study is needed to uncover what the impact of this decay channel is on our results for m_ϕ and f_ϕ. Another physical quantity we have used to compare discretisation errors is the ϕ decay constant. This is also plotted as a function of the lattice spacing in Figure 3.19 with an extrapolation to the continuum for all the three formalisms. As before, we find that all the discretisations agree in the continuum and again the H-H case shows the smallest discretisation errors. In the H-H case, the lattice f_ϕ result in the continuum match with the experimental result obtained from $\Gamma(\phi \to e^+e^-)$ [66] up to 1.5σ.

For calculating the experimental value of the decay constant, we consider the $\phi \to e^+e^-$ decay where the decay width (ignoring the spread in its mass from its full width) is given by [67]

$$\Gamma\left(\phi \to e^+e^-\right) = \frac{4\pi}{3}\alpha^2_{\mathrm{QED}}\frac{f^2_\phi}{m_\phi}e^2_h \tag{3.45}$$

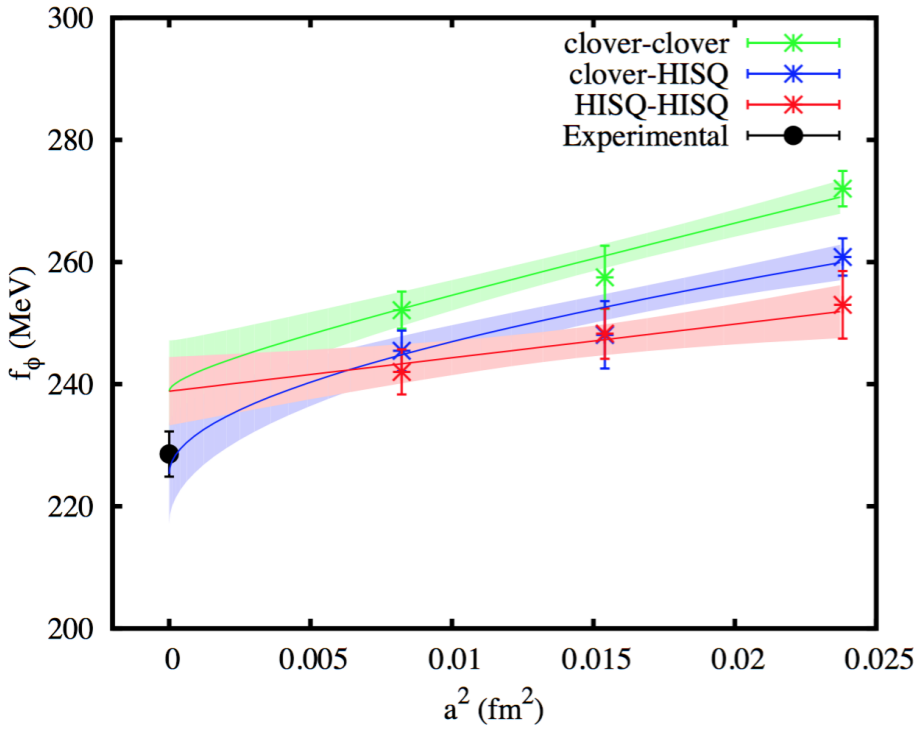

Figure 3.19: f_ϕ calculated with different quark formalisms and extrapolated to $a = 0$.

where $\alpha_{\text{QED}} \approx 1/137$; e_h = strange quark charge = $-1/3$ (in units of e); the experimental value of the average partial width $\Gamma(\phi \to e^+e^-) = 1.27 \pm 0.04$ keV and the experimental value of the mass of the $\phi = 1019.455 \pm 0.020$ MeV [68]. Therefore, the experimental value of f_ϕ is 228.56 ± 3.70 MeV.

m_ϕ and f_ϕ results computed on the $m_l/m_s = 0.2$ lattices are not accurate because the sea light quark mass we have been using is much heavier than the physical one. Therefore, in our calculation, the ϕ meson decays into virtual $K\bar{K}$ which are much heavier than the real kaons, giving rise to the difference between the lattice and the experimental results for the mass and decay constant of the ϕ meson.

To see how the masses of the dynamical light quarks impact our calculation, I have calculated the H-H ϕ correlators with physical dynamical light quarks. When extrapolated to the continuum using the same fit form as in equation 3.41, in this case m_ϕ and f_ϕ perfectly agree with the experimental results (shown in Figure 3.20).

3.6.6 Comparison of statistical uncertainties

Comparison of the statistical uncertainties coming from the H-H and the cl-cl methods has given the results as expected. The generation of one clover strange propagator costs ~ 4 times as much as that for one HISQ propagator combined with the fact that a clover propagator requires 16 times more storage compared to one HISQ propagator. However, the statistical uncertainties are similar in ϕ meson masses for the HISQ and the clover discretisations on the coarse and the fine lattices. This is shown in Figure 3.21) where the statistical uncertainties have been represented as the percent errors in the ϕ masses.

This is in line with the expectation from comparing the naive and the staggered quarks where the spin degrees of freedom for naive quarks is completely redundant.

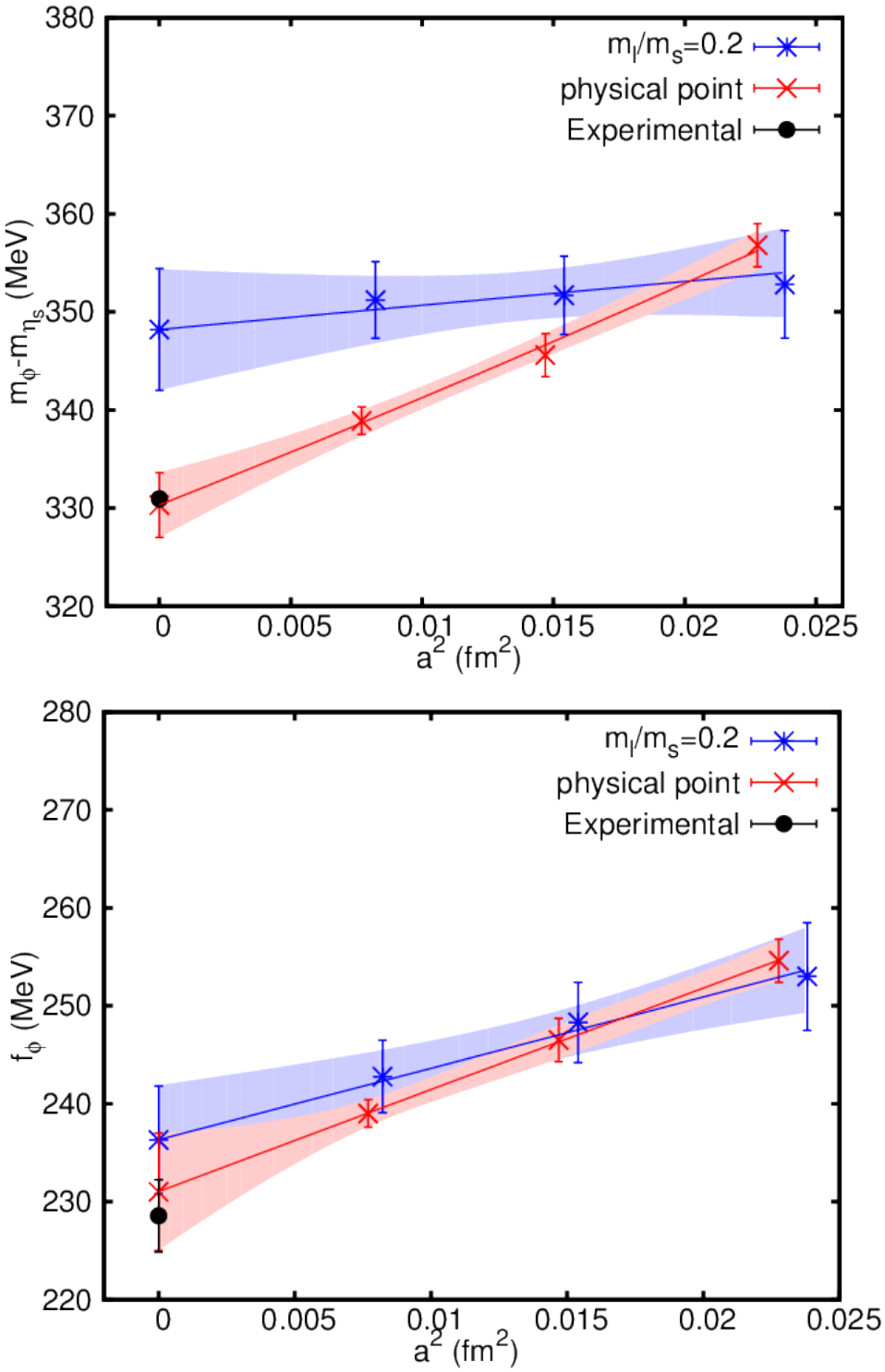

Figure 3.20: On the top: $m_\phi - m_{\eta_s}$ calculated with the H-H formalism and with two different masses of m_l^{sea} - physical and one-fifth m_s and extrapolated to $a = 0$. At the bottom: f_ϕ calculated with the H-H formalism and with two different masses of m_l^{sea} - physical and one-fifth m_s and extrapolated to $a = 0$

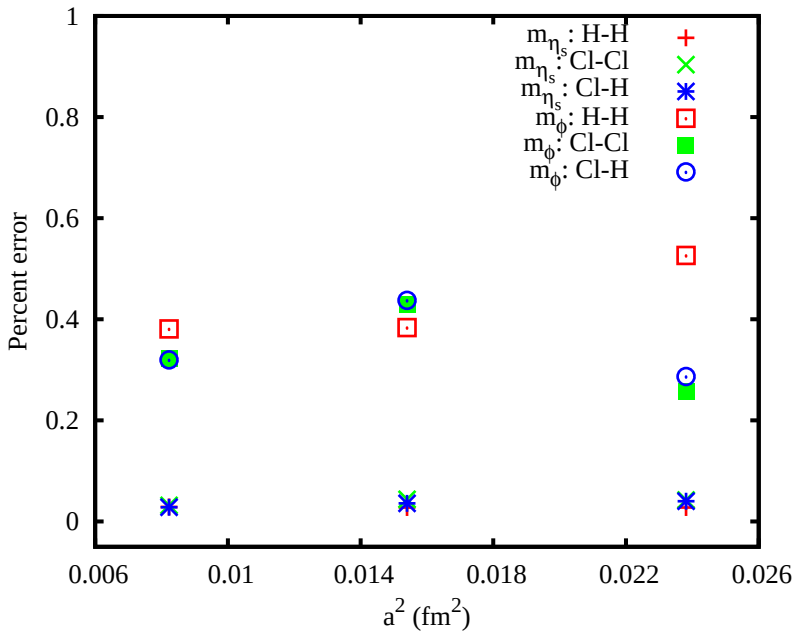

Figure 3.21: We compare the statistical uncertainties (in terms of percent errors) in m_{η_s} and m_ϕ using the H-H, cl-cl and H-cl formalism. We find that both the HISQ and clover formalisms achieve similar precision on the coarse and fine lattices if same number of configurations are used for calculation. We do not gain anything more in terms of the precision from using the four spin components of the clover quarks.

Part III

Muon g-2

Chapter 4

The anomalous magnetic moment of the muon and lattice QCD

4.1 Motivation

The anomalous magnetic moment of the muon, a_μ, defined as the fractional difference of its gyromagnetic ratio from the naive value of 2, i.e. $a_\mu = (g-2)/2$, is a result of the interactions of the muon with a cloud of virtual particles. It has been measured with an impressive accuracy of 0.54 parts-per-million (ppm) [69] in experiment (BNL $E821$): $11,659,208.9(54)(33) \times 10^{-10}$, thus providing the most stringent test of the Standard Model. Theoretically, a_μ has been calculated ($11,659,180.2(49) \times 10^{-10}$) with an even better precision of 0.42 ppm, but surprisingly, shows a tantalising discrepancy of about 3σ [70–73] with the experimental result. This could be an exciting indication of the existence of new virtual particles beyond the Standard Model. Improvements of a factor of 4 in the experimental uncertainty (Fermilab $E989$) are expected, and improvements in the theoretical determination would make the discrepancy (if it remains) really compelling.

In the SM, a_μ receives contributions from Quantum Electrodynamics (QED)

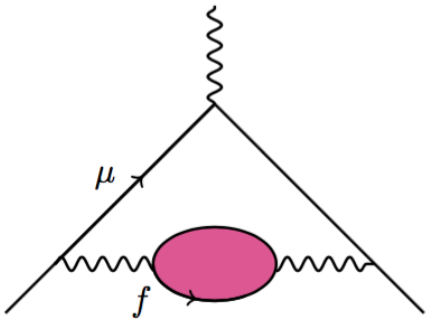

Figure 4.1: The hadronic vacuum polarisation contribution to the muon anomalous magnetic moment is represented as a coloured blob inserted into the photon propagator (represented by a wavy line) that corrects the point-like photon-muon coupling at the top of the diagram. This diagram is taken from [74].

for virtual leptons, from Electroweak (EW) theory for virtual gauge bosons and from Quantum Chromodynamics (QCD) for virtual hadrons. The QED contribution (largest) and the EW contribution (tiny) have been calculated with high precision and have little impact on the overall theoretical uncertainty in a_μ as listed in Table 4.1. The theoretical uncertainty is dominated by the QCD contributions, mainly by the lowest order hadronic vacuum polarisation (HVP) (0.36 ppm), $a_\mu^{\mathrm{HVP,LO}}$ (depicted in Figure 4.1). $a_\mu^{\mathrm{HVP,LO}}$ is currently determined most accurately from dispersion relations, using experimental input from the cross-section for e^+e^- to hadrons with an uncertainty of 0.7% [71,73] and this is the best accepted result for $a_\mu^{\mathrm{HVP,LO}}$. However, if $a_\mu^{\mathrm{HVP,LO}}$ can be calculated to better than 0.5% from first-principles lattice QCD calculations, we could improve on this result. The ETM Collaboration presented the first $N_f = 2+1+1$ lattice calculation for the connected HVP contribution to a_μ with an uncertainty of 4% including the systematics from their lattice fits [18].

With an aim in mind to achieve a 1% uncertainty in $a_\mu^{\mathrm{HVP,LO}}$, for this dissertation, we have developed a new lattice QCD method to calculate the HVP contribution to a_μ which is a significant improvement over previous methods used by other lattice collaborations.

Another hadronic contribution to a_μ whose determination can have significant

Table 4.1: This table shows the contributions to the overall theoretical uncertainty in a_μ coming from QED, EW and QCD. QCD contributions involve the hadronic vacuum polarisation (HVP) at the lowest order (LO), higher order (HO) HVP and the hadronic light-by-light contribution (HLBL).

Contribution	Result (x 10^{-10})	Error
QED (leptons) [70]	11658471.8	0.00 ppm
HVP(LO) [71, 73]	692.3	0.36 ppm
HVP(HO) [71, 75]	-9.8	0.01 ppm
HLbL [76]	10.5	0.22 ppm
EW [77]	15.4	0.02 ppm
Total SM	11659180.2	0.42 ppm

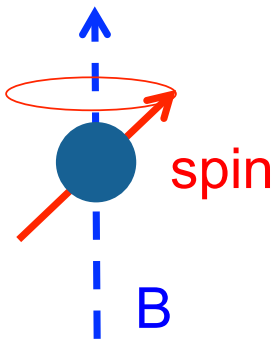

Figure 4.2: Lepton in an external magnetic field $\vec{B}$- its spin precesses around $\vec{B}$.

effect on the theoretical uncertainty in a_μ is from the hadronic-light-by-light diagrams [76, 78]. Detailed reviews on muon $g-2$ can be found in references [79, 80].

4.2 Definitions

An elementary fermion has an intrinsic magnetic moment $\vec{\mu}$ proportional to its spin $\vec{S}$ (depicted in Figure 4.2) and given by

$$\vec{\mu_l} = g_l \frac{Qe}{2m_l} \vec{s} \tag{4.1}$$

(in units of $\hbar = c = 1$) where e is the fundamental electric charge, and m_l is the fermions mass.

In free Dirac theory the Landé g-factor is exactly 2, representing the tree level

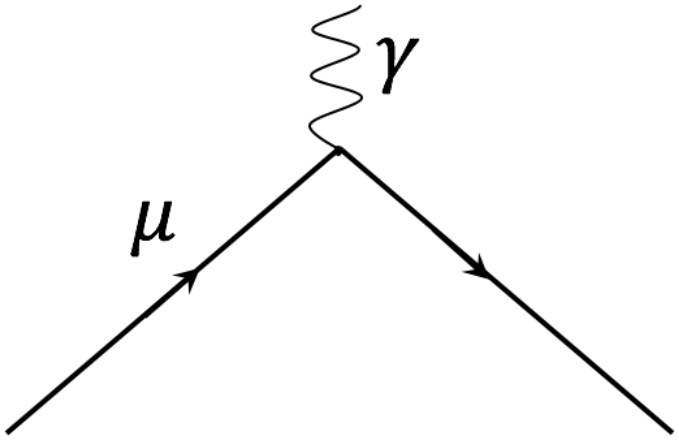

Figure 4.3: Tree level fermion-photon interaction vertex.

vertex of fermion's electromagnetic interaction (shown in figure 4.3).

In the presence of interactions, the vertex gets radiative corrections (indicative diagrams in Figure 4.4 [80]) which can be calculated order-by-order in $\alpha \equiv \frac{e^2}{4\pi}$ from weak-coupling perturbation theory for the QED contributions. Additionally the hadronic contributions can be calculated using a semiphenomenological or a non-perturbative approach, discussed later in this chapter.

The fundamental electromagnetic interaction of the fermions can be represented by a matrix element of the electromagnetic current between incoming and outgoing fermion states represented by $|p_1, s_1\rangle$ and $|p_2, s_2\rangle$ respectively. Here, p is the momentum index and s denotes the spin. The matrix elements due to Lorentz invariance and the Ward-Takahashi identity, take the following form

$$\langle p_2, s_2|\bar{\psi}\gamma_\mu\psi|p_1, s_1\rangle = \bar{u}(p_2, s_2)\big(\gamma_\mu F_1(q^2) + \frac{i\sigma^{\mu\nu}}{2m}q_\nu F_2(q^2)\big) \tag{4.2}$$

where $u(p_1, s_1)$ and $\bar{u}(p_2, s_2)$ are the spinors, $q_\nu = (p_1 - p_2)_\nu$ is the space-like momentum transferred by the photon to the fermion, and the two form factors $F_1(q^2)$ and $F_2(q^2)$ retain all the information about the interaction [80]. In the limit $q^2 \to 0$, F_1 gives the fundamental electric charge e and F_2 is defined as:

$$F_2(0) = \frac{g-2}{2} \tag{4.3}$$

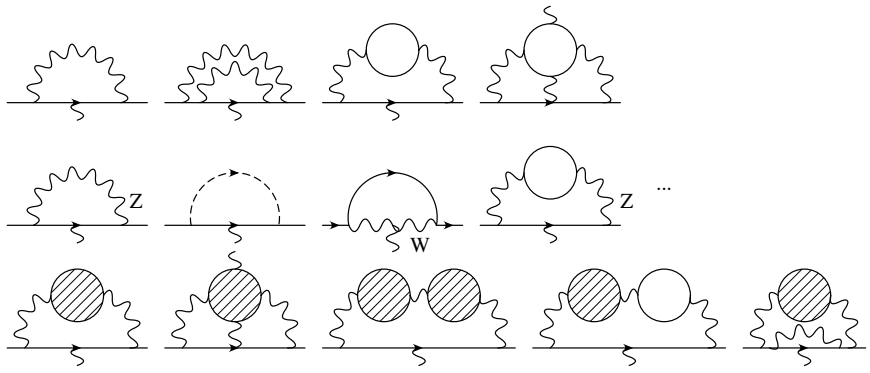

Figure 4.4: Representative diagrams for QED, EW, hadronic corrections to fermion-photon naive interaction vertex (diagram taken from reference [80]). The upper level diagrams are due to QED corrections with the left most one known as the Schwinger term. The diagrams in the mid-level get corrections due to electroweak interactions of muon, and the diagrams at the bottom arise from the hadronic corrections.

or the "anomalous magnetic moment" of the fermion.

4.3 Experimental Status

The pioneering experiments to measure muon $g-2$ started at CERN [81] over five decades ago and the last of the sets was carried out three decades ago resulting in a 7 ppm mean experimental uncertainty in a_μ. These experiments were followed by $E821$ at BNL between 2001-2004, which reduced the uncertainty to 0.54 ppm [69].

$$a_\mu^{\text{exp}} = 11659208.9(63) \times 10^{-10}. \tag{4.4}$$

$E821$ used high intensity primary proton beams whose collision with a fixed target generates decay pions which are unstable and decay into muons and neutrinos. The longitudinally polarised high energy forward decay muons are then fed into a storage ring with a constant magnetic field ($\vec{B}$). While circulating with almost the speed of light the muons continually decay to positrons and neutrinos.

$$\mu^+ \to e^+ + \nu_e + \bar{\nu_\mu}. \tag{4.5}$$

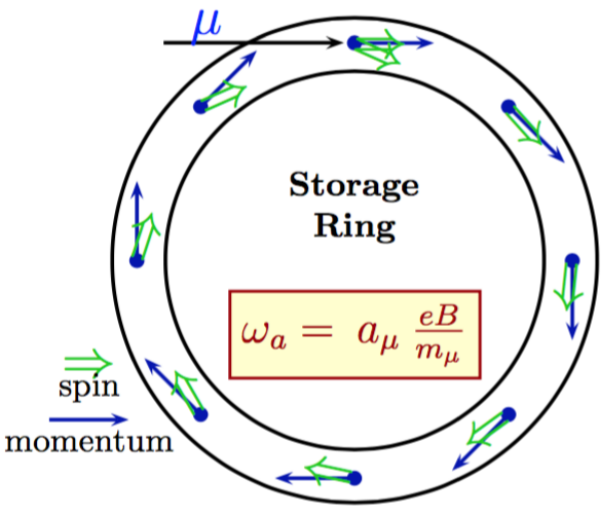

Figure 4.5: Indicative diagrams to show the muon's spin and "Larmor precession" within the storage ring. This diagram is taken from reference [79].

While the neutrinos fly away undetected, the positrons are detected by detectors distributed around the storage ring. While circulating around the storage ring, the muon's spin vector precesses around $\vec{B}$, and the phenomenon, known as "Larmor precession", is characterised by an angular frequency $\vec{\omega_a}$. In the horizontal plane, the muons execute a relativistic cyclotron motion and the cyclotron frequency is given by $\vec{\omega_c}$ (represented in Figure 4.6). Due to the presence of the muon's anomalous magnetic moment a_μ, the spin precession frequency $\vec{\omega_s}$ is slightly larger than $\vec{\omega_c}$ and the difference is defined as $\vec{\omega_a}$,

$$\omega_c = \frac{eB}{m_\mu \gamma} \tag{4.6}$$

$$\omega_s = \frac{eB}{m_\mu} big(\frac{1}{\gamma} + a_\mu\big) \tag{4.7}$$

$$\omega_a = \omega_s - \omega_c = a_\mu \frac{eB}{m_\mu} \tag{4.8}$$

where γ is the relativistic Lorentz factor corresponding to the orbital speed of the muons in the ring, v.

Now, to retain the muons in the ring, an additional electric field $\vec{E}$ is also applied in perpendicular to the plane of muon orbit using an electrostatic focusing system.

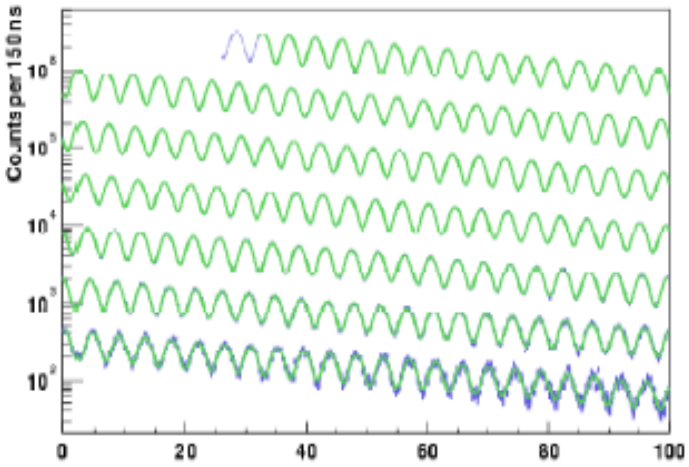

Figure 4.6: This figure shows the sinusoidal modulation in the time distribution of the decay positrons in the storage ring. This diagram is taken from [79].

It has been shown [79, 82] that this modifies equation 4.8 as follows.

$$\omega_a = \frac{e}{m_\mu}\left(a_\mu \vec{B} - [a_\mu - \frac{1}{\gamma^2 - 1}]\vec{v} \times \vec{E}\right) \tag{4.9}$$

By choosing a "magic" momentum for muons, 3.094 GeV/c (c is the speed of light in the vacuum), the effect of $\vec{E}$ vanishes from equation 4.9 and we get back equation 4.8. Therefore, for precise measurement of a_μ from experiment one has to measure a frequency $\vec{\omega_a}$, and a magnetic field ($\vec{B}$) precisely from this experiment. The muon mass m_μ is measured from another experiment on muonium.

The angular frequency $\vec{\omega_a}$ is accurately determined from the sinusoidal modulation in the time distribution of the decay positrons (shown in Figure 4.6) observed with electromagnetic calorimeters [69,83,84]. More details about the experiment $E821$ can be found in references [69, 79, 83–85].

The forthcoming muon g-2 experiment at Fermilab ($E989$) [86,87] and at J-PARC ($E34$) [88] expect to reduce the uncertainty in a_μ to 0.14 ppm starting in 2017/18. $E989$ uses the same electromagnet from the BNL experiment and the same principle with a magic momentum, but with muons of much higher intensity. The J-PARC experiment does not require the electrostatic lensing or the magic momentum concept

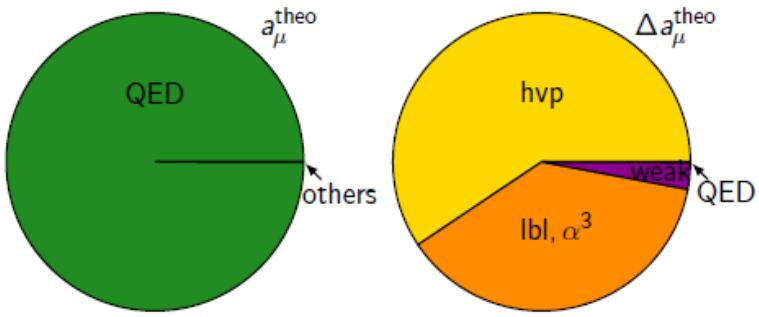

Figure 4.7: The left diagram shows the pie-chart for different contributions and the diagram on the right indicates the uncertainties in calculating these contributions. We can clearly see that the dominant contribution to a_μ comes from QED whereas the theoretical uncertainty gets its dominant contribution from the hadronic vacuum polarisation. This diagram is taken from reference [89].

as an ultra-cold muon beam is utilised [88].

4.4 Theoretical status

From Table 4.1 we can see that the dominant contribution to a_μ comes from QED whereas the theoretical uncertainty gets dominant contribution from the hadronic vacuum polarisation. This is depicted in Figure 4.7) (taken from reference [89]).

4.4.1 QED contribution

The QED contributions can be calculated order-by-order in $(\frac{\alpha}{\pi})$ from perturbation theory since the coupling α, the fine structure constant, is much less than 1 [79,89,90]:

$$\alpha = 7.2973525698(24) \times 10^{-3} \tag{4.10}$$

and

$$a_\mu^{\text{QED}} = \sum_{n=1}^{\infty} a_\mu^n \left(\frac{\alpha}{\pi}\right)^n. \tag{4.11}$$

The leading order QED contribution (depicted in Figure 4.8) known as the Schwinger term [91] has the dominant contribution in a_μ. The QED diagrams have been

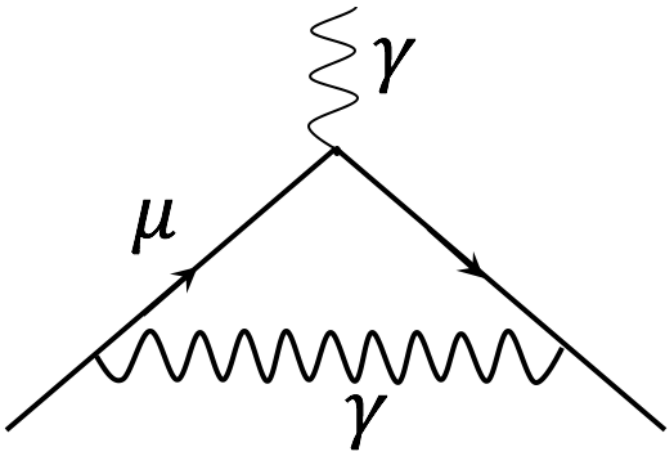

Figure 4.8: Leading order QED contribution (Schwinger term) [91]

calculated up to the fifth order in α [92] and the calculated result is

$$a_\mu^{\text{QED}} = 11658471.8846(37) \times 10^{-10}. \tag{4.12}$$

The uncertainty achieved in this calculation is ~ 0.3 parts-per-billion (ppb). The leading contribution to a_μ at the sixth order has been estimated [92] to

$$a_\mu^{\text{QED}}[\text{6-loop}] \sim 0.8 \times 10^{-12} \tag{4.13}$$

which is twice the size of the uncertainty in a_μ^{QED} up to the fifth order.

4.4.2 EW Contribution

The electroweak contributions, though very small (from Table 4.1), still need to be calculated unambiguously as they are altogether of size 3σ and without counting it the deviation of the theory from the experiment would have been 6σ. It was possible to make convincing predictions of a_μ^{EW} after the Electroweak Standard Model had been renormalised by 't Hooft in 1971 [79]. But a_μ being a physical quantity can also be directly calculated in unitary gauge which is particularly easy as only the physical particles appear in the diagrams and the diagrams exhibiting Higgs ghosts and Faddeev-Popov ghosts are absent. Since the gauge bosons $W^\pm, Z$ and Higgs (H)

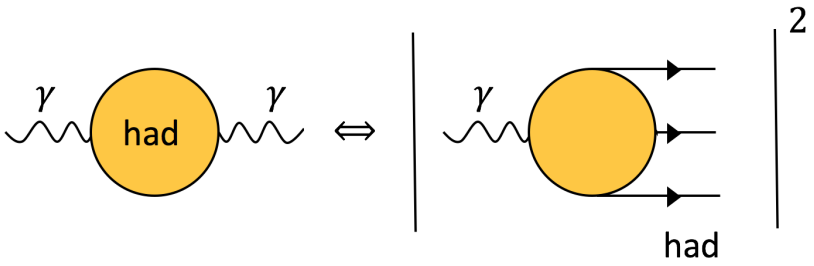

Figure 4.9: Visualisation of optical theorem

are much more massive than the relevant energy scale of a_μ, a perturbative treatment of the electroweak contribution is possible [79, 89].

Neglecting the tiny terms $O(m_\mu^2/M_{W,Z}^2)$, and combining the W and Z boson contributions, the results for $a_\mu^{\rm EW}$ in one loop and two loops are [79, 89, 90]

$$a_\mu^{\rm EW}[\text{1-loop}] = 19.482(2) \times 10^{-10} \tag{4.14}$$

$$a_\mu^{\rm EW}[\text{2-loop}] = -4.07(21) \times 10^{-10}. \tag{4.15}$$

The contribution due to the Higgs mass is $\sim 10^{-14}$ [79, 89] and the leading logarithms for the three-loop contribution $\sim 10^{-12}$ [90] are, therefore, not included at the current level of precision.

4.4.3 Hadronic Contributions

The hadronic contributions enter a_μ at the order $(\frac{\alpha}{\pi})^2$ known as the lowest order "hadronic vacuum polarisation (HVP)", $a_\mu^{\rm HVP,LO}$ (represented by Figure 4.1).

At low energy this contribution is not calculable in perturbation theory. To date $a_\mu^{\rm HVP,LO}$ is best known from a semi-phenomenological approach using the optical theorem and dispersion relation with the $e^+e^- \to$ hadrons experimental cross sections.

In this method,

$$a_\mu^{\rm HVP,LO} = \alpha_s^2 \int_{4m_\pi^2}^{\infty} ds K(s/m^2)\sigma_{\rm tot}(s) \tag{4.16}$$

where s is the center-of-mass energy and $\sigma_{\rm tot}(s)$ is the total cross section of $e^+e^- \to$ hadrons. The integration kernel is given by [79]

$$\begin{aligned} K(s) &= \frac{3s}{m_\mu^2}\Big(\frac{s^2}{2-s^2} + \frac{(1+s^2)(1+s^2)}{s^2}\big(\ln(1+s) - s + \frac{s^2}{2}\big) \\ &+ \frac{(1+s)}{(1-s)}s^2\ln(s)\Big). \end{aligned} \tag{4.17}$$

Here, the major sources of uncertainties come from the experimental inputs and the numerical integration. Above the cutoff $m_{\rm cut} \geq 2$ GeV, perturbation theory is used to calculate this integral. Hagiwara et. al. [71] calculated the value to be

$$a_\mu^{\rm HVP,LO} = 694.9(4.3) \times 10^{-10}. \tag{4.18}$$

There is a spread between different semi-phenomenological approaches using different experimental data, which is expected to be resolved with the new data coming from BES-III. Since the dominant contribution to the theoretical uncertainty in a_μ arises from the theoretical calculation of $a_\mu^{\rm HVP,LO}$, for this dissertation I have concentrated on the first principle theoretical calculation of $a_\mu^{\rm HVP,LO}$ using lattice QCD.

The higher order diagrams, for example, diagrams at $(\frac{\alpha}{\pi})^3$ including higher order hadronic vacuum polarisation can be calculated using the same technique [79].

$$a_\mu^{\rm HVP}[\alpha^3] = -8.85(9) \times 10^{-10}. \tag{4.19}$$

4.5 HVP from lattice QCD: our formalism

On the lattice, $a_\mu^{\rm HVP,LO}$ associated with a given quark flavour, f, is obtained by inserting the quark vacuum polarisation $\hat{\Pi}$ into the photon propagator [93,94] (shown in Figures 4.1 and 4.10).

$$a_{\mu,\rm HVP}^{\rm (f)} = \frac{\alpha}{\pi}\int_0^\infty dq^2 f(q^2)(4\pi\alpha Q_{\rm f}^2)\hat{\Pi}_{\rm f}(q^2) \tag{4.20}$$

where $\alpha \equiv \alpha_{\rm QED}$ and Q_f is the electric charge of the quark flavour f in units of

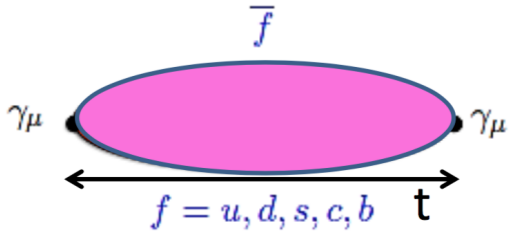

Figure 4.10: Representative HVP contribution to the muon anomalous magnetic moment is given as a shaded blob inserted into the photon propagators represented by a wavy line.

e. We have not considered the disconnected diagrams at this point so the result is flavour-diagonal. Here, we need the renormalised vacuum polarisation function,

$$\hat{\Pi}(q^2) \equiv \Pi(q^2) - \Pi(0) \tag{4.21}$$

and $f(q^2)$ is a known analytic function of four-momentum squared, given by

$$f(q^2) \equiv \frac{m_\mu^2 q^2 A^3 (1 - q^2 A)}{1 + m_\mu^2 q^2 A^2} \tag{4.22}$$

where

$$A \equiv \frac{\sqrt{q^4 + 4m_\mu^2 q^2} - q^2}{2m_\mu^2 q^2}. \tag{4.23}$$

$f(q^2)$ is strongly peaked around $q^2 \sim m_\mu^2/4 \sim 0.003$ GeV^2 and so is the integrand in equation 4.20. However, extrapolating from higher values of q^2 to near zero values of q^2 leads to model uncertainties.

To get around this issue we have developed a new method [95] in which the HVP contribution is expressed as a Taylor series of a small number of derivatives of the vacuum polarisation function $\hat{\Pi}$ evaluated at $q^2 = 0$.

The quark polarisation tensor is the Fourier transform of the vector current-current correlator. For spatial currents at zero spatial momentum

$$\Pi^{ii}(q^2) = q^2 \Pi(q^2) = a^4 \sum_t e^{iqt} \sum_{\vec{x}} \langle j^i(\vec{x}, t) j^i(0) \rangle \tag{4.24}$$

with q the Euclidean energy. Time-moments of the correlator give the derivatives at

$q^2 = 0$ of $\hat{\Pi}$ [8]:

$$\begin{aligned} G_{2n} &\equiv a^4 \sum_t \sum_{\vec{x}} t^{2n} Z_V^2 \langle j^i(\vec{x}, t) j^i(0) \rangle \\ &= (-1)^n \left. \frac{\partial^{2n}}{\partial q^{2n}} q^2 \hat{\Pi}(q^2) \right|_{q^2=0} . \end{aligned} \tag{4.25}$$

Here we need a renormalisation factor Z_V for the lattice vector current which is not conserved in our HISQ simulation. Note that time-moments remove any contact terms between the two currents. G_{2n} is easily calculated from the correlators calculated in lattice QCD, remembering that time runs from 0 at the origin in both positive and negative directions to a maximum value of $T/2$ in the centre of the lattice.

Defining

$$\hat{\Pi}(q^2) = \sum_{j=1}^{\infty} q^{2j} \Pi_j \tag{4.26}$$

then

$$\Pi_j = (-1)^{j+1} \frac{G_{2j+2}}{(2j+2)!} . \tag{4.27}$$

Using Padé approximants [96] [1] instead of Taylor approximation allows us to deal with high momenta. To evaluate the contribution to a_μ we replace $\hat{\Pi}(q^2)$ with its $[2,2]$ Padé approximants derived from the Π_j [95]. We perform the q^2 integral numerically. The Padé approximation and numerical integration have been performed by codes written by G. Peter Lepage for our (HPQCD) collaboration.

4.6 Lattice simulation

We calculate the light (u/d) and strange (s) quark propagators using the HISQ [97] discretisation on HISQ gauge configurations (given in table 4.2 and shown in figure 2.1) generated by the MILC collaboration [98, 99] with dynamical light (up/down), strange and charm quarks ($N_f = 2 + 1 + 1$). We have used three lattice ensembles

[1] The $[m, n]$ Padé approximant of a function $f(x)$ is a ratio of polynomials in x, of order m in the numerator and n in the denominator, whose Taylor expansion is the same as that of $f(x)$ through order x^{n+m}.

with lattice spacings a $\approx 0.15\,\text{fm}$ (very coarse), $0.12\,\text{fm}$ (coarse) and $0.09\,\text{fm}$ (fine), determined [27] using the Wilson flow parameter w_0 [24]. At each lattice spacing we have three values of the average u/d quark mass (m_l): one fifth and one tenth the s quark mass (m_s) and the physical value ($m_s/27.5$). We tune the valence s quark mass accurately [59] using the mass of the η_s meson ($688.5(2.2)\,\text{MeV}$) [27], as discussed in Chapter 3. At $m_l = m_s/10$, at one lattice spacing $\sim 0.12\,\text{fm}$, we have three different volumes to test for finite volume effects. These sets correspond to a lattice length in units of the π meson mass of $M_\pi L = 3.2$, 4.3 and 5.4. In addition we de-tuned the valence s quark mass by 5% (set 6) to test for tuning effects.

I first tested our method with the calculation of the s quark connected HVP contribution to a_μ and for this the s quark propagators are combined into a correlator with a local vector current at either end which is dominated by the vector meson ϕ at large time. We use the random colour wall source created from a set of $U(1)$ random numbers over a timeslice for improved statistics. The source and the sink ends are summed over the spatial sites on a timeslice by the use of the random wall and set the spatial momentum to zero. I have found the local vector current renormalisation constant ($Z_{V,\bar{s}s}$) completely non-perturbatively with 0.1% uncertainty on the finest $m_l = m_s/5$ lattices [59] (details in chapter 3).

Similarly, to obtain the light quark connected contribution to HVP, I have combined the light quark propagators using a local vector current to form the local light vector connected correlators (dominated by vector meson ρ). The same renormalisation constants, calculated for strange correlators as in reference [59], have been used to renormalise the light vector correlators . We ignore the mass dependence of the Z_Vs since it is less than 0.1% - $\mathcal{O}([am_s/\pi]^2\alpha_s)$ and therefore negligible compared to our statistical errors. The charm quark contribution (connected) to $a_\mu^{\text{HVP,LO}}$ has also been calculated from the previously obtained moments [100] and the bottom quark contribution is calculated using NRQCD in [101] using the same formalism. The HVP

Table 4.2: Here we use gluon field congurations from the MILC collaboration [22]. $\beta = 10/g^2$ is the QCD gauge coupling, and w_0/a for Wilson flow parameter $w_0 = 0.1715(9)$ fm fixed from f_π [25] gives the lattice spacing, a. The masses of the sea quarks- am_l for light quarks, am_s for strange quarks and am_c for charm quarks along with tuned valence s quark mass am_s^{tuned} are given. L/a and T/a are the spatial and temporal lengths of the lattice, and $N_{\text{cfg},s}$ and $N_{\text{cfg},l}$ are the numbers of gauge configurations used on each ensemble for the calculation of a_μ^s and a_μ^l respectively [74].

Set	β	w_0/a	am_l	am_s	am_c	am_s^{tuned}	$L/a \times T/a$	$N_{\text{cfg},s}$	$N_{\text{cfg},l}$
1	5.8	1.1119(10)	0.013	0.065	0.838	0.0700(9)	16×48	1020	9947
2	5.8	1.1272(7)	0.0064	0.064	0.828	0.0686(8)	24×48	1000	1000
3	5.8	1.1367(5)	0.00235	0.0647	0.831	0.0677(8)	32×48	526	997
4	6.0	1.3826(11)	0.0102	0.0509	0.635	0.0545(7)	24×64	1019	1053
5	6.0	1.4029(9)	0.00507	0.0507	0.628	0.0533(7)	24×64	988	1020
6	6.0	1.4029(9)	0.00507	0.0507	0.628	0.0533(7)	32×64	300	1000
7	6.0	1.4029(9)	0.00507	0.0507	0.628	0.0534(7)	40×64	313	331
8	6.0	1.4149(6)	0.00184	0.0507	0.628	0.0527(6)	48×64	1000	998
9	6.3	1.9006(20)	0.0074	0.037	0.44	0.0378(5)	32×96	504	1000
10	6.3	1.9330(20)	0.00363	0.0363	0.43	0.0366(5)	48×96	621	298

also gets contribution from the disconnected correlators, though expected to be very small. I will cover this topic later in this chapter.

We should note that these are the same vector meson correlators which are mainly used to extract meson properties such as masses and decay constants. In Chapter 3 we have shown how accurate our strange vector meson correlators are by extracting the most accurate ϕ meson properties to date. Similar checks are performed for the light vector correlators by extracting the properties of the ρ meson from the two-point light correlators.

4.7 Handling light vector correlators [74]

The light quark contribution in $a_\mu^{\mathrm{HVP,LO}}$ is the most significant part, being 12 times larger than that for the strange quark, in part because of a factor of 5 from the electric charges. Though the extension of our method [95] to calculate $a_{\mu,\mathrm{HVP}}^{\mathrm{light}}$ is straightforward, poor signal-to-noise ratio in this case significantly increases the statistical uncertainties in the time moments [95]. The signal in this case is controlled by the light quark vector meson pole ρ and the noise by the pseudoscalar meson π. The signal to noise ratio for the vector correlators degrades exponentially with increasing time slices. This increases the uncertainties in the Taylor coefficients Π_j, particularly for higher j values.

We have overcome this issue by calculating the time moments from the reconstructed correlators using the best fit parameters for time slices larger than t^* instead of using the original correlators. This constrains the uncertainties in the correlators at larger times without underestimating them, therefore giving a much better precision in the time moments. I have used the data-fit hybrid correlator as follows:

$$G(t) = \begin{cases} G_{\mathrm{data}}(t) & \text{for } t \leq t^* \text{ from Monte Carlo,} \\ G_{\mathrm{fit}}(t) & \text{for } t > t^* \text{ from multi-exponential fit.} \end{cases}$$

for $t^* = 1.5$ fm $= 6/m_\rho$. I have tested different values of t^* starting from $t^* =$ tmin to pick up a t^* such that we get $\sim 70\%$ of the result from $G_{\rm data}$. We get the same results to within $\pm\sigma/4$ with $t^* = 0.75$ fm.

4.7.1 Gaussian smearings

Furthermore, we have improved the fit uncertainties by using Gaussian smearings [102–105] at both the source and the sink and fitting a 2×2 matrix of correlators using simultaneous Bayesian fitting. The smearing is chosen to have an improved projection onto the ground state vector meson ρ and thus reduces the excited state contamination in the smaller time slices. This gives us a larger plateau for extraction of the meson mass and ground state amplitudes (as depicted in Figure 4.11).

A 2×2 matrix of vector meson correlators is formed from all four combinations of two meson operators with zero three momentum for the source and sink. One meson operator is the local vector current operator denoted by "loc" and another is a vector current operator with Gaussian covariant smearing applied to the quark field using operator

$$1 + \left[\frac{r_0^2 D^2}{4n}\right]^n \overset{n\to\infty}{\to} \exp\left(\frac{r_0^2.D^2}{4n}\right). \tag{4.28}$$

Here, D^2 is the covariant Laplacian operator, r_0 is the parameter for the width of the Gaussian function or the smearing radius and n is the number of iterations to achieve the smearing. The smearing operator iteratively constructs a Gaussian function and an extended source. Since we are using staggered quarks and require the current-current correlator for a specific staggered taste, we use a stride-2 covariant operator i.e. the difference operator is defined for grid spacing twice the lattice spacing a instead of only a.

The parameters r_0 and n have been chosen to get the fastest overlap with the ρ

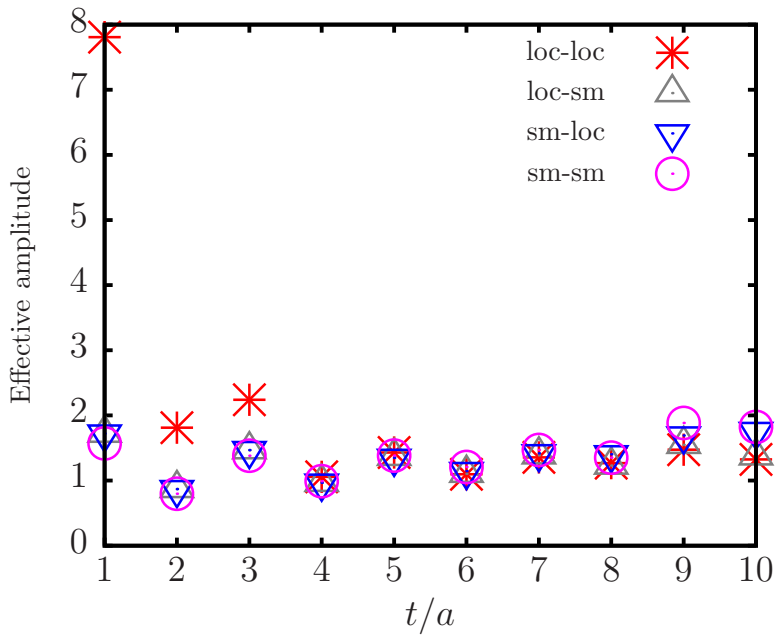

Figure 4.11: In this plot the ratio of the vector correlator to its ground state i.e. the effective amplitude for the first few time slices is shown for all four source and sink smearing combinations. We can clearly see that the plateau (around 1) is achieved much faster for the smeared correlators compared to the non-smeared (loc-loc) correlator (in red points). This plot corresponds to the coarse lattice with physical m_l.

Table 4.3: This table summarises the best values of the smearing parameters used in my calculation for each lattice spacing - the smearing radius r_0 and the number of iterations n for each r_0.

Set	$\sim a$ (fm)	r_0	n
Very coarse	0.15	3a	20
Coarse	0.12	3.75a	30
Fine	0.09	4.5a	40

ground state $\sim e^{-mt} + e^{-m(T-t)}$, where m is the ρ mass and T is the temporal length of the lattice. For the best choice of r_0, only the ground state will be present in principle, and the effective mass

$$M_{\text{eff}}(t) = \frac{1}{N} \frac{C(t)}{e^{-mt} + e^{-m(T-t)}} \tag{4.29}$$

will converge to 1 within 2 to 4 timeslices on the lattice. The number of iterations n is chosen for each r_0 to approximate the Gaussian smoothly. For insufficient iterations the behaviour of $M_{\text{eff}}(t)$ is different when compared to more iterations when the shape remains similar with the increase of n. In practice, I only optimised smearing on one lattice spacing and scaled the rest.

Table 4.3 summarises the best values of the smearing parameters used in my calculation.

Using smearings I have achieved a $\sim$ 25-30% gain in precision in a_μ^{light} for $\sim$ 20-25% increase in the computation cost.

4.7.2 Data analysis and fits

The fit form for the light vector meson correlators is similar to equation 2.46 as discussed in Chapter 3 and given by:

$$\begin{aligned} G_{ij}(t) = a^3 \sum_{k=0}^{n_{\text{exp}}} b_i^{(k)} b_j^{(k)} (e^{-E^{(k)}t} + e^{-E^{(k)}(T-t)}) \\ -(-1)^t a^3 \sum_{ko=0}^{n_{\text{exp}}} d_i^{ko} d_j^{ko} (e^{-E_o^{ko}t} + e^{-E_o^{ko}(T-t)}). \end{aligned} \tag{4.30}$$

The indices i and j stand for meson source and sink respectively. The analysis of the strange meson correlators has been discussed in Chapter 4. In equation 4.30, the first sum is over $J^{PC} = 1^{--}$ vector states coupling to vector operators. The second sum is over the opposite parity states arising from the staggered quark oscillations. $n_{\rm exp}$ represents how many excited states are considered in the fitting and it is normally 7 in my fits, though the fit stabilizes after 3-4 exponentials. I have used the Bayesian fitting technique [65] and set wide priors (in units of GeV) as follows: For first sum,

$$\begin{aligned}
\log(E^{(0)}) &= \log(0.75(38)) \\
\log(E^{(k)} - E^{(k-1)}) &= \log(1.0(5)) \quad (k > 0) \\
\log(b^{(0)}_{\rm loc}) &= \begin{cases} \log(0.14(14)) & (k = 0), \\ \log(0.42(42)) & (k > 0) \end{cases} \\
b^{(0)}_{sm}, b^{(k)}_{sm} &= 0.01(1).
\end{aligned} \tag{4.31}$$

using the same notations as in previous chapter. We have assigned analogous priors for the second sum as well, but with

$$\log(E^{(0)}_o) = \log(1.2(6)). \tag{4.32}$$

With these priors I have achieved an excellent fit with χ^2 per degree of freedom standing between 0.5-0.9. In terms of 'loc' and 'sm' indices the definition of our $G_{\rm fit}(t)$ used in equation 4.28 gives

$$G_{\rm fit}(t) \equiv G_{\rm loc,loc}\,|_{t\to\infty} \tag{4.33}$$

$$= a^3 \sum_{k=0}^{n_{\rm exp}} b^{(k)}_{\rm loc} b^{(k)}_{\rm loc} e^{-E^{(k)}t} - (-1)^t a^3 \sum_{ko=0}^{n_{\rm exp}} d^{ko}_{\rm loc} d^{ko}_{\rm loc} e^{-E^{ko}_o t}. \tag{4.34}$$

$G_{\rm fit}(t)$ has been reconstructed using the best fit parameter.

From these two-point correlator fits I have extracted the mass M_ρ and ground state amplitude a_0 for the ρ meson. The decay constant for ρ is extracted from

$$f_\rho = a_0 Z_{V^4} \sqrt{\frac{2}{M_\rho}}. \tag{4.35}$$

Our results for these are listed in Table 4.6 and shown in Figure 4.17 with comparison to previous lattice values.

4.7.3 Additional systematic uncertainties

The ρ is not a gold-plated particle and decays to two pions in the continuum, which doesn't happen properly on our lattices with heavier than physical light quark masses. Since, 80% of the light quark vacuum polarisation contribution comes from the ρ meson pole, much of the light quark mass dependence comes from that of the ρ. In handling the light quark vector current-current correlators we found that m_ρ and f_ρ (Figure 4.17) show small finite spatial volume and finite lattice spacing effects on these lattices. Therefore we need to understand ρ better on the lattice and correct for the finite volume effects. We can remove these effects by rescaling the coefficients with the appropriate powers of the ρ mass [18]. Additional systematic uncertainties come from the fact that we are using staggered quarks which give rise to additional tastes of the pions other than the Goldstone one and there exists mass splittings between these tastes on the lattice.

An important contribution to be handled is that from the photon coupling to $\pi - \pi$. It is the $\pi - \pi$ contribution that that has potentially large finite volume contributions and those can be corrected for relatively simply. This is a scalar QED calculation in which $\pi^+\pi^-$ couple to a photon. The issue there is that the finite volume effects are suppressed in our calculation by the staggered effects which mean that other tastes of pion are heavier than the Goldstone, so we will really need to go to finer lattices to see them. To remove this effect on our lattices, we first remove this $\pi\pi$ contribution on each lattice using one-loop, staggered quark, finite-volume chiral perturbation theory [74, 106]. And then restore it from one-loop continuum chiral

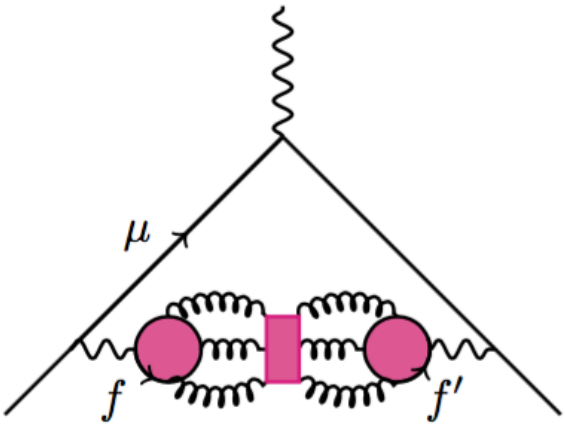

Figure 4.12: This figure is a representative diagram of the disconnected contribution to $a_\mu^{\mathrm{HVP,LO}}$. Here the two coloured blobs are made of light-light, strange-strange and light-strange currents and interact with each other via exchange of gluons.

perturbation theory, with physical π mass. The scaling of $\hat{\Pi}_j^{\mathrm{latt}}$ in this way gives

$$\hat{\Pi}_j^{\mathrm{latt}} \to (\hat{\Pi}_j^{\mathrm{latt}} - \hat{\Pi}_j^{\mathrm{latt}}(\pi\pi)) \left[\frac{m_\rho^{2j,\mathrm{latt}}}{m_\rho^{2j,\mathrm{expt}}} \right]_{\mathrm{latt}} + \hat{\Pi}_j^{\mathrm{cont}}(\pi\pi) \tag{4.36}$$

where $\hat{\Pi}_j^{\mathrm{cont}}(\pi\pi) = 70 \times 10^{-10}$.

The finite volume correction has been mainly done by G. Peter Lepage and is detailed in reference [74].

4.8 Disconnected correlators

The quark-line disconnected contribution to the HVP (depicted in Figure 4.14) is suppressed by m_q. Since

$$\sum_{f=u,d,s} Q_f = 0, \tag{4.37}$$

for Q_f being the charge of quark flavour f, the disconnected contribution to $a_\mu^{\mathrm{HVP,LO}}$ vanishes if $m_u = m_d = m_s$ [94], therefore, it is expected to be very small in reality. In chiral perturbation theory the only terms that contribute are the $\pi - \pi$ ones and this gives a factor of 1/10 between the connected and the disconnected pieces (as we showed in [107].

On the lattice we calculate the disconnected correlators of the following form (4.14):

$$G_{\text{disc}}(x_0 - y_0) \;=\; -Z_V \langle \left(\sum_{\vec{x}} \text{Tr}[\gamma_k D^{-1}(x,x)] \right) \left(\sum_{\vec{y}} \text{Tr}[\gamma_k D^{-1}(y,y)] \right) \rangle$$

The disconnected correlators are extremely noisy and historically other lattice groups (for example [108]) found it challenging to achieve a signal or a small uncertainty. Therefore, our target is to calculate a conservative upper bound for a systematic error from neglecting the disconnected contribution.

I have first applied the "all-to-all" propagator method [108] to calculate the disconnected light and strange correlators (assuming the charm and bottom quarks have negligible disconnected contributions). I have used 50 stochastic noise vectors on each configuration with one-link taste-singlet spatial vector currents for (light - strange) or $(l - s)$ on both sides. It is appropriate to use $(l - s)$ currents as we can see from equations 4.39 and 4.40.

Using the same noise for l and s currents (the method suggested in [108]) I have found a 40% reduction in the uncertainty compared to the l quark case alone (seen from Figure 4.13), though no signal was obtained which is consistent with [108]. One can use spectral decomposition of the propagator with diluted noisy estimators [109] or the method of distillation [110] for obtaining a good signal for the disconnected correlators. But these methods are too expensive with our configurations and beyond the scope of my dissertation.

To get an estimation for the disconnected contribution in our calculation we collaborated with the Hadron Spectrum collaboration. We combined their light quark disconnected correlators with a clear signal generated using the distillation method [111, 112] and our methods of calculating HVP [74, 95]. Of course, these correlators have been calculated at heavier than physical light quark masses and using distillation, a method that relies on computing the correlator directly using

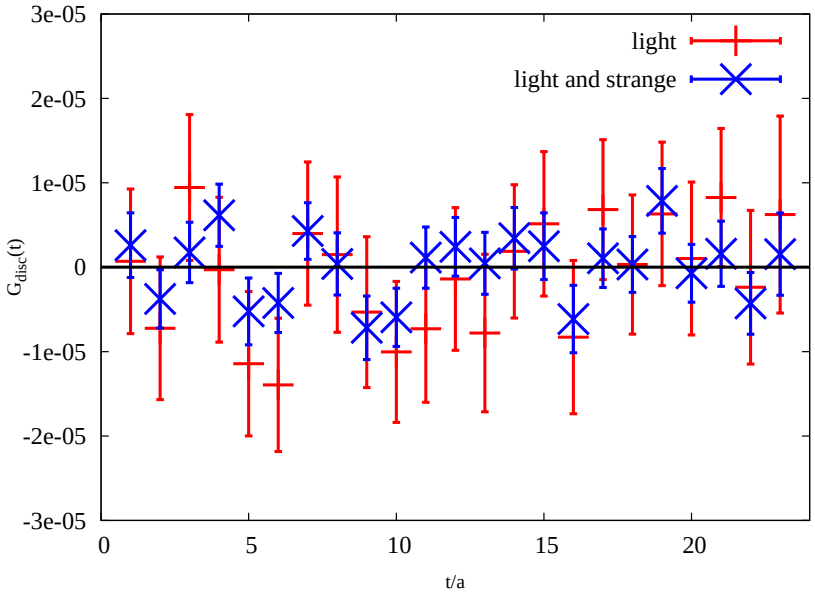

Figure 4.13: In this plot, the disconnected correlators made from light/light and from (light-strange)/(light-strange) currents are being compared. We can clearly see that the latter is much less noisy.

sources made from a basis of vectors spanning the space of the smoothest quark fields [107]. Therefore, these correlators have been normalised by the connected correlators generated by the Hadron Spectrum Collaboration using the same method of distillation.

At large time the disconnected light-light correlator is given by the difference between the ω and the ρ (assuming ρ dominance)

$$2D_{ll,gs} = -\frac{f_\rho^2 m_\rho}{2} e^{-m_\rho t} + \frac{f_\omega^2 m_\omega}{2} e^{-m_\omega t} \tag{4.38}$$

where $D_{ll,gs}$ is the ground state for the l/l disconnected correlator.

Following the notation from reference [112], the total disconnected correlator would be

$$\begin{aligned} D &= D^{ll} + D^{ss} - 2D^{ls} && (4.39) \\ &\equiv D^{l-s} \times D^{l-s}. && (4.40) \end{aligned}$$

where D^{ll} is disconnected l/l piece, D^{ss} is disconnected s/s piece and D^{l-s} is the $(l-s)/(l-s)$ disconnected piece.

We have to take time moments for this total D to calculate the total disconnected contribution to $a_\mu^{\mathrm{HVP,LO}}$.

In figure 4.14, we show the ratios ($R^{ff'}$) of the Hadron Spectrum disconnecetd correlators (described in equation 4.39) to their connected light-light correlators, both generated with the same operators. As expected all the ratios are negative and R^{ll} has the largest magnitude while R^{ss} is the smallest. This plot also shows the ratio we need to calculate the disconnected contribution to HVP.

Then using our method of time moments and the fit techniques [74, 95], we obtain an estimation of the total quark-line disconnected contribution to $a_\mu^{\mathrm{HVP,LO}}$ from a clear signal for the first time. It is -0.15% of the light quark connected contribution with an uncertainty of 1% of that connected contribution coming from the $\pi\pi$ effect at heavier masses [107]. After our work has been published, another calculation of

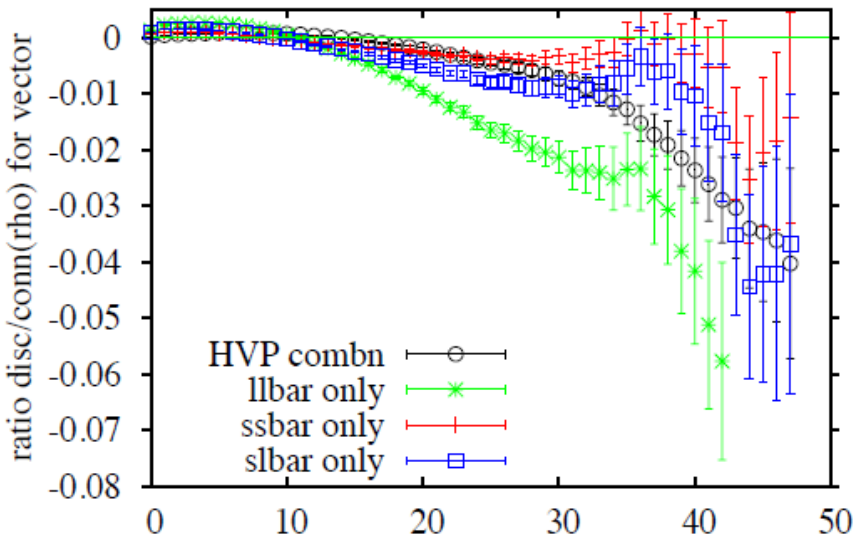

Figure 4.14: Ratios of disconnected correlators, $D^{ff'}$, to the connected correlator C^{ll}, as a function of time in lattice units. Open black circles show the combination of disconnected correlators needed for the hadronic vacuum polarisation contribution to HVP , described by equation 4.38

the disconnected contribution to $a_\mu^{\mathrm{HVP,LO}}$ was done by RBC/UKQCD [113] with the light quark masses close to the physical values and the result $-9.3(33)(23) \times 10^{-10}$ (statistical and systematic uncertainties in the parentheses) is consistent with our estimation.

4.9 Results for $a_\mu^{\mathrm{HVP,LO}}$

Table 4.4 gives the values of the Taylor coefficients Π_j (in equation 4.26) in units of GeV^{2j} for the i-th moment on each configuration for the connected s-quark contribution to $a_\mu^{\mathrm{HVP,LO}}$. The errors given include the statistical and the systematic (correlated) uncertainties from setting the lattice spacing using w_0. The estimates of the connected contribution from s-quarks to $a_\mu^{\mathrm{HVP,LO}}$ are also given for each of the $[1,0], [1,1], [2,1]$ and $[2,2]$ Padé approximants [95].

We fit the results of a_μ^s using the $[2,2]$ Padé approximants from each configuration

Table 4.4: Columns $2-5$ give the Taylor coefficients Π_j (in equation 4.26) in units of GeV^{2j} for the i-th moment on each configuration for the s-quark connected local vector correlators. The errors given include statistics and the (correlated) uncertainty from setting the lattice spacing using w_0. Estimates of the connected contribution from s-quarks to $a_\mu^{\mathrm{HVP,LO}}$ are given for each of the $[1,0], [1,1], [2,1]$ and $[2,2]$ Padé approximants.

set	Π_1	Π_2	Π_3	Π_4	$[1,0] \times 10^{10}$	$[1,1] \times 10^{10}$	$[2,1] \times 10^{10}$	$[2,2] \times 10^{10}$
1	0.06598(76)	-0.0516(11)	0.0450(15)	-0.0403(19)	58.11(67)	53.80(59)	53.95(59)	53.90(59)
2	0.06648(75)	-0.0523(11)	0.0458(15)	-0.0408(18)	58.55(66)	54.19(58)	54.33(59)	54.29(59)
3	0.06618(75)	-0.0523(11)	0.0466(15)	-0.0425(20)	58.28(66)	53.93(58)	54.09(58)	54.04(58)
4	0.06614(74)	-0.0523(11)	0.0467(15)	-0.0427(19)	58.25(65)	53.90(57)	54.06(58)	54.01(57)
5	0.06626(74)	-0.0527(11)	0.0473(15)	-0.0438(19)	58.36(65)	53.99(57)	54.15(57)	54.10(57)
6	0.06829(77)	-0.0557(12)	0.0514(17)	-0.0490(22)	60.14(67)	55.55(59)	55.73(59)	55.67(59)
7	0.06619(74)	-0.0524(11)	0.0468(15)	-0.0430(19)	58.29(65)	53.93(57)	54.10(57)	54.05(57)
8	0.06625(74)	-0.0526(11)	0.0470(15)	-0.0429(19)	58.34(65)	53.98(57)	54.14(57)	54.09(57)
9	0.06616(77)	-0.0531(12)	0.0483(17)	-0.0450(22)	58.27(68)	53.87(59)	54.04(60)	53.99(59)
10	.06630(72)	-0.0534(11)	0.0487(16)	-0.0458(20)	58.39(64)	53.98(56)	54.15(56)	54.10(56)

set to a function of the form

$$\begin{aligned} a^s_{\mu,\mathrm{lat}} &= a^s_\mu \\ &\times \left(1 + c_{a^2}\left(a\Lambda_{\mathrm{QCD}}/\pi\right)^2 + c_{\mathrm{sea}}\delta x_{\mathrm{sea}} + c_{\mathrm{val}}\delta x_{\mathrm{val}}\right), \end{aligned} \tag{4.41}$$

where $\Lambda_{\mathrm{QCD}} = 0.5\,\mathrm{GeV}$ and

$$\delta x_{\mathrm{sea}} \equiv \sum_{q=u,d,s} \frac{m_q^{\mathrm{sea}} - m_q^{\mathrm{phys}}}{m_s^{\mathrm{phys}}}, \qquad \delta x_s \equiv \frac{m_s^{\mathrm{val}} - m_s^{\mathrm{phys}}}{m_s^{\mathrm{phys}}}. \tag{4.42}$$

The discretisation effects are handled by c_{a^2}. The fit from all 10 of our configuration sets is excellent, with a χ^2 per degree of freedom of 0.22 and p-value of 0.99.

Using our method we have achieved [95] an unprecedented uncertainty of 1.1%, for the strange quark connected contribution to $a_\mu^{\mathrm{HVP,LO}}$ (shown in the Figure 4.15)

$$a^s_{\mu,\mathrm{HVP}} = 53.41(59) \times 10^{-10}. \tag{4.43}$$

Here the lattice spacing uncertainty alone contributes $\sim 1\%$ and needs to be improved to achieve a better precision. We found that the finite volume effect was negligibly small whereas the valence HISQ strange quark mass de-tuning effect was significant.

Our result for $a^s_{\mu,\mathrm{HVP}}$ in the continuum limit agrees with the subsequent lattice results by the ETM [114] and RBC/UKQCD Collaborations [115, 116] (shown in Table 4.5). However, using the HISQ quarks we have very small discretisation effects in our calculation compared to what ETMC has obtained which is clear from Figure 4.16. The charm quark contribution (connected) to $a_\mu^{\mathrm{HVP,LO}}$ has also been calculated from the previously obtained moments [100] and found as $14.42(39) \times 10^{-10}$. This piece could have been extracted with a similar precision of $\sim 1\%$ by improving the calculation of $Z_{V,\bar{c}c}$ following the same procedure for calculating $Z_{V,\bar{s}s}$ [59]. However, given the small value of a^c_μ, the uncertainty is not significant. Table 4.5 gives a comparison of our results for $a^s_{\mu,\mathrm{HVP}}$ and $a^s_{\mu,\mathrm{HVP}}$ with ETMC and RBC/UKQCD lattice calculations and the existing most accurate other calculations.

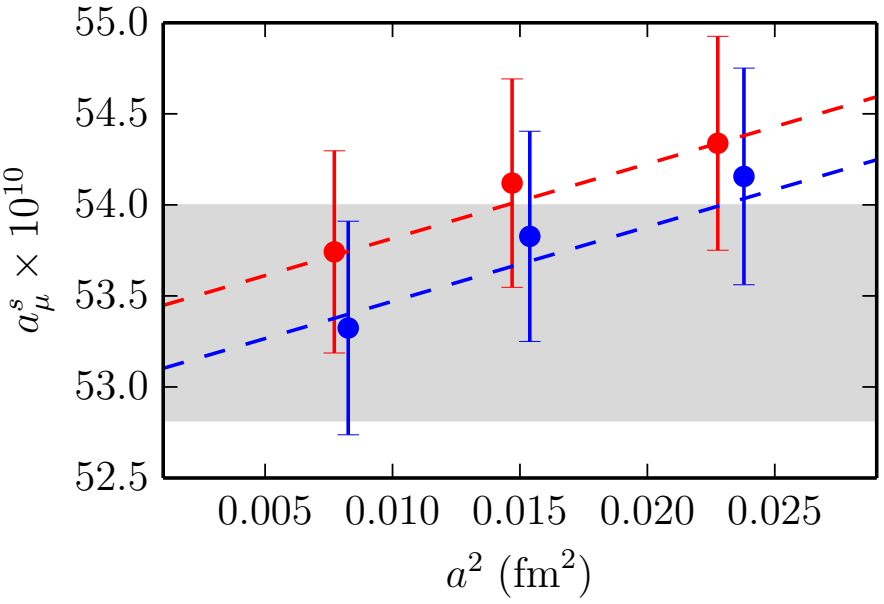

Figure 4.15: $a^s_{\mu,\mathrm{HVP}}$ for different lattice spacings and different light quark masses shown; the grey band gives the final results after chiral-continnum fit and finite volume correction.

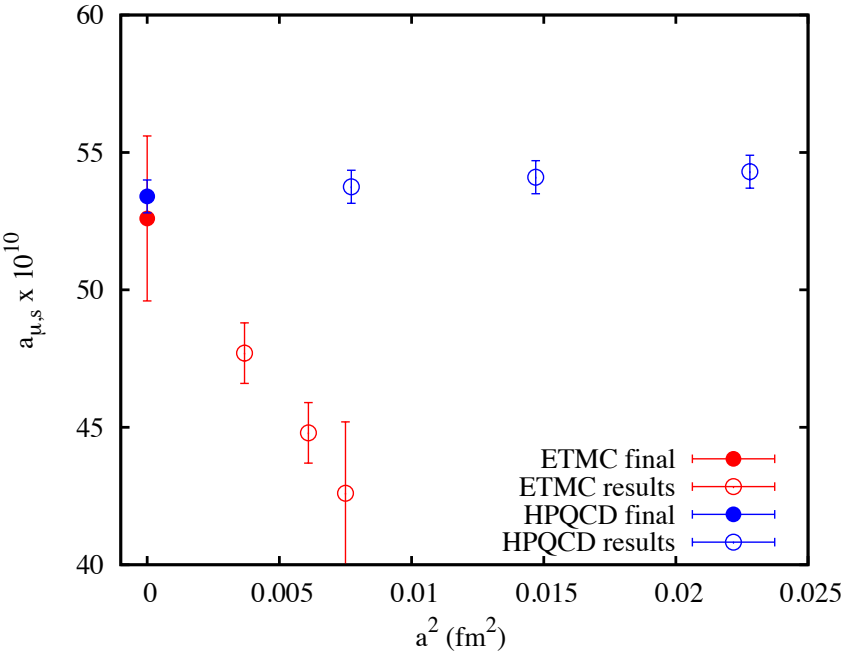

Figure 4.16: Comparison of our results for $a^s_{\mu,\mathrm{HVP}}$ on the emsembles with physical dynamical quark masses with that calculated by ETMC with heavier than physical masses [114].

Table 4.5: Comparison of our results for $a^{s}_{\mu,\mathrm{HVP}}$ and $a^{c}_{\mu,\mathrm{HVP}}$ [95] with ETMC [114] and RBC/UKQCD [115, 116] lattice calculations and the results using the dispersion relation and the experimental results on $e^+e^- \to$ hadrons or τ decay (dispersion relation for strange is just an estimate).

$a_\mu^{s/c}$	dispersion + experiment	Our results	ETMC (preliminary)	RBC/UKQCD
a_μ^s	55.3(8)x10^{-10} [71, 95]	53.41(59)x10^{-10}	53(3)x10^{-10}	53.1(9)x10^{-10}
a_μ^c	14.4(1)x10^{-10} [117]	14.42(39)x10^{-10}	14.1(6)x10^{-10}	-

Table 4.6: Here we list the masses of pion am_π and that of ρ meson am_ρ in lattice unit obtained from the light connected vector meson correlators. $Z_{V,\bar{s}s}$ is the vector current renormalisation [59] [74].

Set	am_π	am_ρ	$Z_{V,\bar{s}s}$
1	0.236430(90)	0.6669(18)	0.9887(20)
2	0.166170(70)	0.6113(51)	0.9887(20)
3	0.101720(40)	0.5978(44)	0.9887(20)
4	0.189380(80)	0.5268(38)	0.9938(17)
5	0.134920(80)	0.4945(83)	0.9938(17)
6	0.134150(50)	0.4866(51)	0.9938(17)
7	0.134010(60)	0.4848(49)	0.9938(17)
8	0.081620(40)	0.4732(27)	0.9938(17)
9	0.14062(10)	0.3849(39)	0.9944(10)
10	0.09850(10)	0.3507(42)	0.9944(10)

Table 4.6 lists the meson properties extracted from the light quark vector correlator analysis such as the pion and ρ meson masses. The time moments calculated from the correlators and the light quark connected cntribution to HVP a_μ^{light} are given in Table 4.7. Our results for the ρ meson properties are shown in Figure 4.17 with a comparison to previous lattice results.

Our results agree well with the experimental results for physical light quark masses and using HISQ the discretisation effects are much smaller in our calculation than in other lattice results.

Our results for the Taylor coefficients Π_j for the light quark connected vector correlator on each ensemble are listed in Table 4.7. At the same time, in Table 4.7

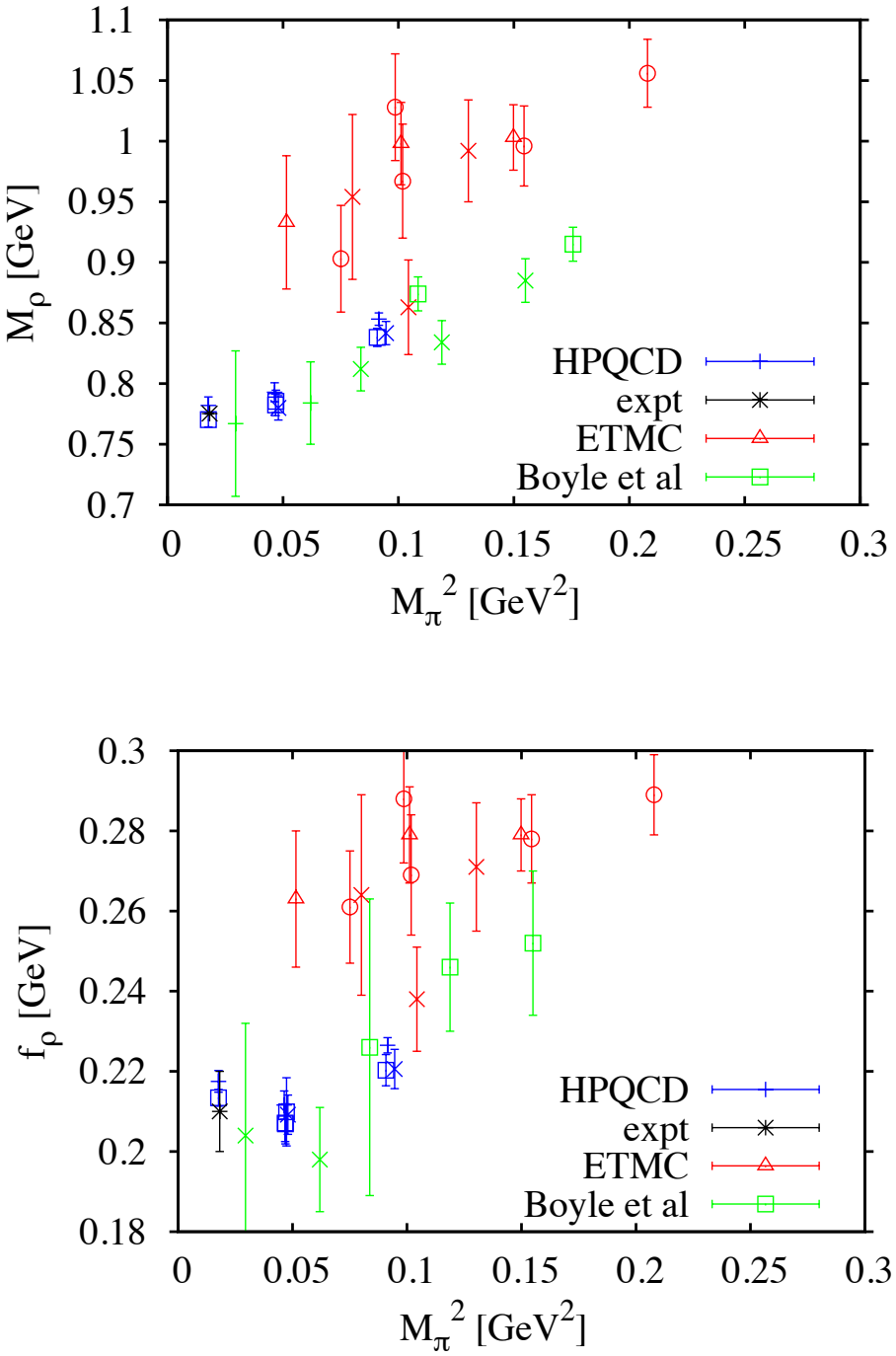

Figure 4.17: Comparison plots of the mass and the decay constant of ρ meson with different pion masses squared: Our numbers (HPQCD) in Red, ETMC results [18] in Blue, RBC/UKQCD results in Green [118] and experimental results in Black

Table 4.7: Columns $2-5$ give the uncorrected Taylor coefficients Π_j (equation 4.26) in units of GeV^{2j} for each data sets in table 4.6. The errors given include statistics and the (correlated) uncertainty from setting the lattice spacing using w_0. Estimates of the connected contribution from ud-quarks to $a_\mu^{\mathrm{HVP,LO}}$ are given for each of the $[1,0],[1,1],[2,1]$ and $[2,2]$ Padé approximants in columns $6-9$ after the correction of moments. The last column gives our final estimates for $a_\mu^{\mathrm{HVP,LO}}$ [74].

set	Π_1	Π_2	Π_3	Π_4	$[1,0]\times 10^{10}$	$[1,1]\times 10^{10}$	$[2,1]\times 10^{10}$	$[2,2]\times 10^{10}$	$a_\mu^{HVP,LO}\times 10^{10}$
1	0.0624 (7)	-0.0762(17)	0.102 (3)	-0.140 (6)	658.8 (3.4)	589.4 (3.0)	591.9 (3.1)	590.9 (3.2)	591.4 (3.2)
2	0.0731(11)	-0.1033(32)	0.160 (8)	-0.254(17)	661.8 (6.5)	589.5 (5.6)	593.5 (6.0)	591.3 (5.9)	592.6 (6.0)
3	0.0795(13)	-0.1178(38)	0.189 (9)	-0.308(21)	691.2 (9.2)	603.8 (8.9)	617.6 (11.6)	608.4 (10.7)	613.0 (11.7)
4	0.0639 (8)	-0.0804(21)	0.112 (5)	-0.158 (9)	648.7 (6.3)	581.2 (5.3)	583.7 (5.3)	582.7 (5.3)	583.2 (5.4)
5	0.0715(13)	-0.0989(41)	0.151(11)	-0.234(24)	654.5 (14.2)	583.9 (11.9)	587.8 (12.1)	585.7 (12.0)	586.8 (12.0)
6	0.0736(11)	-0.1052(33)	0.166 (9)	-0.267(20)	650.6 (8.8)	581.0 (7.4)	584.9 (7.6)	582.8 (7.5)	583.9 (7.6)
7	0.0744(11)	-0.1075(34)	0.171 (9)	-0.278(20)	652.2 (8.1)	582.5 (6.8)	586.3 (7.0)	584.3 (7.0)	585.3 (7.0)
8	0.0811(12)	-0.1238(36)	0.205 (9)	-0.344(20)	675.3 (7.6)	592.5 (7.5)	605.8 (9.9)	596.8 (9.1)	601.3 (10.2)
9	0.0625 (9)	-0.0780(25)	0.108 (6)	-0.152(11)	638.9 (7.6)	573.1 (6.5)	575.5 (6.5)	574.6 (6.5)	575.1 (6.5)
10	0.0756(13)	-0.1111(41)	0.179(11)	-0.293(25)	652.0 (8.5)	583.2 (7.2)	586.5 (7.3)	584.7 (7.2)	585.6 (7.3)

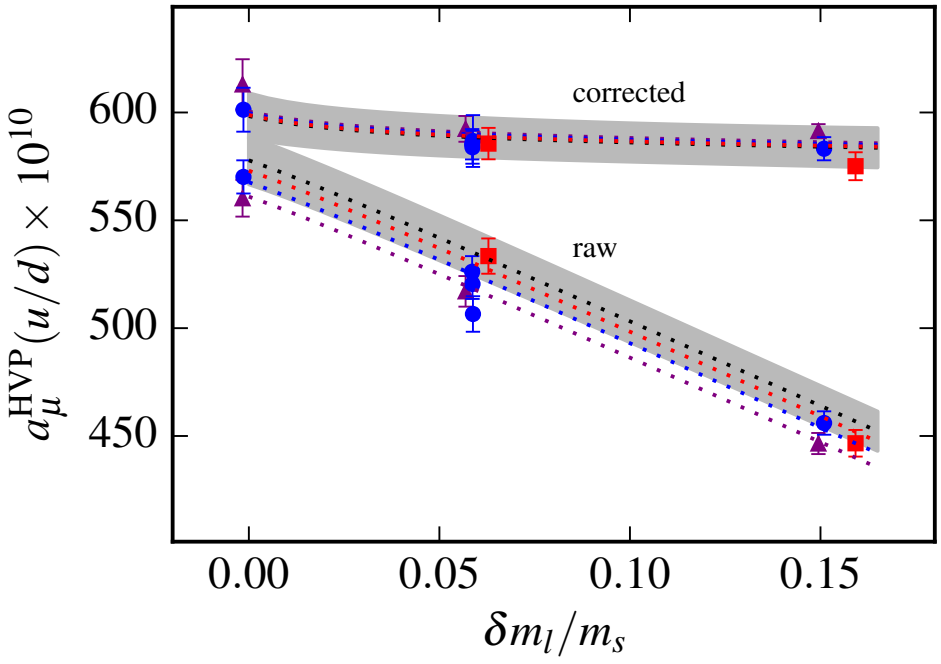

Figure 4.18: The connected contribution to the muon anomaly a_μ from the vacuum polarisation of u/d quarks, both uncorrected and rescaled (corrected), for the three lattice spacings, and the three light-quark masses are shown. δm_l represents the deviation of the valence light quark mass used on each ensemble from the physical light quark mass. The dashed lines are the corresponding values from the fit function, using the best-fit parameters. The gray band for the corrected results shows our final result, $598(11) \times 10^{-10}$, after chiral-continuum extrapolation.

we also list the estimation for $a_\mu^{\rm light}$ for different Padé approximants after correcting the time moments and then the final results for $a_\mu^{\rm HVP,LO}$.

Our results for $a_\mu^{\rm light}$ are shown in Figure 4.18. The rescaled values are independent of m_l/m_s, a^2, the finite volume effects. Fitting the corrected results as a function of a^2 and $m_{\rm sea}$ yields a result of $a_\mu^{\rm light} = 598(11) \times 10^{-10}$ including 1% QED and 1% isospin uncertainties.

We fit the corrected results of $a_\mu^{\rm light}$ using the $[2,2]$ Padé approximants from each configuration set to a function of the form

$$a_{\mu,\rm lat}^{\rm light} = a_\mu^{\rm light} \times \left(1 + c_{a^2}\left(a\Lambda_{\rm QCD}/\pi\right)^2 + c_{\rm sea}\delta x_{\rm sea} + c_{\rm val}\delta x_{\rm val}\right),$$

where $\Lambda_{\rm QCD} = 0.5\,\text{GeV}$.

Table 4.8: This table gives our results for the contributions to the HVP coming from each of the flavour separated connected and the disconnecetd pieces and then the final result for total $a_\mu^{\rm HVP,LO}$ from our lattice simulation.

Contribution	Result (x 10^{-10})	
light, conn	598(11)	(including 1% for each of QED and isospin effects)
strange, conn	53.4 (6)	(1403.1778)
charm, conn	14.4(4)	(1403.1778, 1208.2855)
bottom, conn	0.27(4)	(1408.5768)
disconn. (estimate)	0(9)	take 1.5% as uncertainty; contribution negative
Total	666(6)(12)	

The discretisation effects are handled by c_{a^2} as before. The fit from all ~ 10 of our configuration sets is excellent, with a χ^2 per degree of freedom of ~ 0.9 for the corrected data and ~ 0.6 for the uncorrected data. The $[2,2]$ Padé approximants converged to a better than 0.2% and therefore contributed negligibly to the total uncertainty. In our calculation we have removed the systematic uncertainties except for the QED and the isospin breaking effects which are reasonably taken as $\sim 1\%$ each. The total uncertainty which is less than 2% is dominated by these systematic errors.

4.10 Result for total $a_\mu^{\rm HVP,LO}$

Table 4.8 shows the contributions to HVP coming from the connected contribution for each of the quark flavours and the disconnected pieces.

Therefore, our estimation of the entire HVP contribution to the anomalous magnetic moment of the muon is

$$a_\mu^{\rm HVP,LO} = 666(6)(12) \times 10^{-10} \tag{4.44}$$

including all the systematics (with 1% QED and 1% isospin uncertainties).

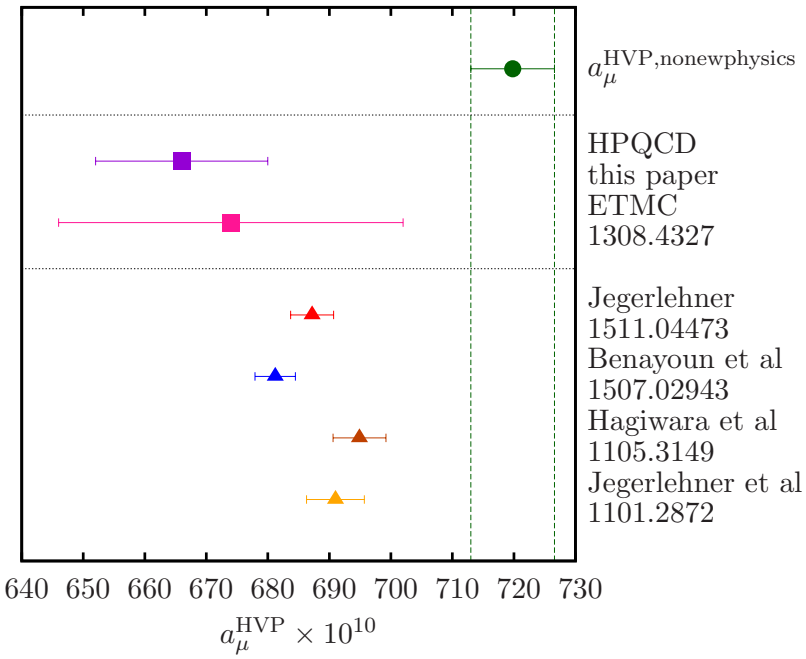

Figure 4.19: In this plot I have compared our result for $a_\mu^{\mathrm{HVP,LO}}$ with that from other lattice and non-lattice results. We can clearly see that our (HPQCD) result is $\sim 3.5\sigma$ away from the result that we should have found if there is no new physics.

Figure 4.19 shows that our result for $a_\mu^{\mathrm{HVP,LO}}$ agrees well with previous lattice result $674(28)\times10^{-10}$ [18] and the non-lattice results - $694.9(43)\times10^{-10}$ [71], $690.8(4.7)\times 10^{-10}$ [106], $681.9(3.2)\times10^{-10}$ [119] and $687.2(3.5)\times10^{-10}$ [120]. Though we have not yet achieved the level of precision comparable to phenomenology, the spread between the phenomenological results is of the same size as the uncertainty in our result.

It is interesting to see the implication of our result compared to the experimental scenario. Let us assume there is no new physics beyond the Standard Model. Then the question is what value of $a_\mu^{\mathrm{HVP,LO}}$ we expect to get. Subtracting the QED [70] and the EW [77] contributions from the experimental value of total a_μ we get $721.7(6.3)\times10^{-10}$ which should be the value of the total hadronic contributions in the absence of new physics. If we subtract the other hadronic contributions such as hadronic-light-by-light $(10.5(2.6)\times10^{-10})$ [73] and higher order HVP $(-8.85(9)\times10^{-10})$ [71,75] from this value then we expect $a_\mu^{\mathrm{HVP,LO}}$ to be $719.8(6.8)\times10^{-10}$ if no new physics exists. Interestingly

we observe a 3.5σ deviation of our result from this expected value (shown in Figure 4.19), still we can not claim new physics unless the uncertainties in our calculations are reduced to $\sim 0.5\%$.

Part IV

Flavour physics with HISQ

Chapter 5

Semileptonic meson decay: $D \to Kl\nu$

5.1 Motivation

The flavour changing weak interactions between quarks via emission of W bosons can be parametrised in terms of the Cabbibo-Kobayashi-Maskawa (CKM) unitary matrix in the Standard Model given by [121, 122]

$$V_{\rm CKM} = \begin{bmatrix} V_{ud} & V_{us} & V_{ub} \\ V_{cd} & V_{cs} & V_{cb} \\ V_{td} & V_{ts} & V_{tb} \end{bmatrix}. \tag{5.1}$$

Precise and independent determination of each of the CKM matrix elements is crucial to test the Standard Model stringently, and any deviation from unitarity would signal the existence of physics beyond the Standard Model.

The unitarity of the first row has already been precisely tested giving [66]

$$|V_{ud}|^2 + |V_{us}|^2 + |V_{ub}|^2 = 0.9999 \pm 0.0006. \tag{5.2}$$

Here V_{ub} has negligible contribution, V_{ud} has been measured with 0.02% accuracy from experiment and theory, and V_{us} has been determined with sub-percent level

accuracy combining experimental measurement and lattice QCD results. Also, the unitarity of the first column has been tested precisely (although not as precisely as the first row):

$$|V_{ud}|^2 + |V_{cd}|^2 + |V_{td}|^2 = 1.000 \pm 0.004. \tag{5.3}$$

However, it has not been possible so far to test the second row unitarity with a similar precision. At present what we have is [66]

$$|V_{cd}|^2 + |V_{cs}|^2 + |V_{cb}|^2 = 1.024 \pm 0.032. \tag{5.4}$$

The same is true for the second column unitarity checks in which case we have so far obtained

$$|V_{us}|^2 + |V_{cs}|^2 + |V_{ts}|^2 = 1.025 \pm 0.032. \tag{5.5}$$

The uncertainties in the unitarity checks of the second row and second column of the CKM matrix are dominated by that of $|V_{cs}|$, the central CKM matrix element. This element is calculated from studies of the semileptonic meson decays involving charged flavour changing current from c to s by combining the experimental decay rate with the vector form factor calculated from lattice QCD [121, 122]. However, currently the uncertainty in $|V_{cs}|$ is dominated by the lattice uncertainty in the form factors. For precise determination of $|V_{cs}|$ we need to achieve a lattice computation of the form factors with similar precision as the experimental decay rate. In the past, simulating the c-quarks on the lattice posed a challenge as the c-quark was heavier than the lattice cut off. Therefore, the NRQCD or the Fermilab heavy clover action was used to simulate the charm quark on the lattice. Using such an effective theory, the first unquenched calculation of D meson semileptonic decays with $N_f = 2 + 1$ was done by the Fermilab lattice and MILC collaborations [123] and was a pioneering work as it predicted the shape of the form factors with $\sim 10\%$ uncertainty even before any experiment was done in this sector.

Using effective theory gives large systematic uncertainties arising from the perturbative determination of the heavy-light current renormalisations. With the development of the relativistic HISQ formalism [17] which removes all $\mathcal{O}(am_c)^2$ and $\mathcal{O}(\alpha_s(am_c)^2)$ artifacts and the availability of HISQ lattices with $a \leq 0.15$ fm, it has been possible to simulate the c-quark relativistically.

Among various works carried out by HPQCD collaboration, the study of the D and D_s meson leptonic decays [62] and D meson semileptonic decay [35, 36] are noteworthy. Among some of the important works done by other collaborations, those of the Fermilab lattice collaboration and ETMC [123, 124] are worth mentioning. In the latest study of D meson semileptonic decays by the Fermilab lattice and MILC collaborations [125] on HISQ $N_f = 2 + 1 + 1$ lattices, they have calculated the scalar form factor at the zero q^2 exchange (from D to K meson) limit to extract $|V_{cs}|$.

With a large worldwide experimental program providing flavour physics data- LHCb and NA62 at CERN, BES-III in Beijing, KLOE-2 in Frascati and KOTO at J-PARC (Japan); and the forthcoming Belle-II at J-PARC- the development of new and continued refinement of existing lattice QCD methods is required to attain precise theoretical predictions that can match the increasing precision of the experimental data.

For my dissertation I have studied the semileptonic $D \to Kl\nu$ decay on HISQ $N_f = 2 + 1 + 1$ lattices. In contrast to the work done by the Fermilab lattice and MILC collaboration [125], I have calculated both its scalar and vector form factors over the whole range of physical kaon momentum instead of only at the maximum kaon momentum. However, I have only used the scalar form factor at the zero momentum exchange (from D to W boson) limit to extract $|V_{cs}|$ for the purpose of this dissertation, though in future this study will be extended to include all experimental momentum bins and their correlations, following reference [35].

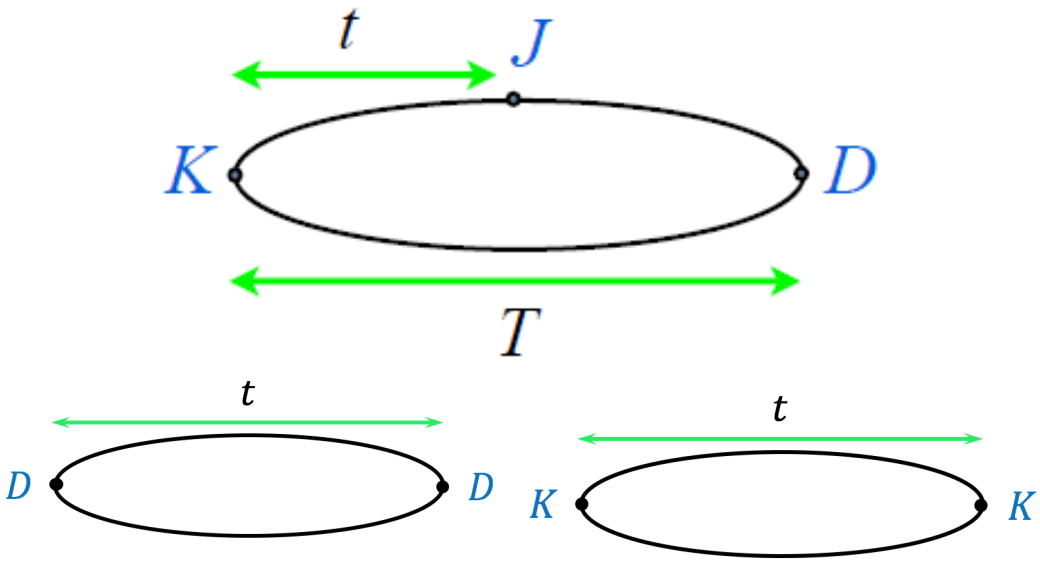

Figure 5.1: The diagram represents the three-point correlator for the $D \to Kl\nu$ semileptonic decay (on the top) and the two-point correlators for the D and K mesons (at the bottom).

5.2 Formalism

Let us consider the matrix element of the $D \to Kl\nu$ semileptonic decay by the charged electroweak current (in Figure 5.2). In the one W exchange approximation, the amplitude becomes

$$\begin{aligned} \langle K^- l^+ \nu | J_W | D^0 \rangle &= \frac{G_F}{\sqrt{2}} V_{cs} \bar{v}(l) \gamma_\mu (1 - \gamma_5) u(\nu) \\ &\quad \langle K^- | \bar{\psi_s} \gamma_\mu (1 - \gamma_5) \psi_c | D^0 \rangle. \end{aligned} \tag{5.6}$$

where G_F is the Fermi constant and the amplitude has been factorised into leptonic and hadronic parts. The leptonic part can be straightforwardly evaluated whereas for calculating the hadronic part

$$\langle H_\mu \rangle = \langle K^- | \bar{s} \gamma_\mu (1 - \gamma_5) c | D^0 \rangle$$

we need to rely on the non-perturbative method of lattice QCD. $\langle H_\mu \rangle$ gets a contribution only from the vector current V_μ for pseudoscalar to pseudoscalar decay and can be parametrised in different ways. We will consider one of those where it can be written in terms of the scalar and vector form factors $f_0(q^2)$ and $f_+(q^2)$. Here, $q^\mu = p_D^\mu - p_K^\mu$ is

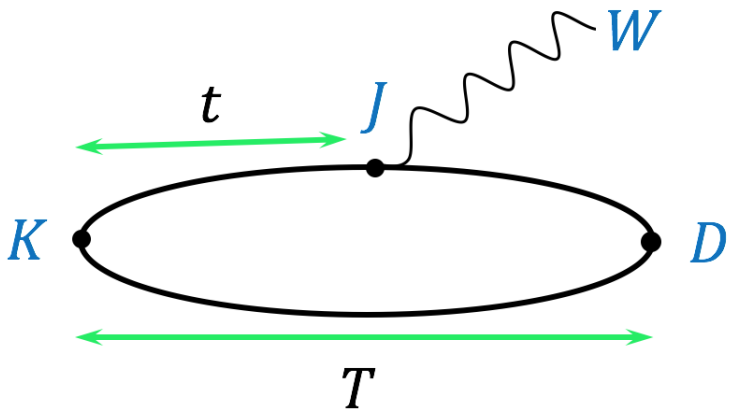

Figure 5.2: The diagram represents the $D \to Kl\nu$ semileptonic decay by charged electroweak current with one W exchange.

the exchanged 4-momentum from D with a 4-momentum p_D^μ to K with a 4-momentum p_K^μ with the difference carried away by the W boson. The parametrisation can be written as

$$\begin{aligned} Z_{V,t} \times \langle K^-|V^\mu|D^0\rangle &= f_+^{D\to K}(q^2)[p_D^\mu + p_K^\mu - \frac{M_D^2 - M_K^2}{q^2}q^\mu] \\ &\quad + f_0^{D\to K}(q^2)\frac{M_D^2 - M_K^2}{q^2}q^\mu \end{aligned} \tag{5.7}$$

where, M_D and M_K are the masses of the D and K mesons respectively. In our setup, we give momentum to the strange quark inside the K meson.

The local vector current using our lattice formalism, HISQ, is not conserved. Therefore it requires a matching factor Z_V to obtain the continuum result. For easier calculation of the Z_V factor and a better signal I have used only local temporal vector current and calculated $Z_{V,t}$ from $\langle S^{latt}\rangle$ and other kinematic factors. The complete non-perturbative calculation of $Z_{V,t}$ reduces systematic uncertainties significantly over neglecting higher-order terms in the perturbative calculation; as demonstrated in Chapter 3. The scalar current using HISQ is perfectly renormalised when multiplied by the lattice quark mass [36].

For calculating $Z_{V,t}$ we consider the kinematics at $q^2 = q^2_{\rm max} = (M_D - M_K)^2$ i.e.

$\vec{p}_K = \vec{0}$. Under this condition, equation 5.7 becomes

$$\begin{aligned} Z_{V,t} \times \langle K^-|V^0|D^0\rangle &= f_+^{D\to K}(q^2)[M_D + M_K - (M_D + M_K)] \\ &\quad + f_0^{D\to K}(q^2)(M_D + M_K) \qquad (5.8) \\ &= (M_D + M_K) \times f_0^{D\to K}(q^2_{\max}) \qquad (5.9) \end{aligned}$$

Now, the scalar current amplitude is parametrised as

$$\langle K^-|S|D^0\rangle = \frac{M_D^2 - M_K^2}{m_{0c} - m_{0s}} f_0^{D\to K}(q^2) \qquad (5.10)$$

Inverting this equation the scalar form factor for different q^2 can be extracted.

$$f_0^{D\to K}(q^2) = \frac{(m_{0c} - m_{0s})\langle K^-|S|D^0\rangle}{M_D^2 - M_K^2} \qquad (5.11)$$

Plugging in the $f_0^{D\to K}(q^2)$ values from equation 5.11 into equation 5.9 we can extract $Z_{V,t}$. For different kinematic combinations we can extract the vector form factor $f_+^{D\to K}(q^2)$ by plugging in the $f_0^{D\to K}(q^2)$ values from equation 5.11 into equation 5.7. In this way we can cover the full physical range of q^2 starting from $q^2_{\max}$ where the momentum exchange is maximum i.e. K meson is at rest down to $q^2 = 0$ where K gets the maximum possible momentum in the opposite direction to the leptons.

Under the condition that $\vec{p}_D = \vec{p}_K$ or momentum exchange $\vec{q} = \vec{0}$, i.e. in the center of mass frame of the decay leptons, we get

$$\begin{aligned} \langle K^-(p_K)|\bar{\psi}_s \vec{\gamma} \psi_c|D^0(p_D)\rangle &= 2\vec{p}_D f_+^{D\to K}(q^2) \\ \langle K^-(p_K)|\bar{\psi}_s \gamma_4 \psi_c|D^0(p_D)\rangle &= \frac{m_D^2 - m_K^2}{q} f_0^{D\to K}(q^2). \qquad (5.12) \end{aligned}$$

Therefore, $f_0(q^2)$ corresponds to the exchange of a scalar particle and $f_+(q^2)$ is associated with a vector particle exchange.

The differential decay rate is dominated by the vector channel in the vanishing lepton mass limit [126] and we get

$$d\Gamma(q^2) = \frac{G_F^2 |V_{cs}|^2}{192\pi^3 m_D^3} dq^2 \lambda(q^2)^{3/2} |f_+(q^2)|^2 \qquad (5.13)$$

where $\lambda(q^2)$ is the phase-space term.

My goal is to calculate $f_+(q^2 = 0)$ i.e. the vector form factor precisely from lattice QCD such that $|V_{cs}|$ can be extracted with high precision. In future I plan to compare the experimental decay rate to lattice results over all q^2 bins rather than only $q^2 = 0$ limit [36, 123–125] and calculate $|V_{cs}|$, however, for the purpose of this dissertation, I will continue to exploit the kinematic relation $f_+(q^2 = 0) = f_0(q^2 = 0)$ to calculate $|V_{cs}|$, although I am doing the full analysis.

5.3 Lattice setup

The scalar and local temporal vector current amplitudes of the $D \to Kl\nu$ semileptonic decay are extracted from the three-point correlation functions on lattice. In this set up a zero momentum D meson is created at time $t_0 + T$ on lattice, after it propagates to time t on lattice, the current (scalar or local temporal vector) is inserted at time t which changes the flavour c inside the D meson to flavour s to create a K meson and emit a W boson. Therefore, in our simulation an s-quark propagator runs from t_0 to t whereas the light quark (spectator quark) propagator runs from t_0 to $t_0 + T$. The K propagates from time t to time t_0 on the lattice and is annihilated at that time, where, $t_0 < t < t_0 + T$. The c-quark propagator is generated from $t_0 + T$ considering the value of the light quark propagator at this particular time slice as the source of the c propagator. This approach is known as the "sequential technique" and the propagator generated in this way is called as the "extended propagator".

The values of t_0 have been chosen randomly to reduce autocorrelation and for each configuration multiple values of t_0, uniformly placed on the lattice, have been used to get better statistics. To increase the statistics further, multiple values of the source-sink separation T have also been used for each t_0 value.

The K gets momentum p_K, which has been generated using twisted boundary conditions (as described in chapter 2) for the s-quark propagator. To access the whole

range of momentum transfer and generate several kinematics, K is given different momentum twists using twisted boundary conditions including that tuned to generate $q^2 = 0$ kinematics.

5.3.1 Staggered phases

As previously discussed, staggered quarks have four tastes running in the correlator loop. To get a non-zero expectation value of the scalar and vector current operator matrix elements, we need to choose correct combinations of operators at the source, sink and current insertion point such that the correlator becomes taste-singlet. For generating the scalar current amplitude, the current carries spin-taste $1 \otimes 1$. We keep the spin-taste at the K-meson annihilation point the same for both scalar and vector currents as we want to use the same strange propagators in both cases. This end has the spin-taste content $\gamma_5 \otimes \gamma_5$. To nullify the tastes, the simplest choice of operators for the D meson end is the Goldstone pseudoscalar operator $\gamma_5 \otimes \gamma_5$.

For the local temporal vector current, at the current insertion point I have used the $\gamma_t \otimes \gamma_t$ operator. As mentioned before, the same K meson propagators are used in this case as well, therefore we have a spin-taste operator $\gamma_5 \otimes \gamma_5$ at this end. Now, to cancel the overall taste the simplest operator choice at the D meson end would be the local non-Goldstone operator $\gamma_5\gamma_t \otimes \gamma_5\gamma_t$ which generates a D meson with slightly different mass. To use these three-point correlators we need to make Goldstone and local non-Goldstone two-point D correlators and Goldstone two-point K correlators as well.

5.3.2 Correlators using random wall sources

Let us say that $\phi_D^\dagger$ and ϕ_K are respectively the D meson creation and K meson annihilation operators, and S is the lattice current. Therefore, $\phi_K = \bar{\psi}_l\gamma_5\psi_s$, $\phi_D^\dagger =$

$\bar{\psi}_c\gamma_5\psi_l$, $S \equiv \bar{\psi}_s\psi_c$ is the scalar current and $V_0 \equiv \bar{\psi}_s\gamma_4\psi_c$ is the local temporal vector current.

Therefore the scalar current amplitude after applying the staggering transformation becomes [36]

$$\begin{aligned}\langle\phi_K(x)S(y)\phi_D^\dagger(z)\rangle &= \frac{1}{4}(-1)^{\sum_\mu y_\mu^<}(-1)^{\sum_\mu z_\mu^<} \\ &\quad\times\mathrm{Tr}[g_s^\dagger(y,x)g_c(y,z)g_l(z,x)]. \end{aligned} \tag{5.14}$$

Here, the 'g's are the staggered quark propagators and the summations have the following definition

$$y_\mu^< = \sum_{\nu<\mu} y_\nu, \tag{5.15}$$

$$z_\mu^< = \sum_{\nu<\mu} z_\nu. \tag{5.16}$$

Here μ and ν represent space-time directions.

Also, $x_0 \equiv t_0$, $y_0 \equiv t$, $z_0 \equiv t_0+T$. The trace is over colours only. In this calculation we are using the same random wall source for the light and strange quarks.

Therefore the three-point correlation function becomes

$$\begin{aligned} C^{3\mathrm{pt}}(t_0,t,T,\vec{p}_k) &= \frac{1}{L^3}\sum_{\vec{x},\vec{y},\vec{z}} e^{i\vec{p}_k.(\vec{z}-\vec{x})}\langle\phi_K(x)S(y)\phi_D^\dagger(z)\rangle \\ &= \frac{1}{L^3}\sum_{\vec{x},\vec{y},\vec{z}} \exp(i\vec{p}_k.(\vec{z}-\vec{x}))\big(\frac{1}{4}(-1)^{\sum_\mu y_\mu^<}(-1)^{\sum_\mu z_\mu^<} \\ &\quad\times\mathrm{Tr}[g_s^\dagger(y,x)g_c(y,z)g_l(z,x)]\big). \end{aligned} \tag{5.17}$$

We use random colour wall sources to gain better statistics and in this case the trace in equation 5.17 becomes

$$\langle\mathrm{Tr}[g_s^\dagger(y,x)g_c(y,z)g_l(z,x')\eta^\dagger(\vec{x})\eta(\vec{x}')]\rangle. \tag{5.18}$$

In the sequential approach the light quark propagator is generated with the source $\frac{1}{\sqrt{L^3}}\sum_{\vec{x}'}\eta(\vec{x}')$ and the s quark propagator is generated from the source $\frac{1}{\sqrt{L^3}}\sum_{\vec{x}}\eta(\vec{x})e^{i\vec{p}_K.\vec{x}}$.

These give us after fermion matrix inversions the following propagators for the light and s quarks -

$$g_l^{\rm Rwall}(z,t_0) \equiv \frac{1}{\sqrt{L^3}} \sum_{\vec{x}'} g_l(z,x')\eta(\vec{x}') \tag{5.19}$$

and

$$g_s^{\rm Rwall}(y,t_0,\vec{p}_k) \equiv \frac{1}{\sqrt{L^3}} \sum_{\vec{x}} g_s(y,x)\eta(\vec{x})e^{i\vec{p}_k.\vec{x}}. \tag{5.20}$$

The sequential c-quark propagator is generated by starting with a source

$$\textstyle\sum_{\vec{z}} \sum_{\mu} z_\mu^< g_l^{\rm Rwall}(z,t_0)$$

at the time slice t_0+T and then inverting the fermion matrix. The sequential c propagator is written as

$$g_c^{\rm seq}(y,t_0,T) \equiv \sum_{\vec{z}} \sum_{\mu} z_\mu^< g_c(y,z) g_l^{\rm Rwall}(z,t0). \tag{5.21}$$

In terms of the sequential propagator the three-point correlator for scalar current becomes -

$$C_{\rm Rwall}^{\rm 3pt,scalar}(t_0,t,T,\vec{p}_k) = \sum_{\vec{y}} \exp(i\vec{p}_k.\vec{y}) \frac{1}{4} \sum_{\mu} y_\mu^< \langle {\rm Tr}[g_s^{\dagger\,{\rm Rwall}}(y,t_0,\vec{p}) g_c^{\rm seq}(y,t_0,T)]\rangle \tag{5.22}$$

Similarly we can deduce the three-point correlator for the local temporal vector current using the sequential source technique, but now for lattice current $V=\bar{\psi}_s\gamma_t\psi_c$. We get an overall phase factor $(-1)^{t+T}$ in the three-point amplitude and the correlator with random wall sources look like

$$C_{\rm Rwall}^{\rm 3pt,scalar}(t_0,t,T,\vec{p}_k) = \sum_{\vec{y}} \exp(i\vec{p}_k.\vec{y}) \frac{1}{4} \langle {\rm Tr}[g_s^{{\rm Rwall}\,\dagger}(y,t_0,\vec{p}) g_c^{\rm seq}(y,t_0,T)]\rangle. \tag{5.23}$$

In the case of the local temporal vector current, the extended charm propagator is generated as

$$g_c^{\rm seq}(y,t_0,T) \equiv \sum_{\vec{z}} (-1)^{t_0+T} g_c(y,z) g_l^{\rm Rwall}(z,t0). \tag{5.24}$$

To extract the three-point amplitudes for both currents we also need to construct the two-point correlators for D and K. We should note that we need both Goldstone

and non-Goldstone D mesons in our calculation. The two point correlator for the Goldstone and non-Goldstone D meson is given as

$$C_D^{\rm 2pt}(t_0,t) = \frac{1}{L^3}\sum_{\vec{x},\vec{y}}\langle\phi_D(\vec{y},t)\phi_D^\dagger(\vec{x},t_0)\rangle \tag{5.25}$$

with the Goldstone operator $\phi_{D,\rm gold}(\vec{y},t) = \bar{\psi}_c\gamma_5\psi_l$ and the nonGoldstone operator $\phi_{D,\rm nongold}(\vec{y},t) = (-1)^t\bar{\psi}_c\gamma_5\gamma_t\psi_l$.

And the two-point correlator for the K meson is given by

$$C_K^{\rm 2pt}(t_0,t;\vec{p}_k) = \frac{1}{L^3}\sum_{\vec{x},\vec{y}}\exp(i\vec{p}_k.(\vec{x}-\vec{y}))\langle\phi_K(\vec{y},t)\phi_K^\dagger(\vec{x},t_0)\rangle. \tag{5.26}$$

5.3.3 Momentum twists

To cover the whole range of physical kaon momentum we undertake the lattice calculation of the form factors at four different q^2 values starting from $q^2_{\rm max}$ where $\vec{p}_K = \vec{0}$ to $q^2 = 0$ where the kaon gets the maximum momentum in the opposite direction to the decay leptons. The two intermediate values of momentum used in my calculations are $2q^2_{\rm max}/3$ and $q^2_{\rm max}/3$. Starting from these q^2 values with $q^2_{\rm max} = (M_D - M_K)^2$ we can deduce what momentum the K meson gains and what momentum twists we apply to the s-quark propagators in MILC code.

For $q^2 = 0$ case, the kaon gets 3-momentum-

$$\begin{aligned}\bar{p}_K &= \sqrt{\frac{(M_D^2+M_K^2)^2}{4M_D^2} - M_K^2} \\ &= \frac{M_D - M_K}{2M_D}\end{aligned} \tag{5.27}$$

with the corresponding momentum twist (same twist applied in the x, y and z directions) in the MILC code is

$$\theta = \frac{L}{\pi\sqrt{3}}\sqrt{\frac{(M_D^2+M_K^2)^2}{4M_D^2} - M_K^2}, \tag{5.28}$$

where L is the spatial length of the lattice. The momentum twist θ in the MILC code is given in units of π/L and I have used the same θ for all the three spatial directions. Therefore, $\vec{p}_K^2 = (\pi/L)^2 \times 3\theta^2$.

For $q^2 = 2q^2_{\rm max}/3$, kaon momentum and the momentum twist are given by

$$\bar{p}_K(\text{latt}) = \sqrt{\frac{\left(M_D^2 + M_K^2 + 4M_D M_K\right)^2}{36M_D^2} - M_K^2} \tag{5.29}$$

and

$$\theta = \frac{L}{\pi\sqrt{3}}\sqrt{\frac{\left(M_D^2 + M_K^2 + 4M_D M_K\right)^2}{36M_D^2} - M_K^2}. \tag{5.30}$$

For $q^2 = q^2_{\rm max}/3$, we use the following values for the kaon momentum and the momentum twist.

$$\bar{p}_K(\text{latt}) = \sqrt{\frac{\left(M_D^2 + M_K^2 + M_D M_K\right)^2}{9M_D^2} - M_K^2}. \tag{5.31}$$

And

$$\theta = \frac{L}{\pi\sqrt{3}}\sqrt{\frac{\left(M_D^2 + M_K^2 + M_D M_K\right)^2}{9M_D^2} - M_K^2}. \tag{5.32}$$

5.4 Simulation details

For this project I have used publicly available MILC HISQ $N_f = 2{+}1{+}1$ configurations with three different lattice spacing values $\sim$ 0.09 fm (fine), $\sim$ 0.12 fm (coarse), $\sim$ 0.15 fm (very coarse) and the physical values of the dynamical quark masses. This calculation is an improvement over the previous calculation done by HPQCD with $N_f = 2 + 1$ Asqtad quarks [35]. Also, in my calculation I have used the local temporal vector current for easier renormalisation and better statistics over the one-link spatial current used in reference [35]. The details of these configurations are given in Table 5.1.

Table 5.1: Sets of MILC configurations used for the study of the $D \to Kl\nu$ semileptonic decay with their $\beta = 6/g^2$ [22], w_0/a for $w_0 = 0.1715(9)$ fm fixed from f_π [25], L_s/a, L_t/a, number of configurations $N_{\rm conf}$, number of independent time sources for each configuration t_0, multiple values of the source-sink separation T for each t_0, (HISQ) sea quark masses- m_l, m_s and m_c in lattice units [22].

Set	β	w_0/a	L_s/a	L_t/a	$N_{\rm conf}$	t_0	T	$am_l^{\rm sea}$	$am_s^{\rm sea}$	$am_c^{\rm sea}$
3	5.8	1.1367(5)	36	48	997	16	9, 12, 15, 18	0.00235	0.0647	0.831
8	6.0	1.4149(6)	48	64	998	16	12, 15, 18, 21	0.00184	0.0507	0.628
11	6.0	1.9518(7)	64	96	660	8	16, 19, 22, 25	0.00120	0.0363	0.432

Table 5.2: The bare masses of the valence quarks and "Naik" ϵ for the c-quarks [128, 129] for the configurations used in this calculation. The valence light quark mass $am_l^{\rm val}$ is taken to be the same as $am_l^{\rm sea}$ whereas $am_s^{\rm val,tuned}$ is obtained by tuning the valence strange quark mass [127] to give the mass of the η_s meson to be 0.6885(22) GeV [127]. We get the tuned valence charm quark mass $am_c^{\rm val,tuned}$ by tuning the mass of the η_c meson $m_{\eta_c} = 2.9863(27)$ GeV [127].

Set	L_s/a	L_t/a	$am_l^{\rm val}$	$am_s^{\rm val,tuned}$	$am_c^{\rm val,tuned}$	ϵ
3	36	48	0.00235	0.0678	0.8605	-0.1162
8	48	64	0.00184	0.0527	0.643	-0.2336
11	64	96	0.0012	0.036	0.432	-0.1162

The adjustable parameters in this calculation are the bare valence quark masses and the ϵ parameter for HISQ [17] to improve the "Naik" term (ϵ_N) for charm quarks. The valence light quark mass $am_l^{\rm val}$ is taken to be the same as $am_l^{\rm sea}$ whereas $am_s^{\rm val,tuned}$ is obtained by tuning the valence strange quark mass [127] to give the mass of the η_s meson to be 0.6885(22) GeV [127]. We tuned the valence charm quark mass $am_c^{\rm val,tuned}$ to get the mass of the η_c meson $m_{\eta_c} = 2.9863(27)$ GeV [127]. ϵ vanishes rapidly for decreasing masses of the quarks, therefore is taken as zero for the light and strange quarks. For heavier charm quarks ϵ is given by

$$\epsilon = \epsilon_N - 1 = \frac{(4 - \sqrt{(}4 + 12 \times m_{\rm tree}/(\cosh(m_{\rm tree}) \times \sinh(m_{\rm tree}))))}{(\sinh(m_{\rm tree}))^2} - 1. \quad (5.33)$$

Here, "$m_{\rm tree}$" is the tree level quark mass given by

$$\begin{aligned} m_{\rm tree} &= [1 - (3.0/80.0) \times m_c^4 + (23/2240) \times m_c^6 \\ &\quad +(1783/537600) \times m_c^8 - (76943/23654400) \times m_c^{10}]m_c. \end{aligned} \quad (5.34)$$

The values for these adjustable parameters in our calculation are listed in Table 5.2

The inversion for the strange propagators for each of the $\vec{p}_K$s is the most expensive part of this calculation as the used zero momentum light propagators were previously generated by Rachel Dowdall for a separate project. While generating charm propagators the stopping condition (using the relative error instead of the absolute errors in the

CG method) has been tested using the "truncated solver" method to achieve the convergence.

5.5 Fits and data analysis

The two point heavy-light D and K meson correlators have the fit forms described in equation 2.46. The ground state probability of the D/K meson is extracted as

$$(a_o^D)^2 = \frac{|\langle 0|\chi_D|D\rangle|^2}{2M_D a^3}$$
$$(a_o^K)^2 = \frac{|\langle 0|\chi_K|K\rangle|^2}{2M_K a^3}. \tag{5.35}$$

Here, χ_D and χ_K are the interpolating operators for the D and the K mesons respectively; a is the lattice spacing.

The three-point correlators (for both the scalar and vector currents) have oscillations at both ends and can be written as in equation 2.47.

Here, we have taken $0 \leq t \leq T$ and $T \ll L_t$ such that any contributions from the meson propagating in the opposite direction from the boundary due to the periodic boundary condition can be neglected. Otherwise, it will tremendously complicate the fit form of the three-point correlator.

We use Bayesian fitting methods [65] to simultaneously fit the two-point and three-point correlators for multiple Ts with all correlations among errors taken into account to extract the three-point amplitude V^{nn}. Since using all T values does not increase the number of fit parameters, but increases the amount of data, we get much better statistics from simultaneous fitting and much more precise ground state observables for the mesons. We use both even and odd T values which further improves the fit uncertainties.

Here, the scalar current amplitude is

$$\langle K|S|D\rangle = 2\sqrt{M_D E_K} V_{00}^{\mathrm{nn,scalar}}. \tag{5.36}$$

And the vector current amplitude is given by

$$\langle K|V|D\rangle = Z_V \times 2\sqrt{M_D E_K} V_{00}^{\mathrm{nn,vector}}. \tag{5.37}$$

And using equations 5.36 and 5.10 we extract $f_0(q^2)$. Putting the values of $f_0(q^2)$ and Z_V in equation 5.9 we can extract $f_+(q^2)$.

For the first sum in equation 2.46 (and for $\vec{p}_K = \vec{0}$) we have used the priors as (energy in the units of GeV)

$$\begin{aligned}
\log(E^K_{(0)}) &= \log(0.48(5)) \\
\log(E^K_{(n)} - E^K_{(n-1)}) &= \log(0.40(20)) \quad (n > 0) \\
a^K_{(0)} &= 0.01(1.0) \\
\log(E^D_{(0)}) &= \log(1.80(18)) \\
\log(E^D_{(n)} - E^D_{(n-1)}) &= \log(0.40(20)) \quad (n > 0) \\
a^D_{(0)} &= 0.01(1.0).
\end{aligned} \tag{5.38}$$

The notation is the same as used in the previous chapters. We have assigned analogous priors for the second sum as well, but with

$$\log(Eo^{D/K}_{(0)}) = \log(E^D/K_{(0)} + (0.23, 0.12)). \tag{5.39}$$

For the three point amplitudes we assign

$$\begin{aligned}
V^{nn}_{\mathrm{scalar}} &= 0.01(5.0), V^{on}_{\mathrm{scalar}} = 0.01(15.0) \\
V^{no}_{\mathrm{scalar}} &= 0.01(15.0), V^{oo}_{\mathrm{scalar}} = 0.01(15.0) \\
V^{nn}_{\mathrm{vector}} &= 0.01(10.0), V^{on}_{\mathrm{vector}} = 0.01(10.0) \\
V^{no}_{\mathrm{vector}} &= 0.01(10.0), V^{oo}_{\mathrm{vector}} = 0.01(10.0).
\end{aligned} \tag{5.40}$$

The energy priors for other kaon momenta $\vec{p}_K$ are given following the dispersion relation $E^2 = \vec{p}_K^2 + m^2$.

The time range I have used for fitting two-point correlators is $[t_{\mathrm{min}}, L_t - t_{\mathrm{min}}]$, where t_{min} for very coarse, coarse and fine lattices are $3, 4$ and 5 respectively. To fit the three point correlators on very coarse, coarse and fine lattices I have used time ranges $[3, T-3]$, $[4, T-4]$ and $[6, T-6]$ respectively. The fits are generally consistent within a range of t_{min} values.

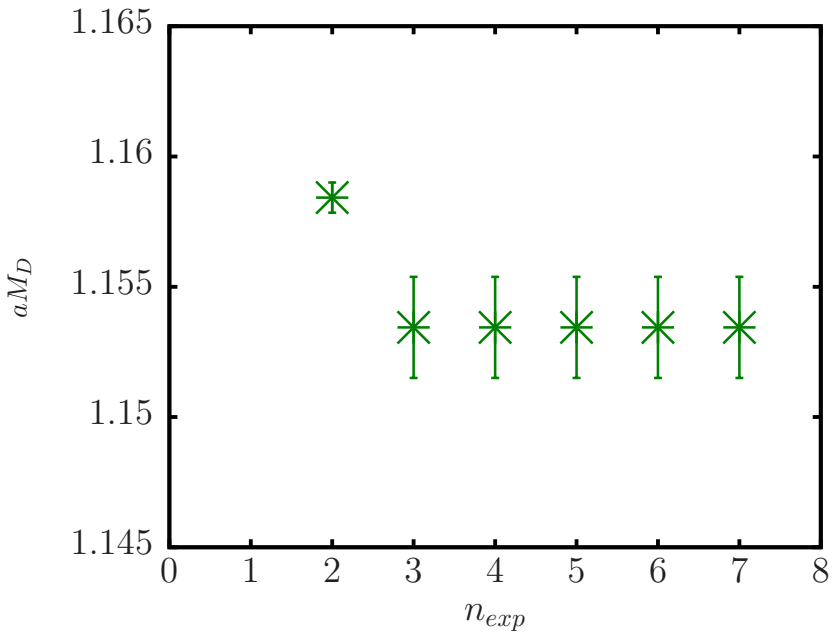

Figure 5.3: M_D vs. $n_{\rm exp}$ plot on the coarse lattice.

5.6 Results

In this calculation for each ensemble I have first run the $q^2_{\rm max}$ jobs while I have also generated the zero momentum D and K two-point correlators. I have extracted the meson properties like masses, decay constants separately from only two-point fits and from simultaneous fits of two-point and $q^2_{\rm max}$ three-point correlators. As discussed before, the simultaneous fits give much better precision in the ground state meson properties and the final results are taken from these fits.

While extracting meson ground state properties, I have fitted starting from number of exponentials $n_{\rm exp} = 2$ up to $n_{\rm exp} = 7$ to get a stable fit with a $\chi^2/{\rm dof} < 1$. For the D and K meson properties, I have achieved this from the 3rd exponential fits and hence, this value is taken as our result. The behaviour of these results with number of exponentials is shown in Table 5.3 and Figures 5.3 and 5.4.

This huge number (~ 200) of parameters are sometimes difficult to fit using the simultaneous fitting. Therefore I have also tested with sequential fitting where the

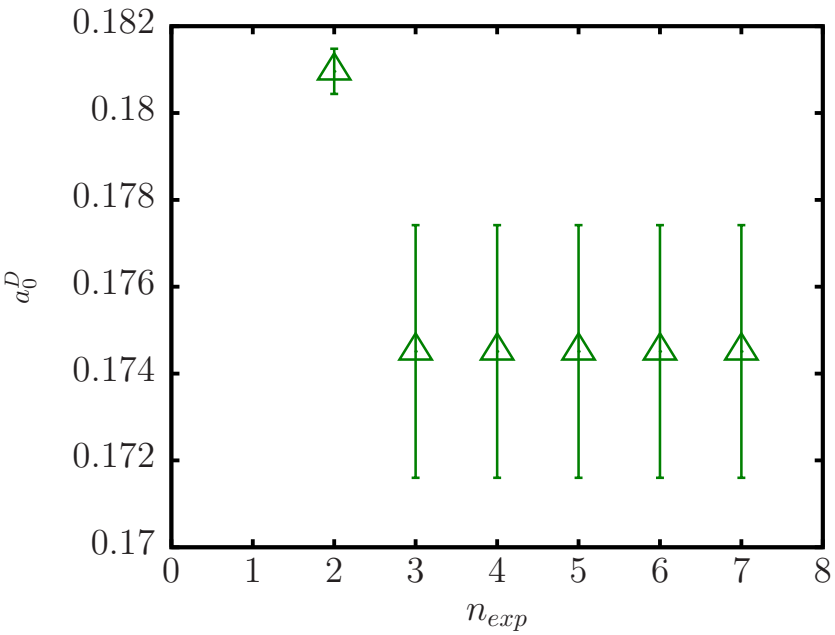

Figure 5.4: a_0^D vs. $n_{\rm exp}$ plot on the coarse lattice.

two-point results are fed as priors to the three-point fits and thus give better stability with much less difficulty. The results extracted from both types of fits are consistent with each other.

The results for the masses, ground state amplitudes and the decay constants of the Goldstone and the non-Goldstone D mesons used in my calculation and of the K meson are listed in Tables 5.4 and 5.5.

Note that the vector current renormalisation factor Z_V is independent of the momentum of the spectator quarks and sea quark masses as shown in [35].

From the $q^2_{\rm max}$ three-point correlators, only $f_0(q^2)$ has been extracted as under this condition the term containing $f_+(q^2)$ in equation 5.7 gets cancelled. As q^2 becomes smaller, the kaon energy E_K gets higher, since in the D meson rest frame

$$q^2 = M_D^2 - M_K^2 - 2M_D E_K \tag{5.41}$$

with $q^2_{\rm max} = (M_D - M_K)^2$ and physical region $q^2_{\rm max} \geq q^2 \geq 0$. Covering this whole physical region of q^2 I have set three more q^2 values and calculated the scalar and vector form factors at these q^2 values. The values of q^2 we aimed for, the momentum

Table 5.3: This table shows the results for $aM_{D,\text{Gold}}$, aM_K, $a_0^{D,\text{Gold}}$ and a_0^K with increasing number of exponentials n_{exp} in the two-point correlator fit on the configuration set '8'. The results become stable from the 3rd exponential fit. The results are extracted from simultaneous two-point and q^2_{max} three-point correlator fits.

n_{exp}	$aM_{D,\text{Gold}}$	aM_K	$a_0^{D,\text{Gold}}$	a_0^K
2	1.15842(17)	0.30438(4)	0.18096(52)	0.20881(5)
3	1.15416(27)	0.30399(5)	0.17451(291)	0.20805(7)
4	1.15416(27)	0.30399(5)	0.17451(291)	0.20805(7)
5	1.15416(27)	0.30399(5)	0.17451(291)	0.20805(7)

Table 5.4: Results for the masses - $aM_{D,\text{Gold}}$, $aM_{D,\text{nongold}}$, aM_K; amplitudes - $a_0^{D,\text{Gold}}$, $a_0^{D,\text{nongold}}$, a_0^K; decay constants - $af^{D,\text{Gold}}$, $af^{D,\text{nongold}}$, af^K and the vector current renormalisation Z_V taken from the 3rd exponential of simultaneous fits of two-point and q^2_{max} three-point correlators; here, $\vec{p}_K = \vec{0}$.

Set	$aM_{D,\text{Gold}}$	$aM_{D,\text{nongold}}$	aM_K	$a_0^{D,\text{Gold}}$	$a_0^{D,\text{nongold}}$	a_0^K	$af^{D,\text{Gold}}$	$af^{D,\text{nongold}}/Z_A$	af^K	Z_V
3	1.44869(72)	1.45307(89)	0.37912(8)	0.23731 (101)	0.13330 (191)	0.28087 (13)	0.16604(58)	0.15642(211)	0.11936(3)	1.0442(75)
8	1.15416(27)	1.15649(45)	0.30400(5)	0.17583(28)	0.09456(38)	0.20808(7)	0.12932(18)	0.12435(48)	0.09821(2)	1.0120(50)
11	0.83220(27)	0.83264(36)	0.21867(6)	0.11511(24)	0.06000(21)	0.13450(11)	0.09289(16)	0.09299(32)	0.06920(3)	1.0265(46)

Table 5.5: Results for the masses (in GeV)- $aM_{D,\text{Gold}}$, $aM_{D,\text{nongold}}$, aM_K; amplitudes - $a_0^{D,\text{Gold}}$, $a_0^{D,\text{nongold}}$, a_0^K; and decay constants (in GeV)- $af^{D,\text{Gold}}$, $af^{D,\text{nongold}}$, af^K taken from the 3rd exponential of simultaneous fits of two-point and q^2_{max} three-point correlators; here, $\vec{p}_K = \vec{0}$.

Set	$M_{D,\text{Gold}}$ (GeV)	$M_{D,\text{nongold}}$(GeV)	M_K (GeV)	$f^{D,\text{Gold}}$ (GeV)	$f^{D,\text{nongold}}$ (GeV)	f^K (GeV)
3	1.89471(95)	1.90045(117)	0.49585(10)	0.21716(76)	0.20455(275)	0.15612(4)
8	1.87895(44)	1.88274(73)	0.49490(8)	0.21052(30)	0.20244(79)	0.15989(8)
11	1.86890(61)	1.86987(81)	0.49108(14)	0.20860(36)	0.20884(72)	0.15541(9)

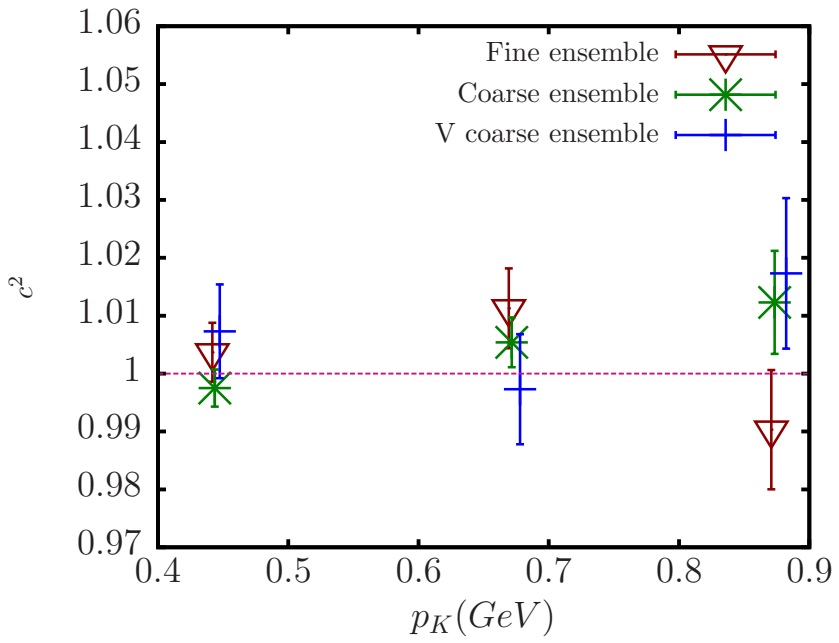

Figure 5.5: Check for relativistic dispersion relation on all lattice ensembles: the square of the speed of light in free space c^2 vs. the kaon momentum $\vec{p}_K$.

twists applied in the MILC code, the kaon momenta and energies generated from these using twisted boundary conditions and the amplitudes of these states are given in Table 5.6.

From this calculation I have tested the relativistic dispersion relation as it is only approximate on the lattice. We check the deviation of the square of the velocity of light

$$c^2(\vec{p}) = \frac{E_K^2(\vec{p}) - M_K^2}{\vec{p}^2} \tag{5.42}$$

from 1 for different kinematics and on all ensembles.

Generally, on the lattice we expect to get violations $\mathcal{O}(\alpha_S(pa)^2)$. Table 5.6 and Figure 5.5 show that in my calculation the relativistic dispersion relation is violated by $1-2\%$ which is within our expectation. However the statistical uncertainties increase in the fitted results for the kaon energies with non-zero momenta.

As we progress towards the $q^2 = 0$ limit, the kaon two-point correlators and the three-point correlators get noisier. Therefore, fitting them smoothly is often a

Table 5.6: This table gives the values of the momenta we fed as inputs- q^2, the square of the lattice kaon momenta $(ap_k)^2$ and the momentum twists applied. We also list the kaon energy aE_K and its amplitude a_0^K. We test the relativistic dispersion relation by looking at the square of the velocity of light c^2 and its deviation from 1.

Set	q^2 (GeV)^2	Momentum twist	$(ap_k)^2$	c^2	aE_K	a_0^K
3	1.95684	(0,0,0)	0	-	0 0.37912(8)	0.28089(14)
	1.30456	(2.013,2.013,2.013)	0.11705	1.0073(81)	0.51234(12)	0.24733(28)
	0.65228	(3.05,3.05,3.05)	0.26871	0.9973(95)	0.64109(18)	0.21334(39)
	0.0053	(3.969,3.969,3.969)	0.45503	1.0173(130)	0.77399(28)	0.20272(55)
8	1.91560	(0,0,0)	0	-	0.30400(5)	0.20808(7)
	1.27707	(2.405,2.405,2.405)	0.07426	0.9975(32)	0.40781(8)	0.16318(11)
	0.63853	(3.641,3.641,3.641)	0.17019	1.0054(43)	0.51425(13)	0.17941(21)
	0.002	(4.735,4.735,4.735)	0.28783	1.0123(89)	0.62339(19)	0.14951(31)
11	1.89839	(0,0,0)	0	-	0.21867(6)	0.13450(9)
	1.26559	(2.315,2.315,2.315)	0.03870	1.0036(51)	0.29461(10)	0.11990(12)
	0.63280	(3.507,3.507,3.507)	0.08882	1.0113(69)	0.37236(14)	0.11165(23)
	0.0007	(4.563,4.563,4.563)	0.15036	0.9903(103)	0.44190(22)	0.10362(37)

Table 5.7: Results for the scalar from factor $f_0(q^2)$, vector form factor $f_+(q^2)$ with q^2 values on different ensembles from simultaneous fits of the two-point and three point correlators.

Set	q^2 (GeV)^2	$f_0(q^2)$	$f_+(q^2)$
3	1.956844912	1.0371(59)	-
	1.304563275	0.9185(86)	1.2144(119)
	0.652281637	0.8250(182)	0.9242(220)
	0.0053	0.7323(323)	0.7331(358)
8	1.91559907	1.0195(23)	-
	1.277066047	0.9037(43)	1.1867(127)
	0.638533023	0.8391(95)	0.9975(62)
	0.002	0.7442(182)	0.7463(213)
11	1.898390079	1.0130(40)	-
	1.265593386	0.9511(82)	1.2042(101)
	0.632796693	0.8491(113)	0.9762(131)
	0.0007	0.7513(215)	0.7521(248)

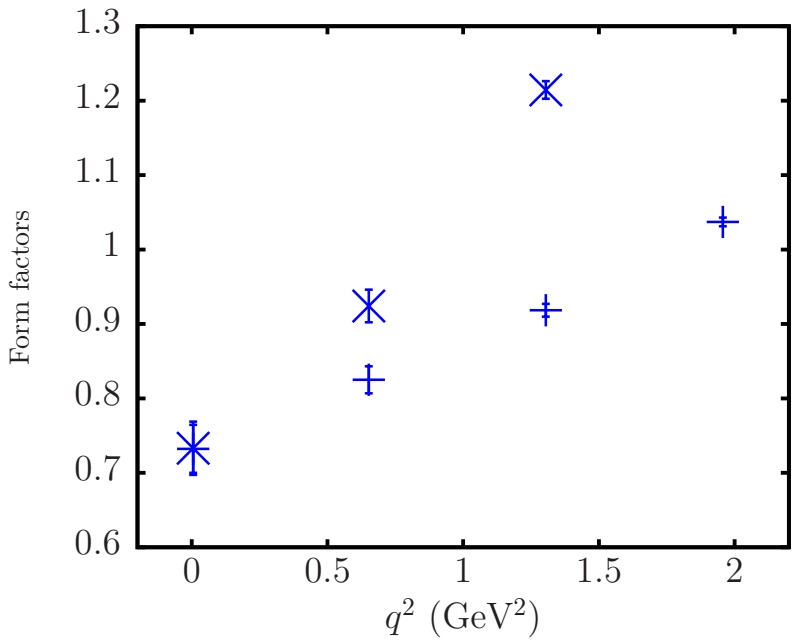

Figure 5.6: This plot shows the q^2 dependence of the form factors $f_0(q^2)$ and $f_+(q^2)$ with q^2 on the very coarse lattice. The blue crosses represent $f_+(q^2)$ values and the blue pluses show the values for $f_0(q^2)$.

challenge, especially for the fine lattice and some tricks need to be applied. I have tested several techniques - binning of data, using a shorter fit time range, fitting different number of Ts, skipping few time slices, increasing svdcut up to 10^{-5} and obtained the optimum fits with acceptable precision.

The scalar and vector form factors are extracted from the simultaneous fits of all data - including two-point and three-point correlators for all q^2 values on each ensemble. Generally the vector current is noisier and hence the vector form factor $f_+(q^2)$. The results for the form factors are listed in Table 5.7 and their q^2 dependence is shown in Figures 5.6, 5.7, 5.8 and 5.9.

We can now perform the continuum extrapolation on $f_0(q^2)$ and then extract V_{cs} using the experimental decay rate which is equal to $f_0(q^2 = 0) \times |V_{cs}|$. Note that we have $f_0(q^2 = 0) = f_+(q^2 = 0)$. I have used $f_0(q^2 = 0)$ instead of $f_+(q^2 = 0)$ since it is less noisy. In future I intend to use $f_+(q^2)$ directly and calculate V_{cs} for every q^2

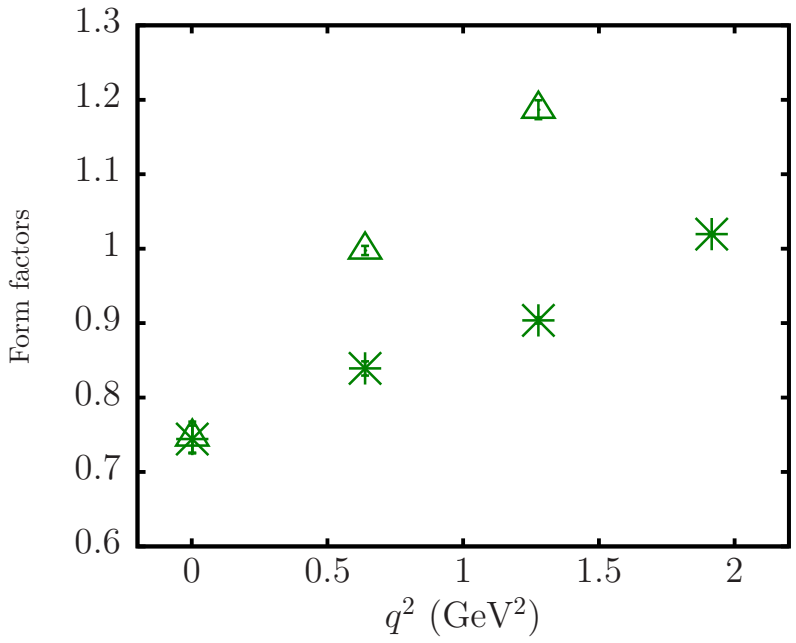

Figure 5.7: This plot shows the q^2 dependence of the form factors $f_0(q^2)$ and $f_+(q^2)$ with q^2 on the coarse lattice. The green triangles represent $f_+(q^2)$ values and the green stars show the values for $f_0(q^2)$.

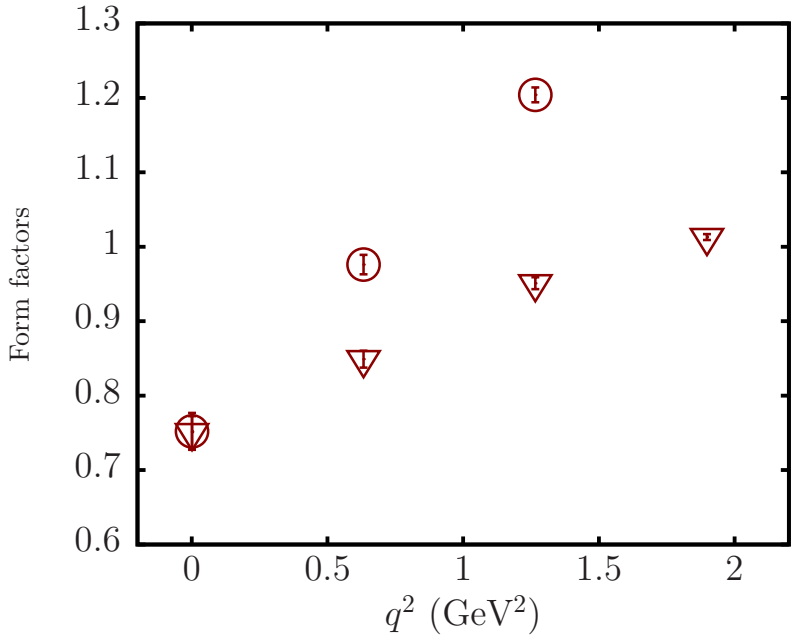

Figure 5.8: This plot shows the q^2 dependence of the form factors $f_0(q^2)$ and $f_+(q^2)$ with q^2 on the fine lattice. The red circles represent $f_+(q^2)$ values and the red triangles show the values for $f_0(q^2)$.

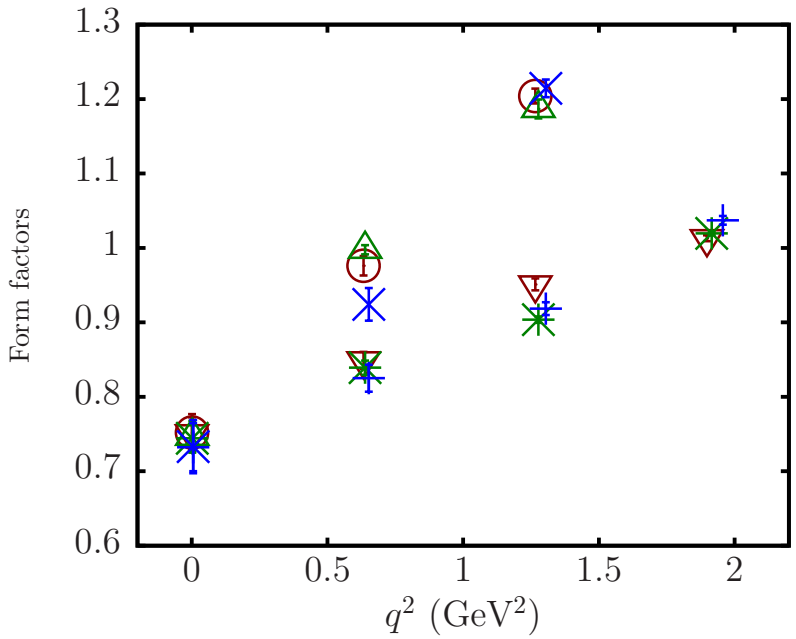

Figure 5.9: This plot shows the q^2 dependence of the form factors $f_0(q^2)$ and $f_+(q^2)$ with q^2 on all the lattice ensembles together. The red circles represent $f_+(q^2)$ values and the red triangles show the values for $f_0(q^2)$ on the fine lattice; the green triangles represent $f_+(q^2)$ values and the green stars show the values for $f_0(q^2)$ on the coarse lattice; and the blue crosses represent $f_+(q^2)$ values and the blue pluses show the values for $f_0(q^2)$ on the very coarse lattice.

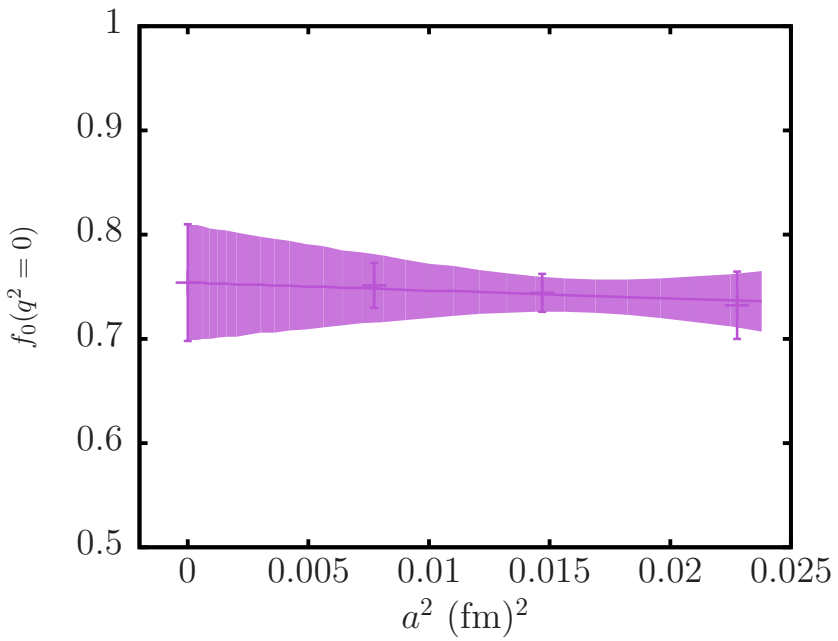

Figure 5.10: $f_0(q^2 = 0)$ vs. the square of the lattice spacing: continuum extrapolation to $a = 0$ of $f_0(q^2 = 0)$.

experimental bin. Figure 5.10 shows the extrapolation of the $f_0(q^2 = 0)$ against the square of the lattice spacing to the continuum limit $a = 0$. From the values of the scalar form factors at $q^2 = 0$ on three different lattice spacings, we are able to make a smooth continuum extrapolation with the fit form for the HISQ action

$$f = c_0 + c_l \times m_{ls} + c_s \times \Delta m_{\eta_s} + c_2 \times (\lambda a)^2 + c_4 \times (\lambda a)^4 + c_6 \times \mathcal{O}(\lambda a)^6).. \quad (5.43)$$

Here, the fit parameters are the coefficients c_0, c_l, c_s, c_2, c_4, and c_6. The fit form (in powers of lattice spacing) replicates the form of the discretised action. For example, in this case there are no odd powers of the lattice spacing in the fit function as HISQ action does not contain them. Also, in the fit results we can find c_2 is negligibly small as the HISQ action is $\mathcal{O}(a^2)$-improved. λ is the relevant QCD scale in our calculation which has been taken between $200 - 400$ MeV to get the best fit. The prior for c_0 has been taken as 0.24(12) and for the rest of the coefficients in equation 3.41 the priors were taken as 0(1). The best fit results have been obtained with a $\chi^2 = 0.3 - 1.1$ and p-value of $0.2 - 0.8$.

Here,

$$m_{ls} = \frac{((2 \times m_l^{\rm sea} + m_s^{\rm sea}) - (2 \times m_l^{\rm phys} + m_s^{\rm phys}))}{m_s^{\rm phys}}; \quad (5.44)$$

$$\Delta m_{\eta_s} = m^2_{\eta_s,{\rm phys}} - m^2_{\eta_s,{\rm obtained}}. \quad (5.45)$$

The term 'm_{ls}' in the fit corrects for the heavier than physical sea light quark mass effects and the term 'Δm_{η_s}' corrects for the valence s quark mass mistuning effects (difference from the physical mass), though they are very small.

We extract the continuum results for the $f_0(q^2 = 0)$ to be 0.754(56) which is also taken to be the value of $f_+(q^2 = 0)$ and is consistent with references [35, 125].

We use the experimental input $f_+(q^2 = 0) \times |V_{cs}| = 0.719(8)$ from CLEO-c [130]; $f_+(q^2 = 0) \times |V_{cs}| = 0.717(10)$ from BaBar [123]. We take their average as $f_+(q^2 = 0) \times |V_{cs}| = 0.718(8)$ and finally calculate $|V_{cs}|$ to be 0.952(46) which is consistent with reference [35].

In future, to get better precision I will increase the statistics on the finer lattices. Also, I will compare the form factors with each q^2 experimental bin and use a Z-expansion following the reference [35].

Chapter 6

Conclusion and Outlook

In this dissertation, I have calculated some phenomenologically important quantities in the Standard Model using the first principle non-perturbative methods of lattice QCD. These quantities involve some crucial tests of the Standard Model to find any hint of new physics beyond it.

Following a brief introduction to the subject in Chapters 1 and 2, in Chapter 3, I have discussed about the pseudoscalar and the vector mesons made from the strange quark-antiquark pairs. The highlight of this chapter is my results for the mass and decay constants of the vector meson ϕ which are the most accurate results to date. I have not considered the quark-line disconnected contributions here since they are very small. It is supported by the fact that our results for the physical dynamical light quark masses perfectly match with the experimental results for m_ϕ and f_ϕ. Furthermore, I have calculated the local temporal axial current and the local vector current renormalisation constants completely nonperturbatively with 0.1% uncertainty on the fine lattice. I have confirmed that the Fermilab formalism [61] for calculating the axial vector current in the mixed perturbative-nonperturbative method is robust. This chapter also includes my results on the comparison of the discretisation errors between the HISQ and clover formalisms from their approach to

the continuum for the ϕ meson mass and decay constant. As expected, the calculation showed that the HISQ action has much smaller discretisation compared to the clover action [59].

In Chapter 4, along with my collaborators, I have developed a new lattice QCD method to calculate the hadronic vacuum polarisation (HVP) contribution to the anomalous magnetic moment of the muon, a_μ [95]. We have achieved an unprecedented uncertainty of $\sim$ 2% in the total HVP contributions to a_μ [74]. Our result for $a_\mu^{\rm HVP,LO}$ is the first lattice calculation to include the effects of the $N_f = 2+1+1$ HISQ dynamical quarks at their physical masses and, at the same time, to take the finite volume effects and other systematics into account. Although we have made a significant progress in this, we have not yet achieved the precision comparable to the semi-phenomenological results of $a_\mu^{\rm HVP,LO}$ ($\sim 1\%$). However, the spread between different non-lattice results is of the same size as the uncertainty in our lattice result. We obtain a 3.5σ deviation in our result of $a_\mu^{\rm HVP,LO}$ from that we expect in the absence of any new physics beyond the Standard Model. However, before we can conclude if there is a new physics effect we would have to increase the precision comparable to the experimental precision. In future, in collaboration with the MILC we are going to use a larger ensemble size ($10,000$ on ~ 0.15 fm lattice with physical dynamical light quark mass) to improve the statistical uncertainty in the light quark connected pieces. We also need to understand the ρ meson better on the lattice which can be done by using larger volume and finer lattices at the physical mass of the dynamical light quark. This requires $\sim$ 7 fm lattice to reduce the finite volume effects below 1% for the continuum $\pi\pi$ contribution. Moreover, we have to achieve an improved precision in the disconnected diagrams using an improved algorithm on MILC lattices and to calculate the QED and isospin corrections.

In Chapter 5, I have studied the $D \to Kl\nu$ semileptonic meson decay and calculated its scalar and vector form factors over the whole physical q^2 region covering the $q^2 = 0$

point. Combining the vector form factor at the $q^2 = 0$ with the experimental decay rate I have found the central CKM matrix element $|V_{cs}|$ as 0.9523(500) which is consistent with [35]. For this calculation I have used the kinematic relation that the vector and scalar form factors at $q^2 = 0$ are equal and extracted the continuum limit of the scalar form factor after a continuum extrapolation. Though within the scope of my present calculation I have not achieved the level of precision in the $|V_{cs}|$ similar to that quoted in [35], my $D \to Kl\nu$ form factor calculation is the first to have been performed on the $N_f = 2 + 1 + 1$ HISQ MILC ensembles with the physical light quark masses covering the full physical q^2 region. In future, instead of using the $f_0(q^2 = 0)$ to extract $f_+(q^2 = 0)$, I will use the $z-$ expansion to extract $|V_{cs}|$ from all the experimental q^2 bins with bin-to-bin correlations taken into account, following [35]. Also, using the statistics on the fine lattices I will be able to increase the precision in our result as it is mainly dictated by the fine lattices due to the very small discretisation in the HISQ action. Moreover, my ongoing calculation also includes heavier dynamical light quark masses in the simulation to test the light quark mass effects.

Bibliography

[1] H. J. Rothe, *Lattice gauge theories: An introduction* (World Sci. Lect. Notes Phys. 74, 2005).

[2] C. Gattringer and C. Lang, *Quantum chromodynamics on the lattice - an introductory presentation* (Springer Lect. Notes Phys. 788, 2009).

[3] T. DeGrand and C. DeTar, *Lattice methods for quantum chromodynamics* (World Sci., 2006).

[4] M. Creutz, *Quarks, gluons and lattices* (Cambridge Monogr. Math. Phys., 1984).

[5] I. Montvay and G. Münster, *Quantum fields on a lattice* (Cambridge Monogr. Math. Phys., 1994).

[6] R. Gupta, Probing the standard model of particle interactions. Proceedings, Summer School in Theoretical Physics, NATO Advanced Study Institute, 68th session, Les Houches, France, July 28-September 5, 1997. Pt. 1, 2 .

[7] G. P. Lepage, Strong interactions at low and intermediate energies. Proceedings, 13th Annual Hampton University Graduate Studies, HUGS'98, Newport News, USA , 49 (1998), hep-lat/0506036.

[8] C. Davies, Lattice QCD: A Guide for people who want results, in *Proceedings, 58th Scottish Universities Summer School in physics, SUSSP58, St. Andrews, UK, August 22-28, 2004*, pp. 233–272, 2005, hep-lat/0509046.

[9] Fermilab Lattice and MILC Collaborations, C. Bernard *et al.*, Phys. Rev. D **83**, 034503 (2011).

[10] D. B. Kaplan, Chiral Symmetry and Lattice Fermions, in *Modern perspectives in lattice QCD: Quantum field theory and high performance computing. Proceedings, International School, 93rd Session, Les Houches, France, August 3-28, 2009*, pp. 223–272, 2009, 0912.2560.

[11] G. P. Lepage, (2005), HPQCD collaboration document.

[12] E. Follana *et al.*, Phys. Rev. D **75**, 054502 (2007).

[13] J. F. Lagae and D. K. Sinclair, Nucl. Phys. Proc. Suppl. **63**, 892 (1998), hep-lat/9709035.

[14] MILC, K. Orginos and D. Toussaint, Phys. Rev. **D59**, 014501 (1999), hep-lat/9805009.

[15] G. P. Lepage, Phys. Rev. **D59**, 074502 (1999), hep-lat/9809157.

[16] G. P. Lepage, Nucl. Phys. Proc. Suppl. **60A**, 267 (1998), hep-lat/9707026.

[17] E. Follana *et al.*, Phys. Rev. D **75**, 054502 (2007).

[18] F. Burger *et al.*, JHEP , 02099 (2013), 1308.4327.

[19] G. Donald, *Semileptonic and radiative meson decays from lattice QCD with improved staggered fermions*, PhD thesis, University of Glasgow, 2013.

[20] B. Colquhoun, *Bottomonium and B Physics with Lattice NRQCD b Quarks*, PhD thesis, University of Glasgow, 2015.

[21] S. Meinel, *Heavy quark physics on the lattice with improved nonrelativistic actions*, PhD thesis, University of Cambridge, 2009.

[22] MILC Collaboration, A. Bazavov *et al.*, Phys. Rev. D **87**, 054505 (2013).

[23] I. T. Drummond, A. Hart, R. R. Horgan, and L. C. Storoni, Phys. Rev. **D66**, 094509 (2002), hep-lat/0208010.

[24] S. Borsanyi *et al.*, JHEP **1209**, 010 (2012), 1203.4469.

[25] HPQCD Collaboration, R. Dowdall, C. Davies, G. Lepage, and C. McNeile, Phys.Rev. **D88**, 074504 (2013), 1303.1670.

[26] HPQCD Collaboration, R. J. Dowdall *et al.*, Phys. Rev. D **85**, 054509 (2012).

[27] HPQCD Collaboration, R. Dowdall, C. Davies, G. Lepage, and C. McNeile, Phys.Rev. **D88**, 074504 (2013), 1303.1670.

[28] HPQCD collaboration, G. C. Donald, C. T. H. Davies, E. Follana, and A. S. Kronfeld, Phys. Rev. D **84**, 054504 (2011), 1106.2412.

[29] A. S. Kronfeld, PoSLAT **2007**, 016 (2007), 0711.0699.

[30] J. Nazareth, Wiley Interdisciplinary Reviews: Computational Statistics **1**, 348 (2009).

[31] HPQCD Collaboration, C. Davies, E. Follana, I. Kendall, G. P. Lepage, and McNeile, Phys.Rev. **D81**, 034506 (2010), 0910.1229.

[32] I. Kendall, PhD thesis, University of Glasgow, UK (2010).

[33] G. M. de Divitiis, R. Petronzio, and N. Tantalo, Phys. Lett. B **595**, 408 (2004), hep-lat/0405002.

[34] D. Guadagnoli, F. Mescia, and S. Simula, Phys. Rev. D **D**, 114504 (2006), hep-lat/0512020.

[35] J. Koponen *et al.*, (2013), arXiv:1305.1462.

[36] H. Na, C. T. H. Davies, E. Follana, G. P. Lepage, and J. Shigemitsu, Phys. Rev. D **82**, 114506 (2010), 1008.4562.

[37] F. Olness and R. Scalise, Am. J. Phys. **79**, 306 (2011), 0812.3578.

[38] S. Ying, Commun. Theor. Phys. **28**, 301 (1997), hep-ph/9506290.

[39] S. Capitani, Phys. Rept. **382**, 113 (2003), hep-lat/0211036.

[40] M. Göckeler *et al.*, The European Physical Journal C **56**, 161 (2008).

[41] G. P. Lepage *et al.*, Nucl. Phys. Proc. Suppl. **106**, 12 (2002), hep-lat/0110175.

[42] S. Schaefer, R. Sommer, and F. Virotta, PoSLATTICE **2009**, 032 (2009), 0910.1465.

[43] L. Del Debbio, H. Panagopoulos, and E. Vicari, JHEP **08**, 044 (2002), hep-th/0204125.

[44] L. Del Debbio, G. M. Manca, and E. Vicari, Phys. Lett. B **594**, 315 (2004), hep-lat/0403001.

[45] C. Aubin and C. Bernard, Phys. Rev. D **68**, 034014 (2003), hep-lat/0304014.

[46] M. Golterman, Modern perspectives in lattice QCD: Quantum field theory and high performance computing. Proceedings, International School, 93rd Session, Les Houches, France, 2009 .

[47] S. Sharpe, Workshop on Perspectives in Lattice QCD Nara, Japan, October 31-November 11, 2005 (2006), hep-lat/0607016.

[48] G. Colangelo, S. Durr, and C. Haefeli, Nucl. Phys. B **721**, 136 (2005), hep-lat/0503014.

[49] J. Gasser and H. Leutwyler, Phys. Lett. B **184**, 83 (1987).

[50] J. Gasser and H. Leutwyler, Nucl. Phys. B **307**, 763 (1988).

[51] C. Davies, PoS **LATTICE2011**, 019 (2011), 1203.3862.

[52] J. Laiho, E. Lunghi, and R. Van de Water, PoS **LATTICE2011**, 018 (2011), 1204.0791.

[53] G. P. Lepage, L. Magnea, C. Nakhleh, U. Magnea, and K. Hornbostel, Phys. Rev. D **46**, 4052 (1992), hep-lat/9205007.

[54] A. X. El-Khadra, A. S. Kronfeld, and P. B. Mackenzie, Phys. Rev. D **55**, 3933 (1997), hep-lat/9604004.

[55] R. Dowdall *et al.*, PoSLATTICE **2013**, 406 (2013), arXiv:1309.4610.

[56] C. McNeile, C. Davies, E. Follana, K. Hornbostel, and G. Lepage, Phys.Rev. **D85**, 031503 (2012), 1110.4510.

[57] J. Harada *et al.*, Phys. Rev. D **65**, 094513 (2002), hep-lat/0112044, [Erratum: Phys. Rev.D71,019903(2005)].

[58] A. X. El-Khadra, E. Gamiz, A. S. Kronfeld, and M. A. Nobes, PoSLATTICE **2007**, 242 (2007), 0710.1437.

[59] B. Chakraborty *et al.*, PoSLATTICE **2013**, 309 (2013), arXiv:1401.0669.

[60] C. Monahan, J. Shigemitsu, and R. Horgan, Phys. Rev. **D87**, 034017 (2013), 1211.6966.

[61] Fermilab Lattice and MILC Collaborations, A. Bazavov *et al.*, Phys. Rev. D **85**, 114506 (2012).

[62] HPQCD and UKQCD Collaborations, E. Follana, C. T. H. Davies, G. P. Lepage, and J. Shigemitsu, Phys. Rev. Lett. **100**, 062002 (2008).

[63] A. X. El-Khadra, E. Gamiz, A. S. Kronfeld, and M. A. Nobes, PoS **LAT2007**, 242 (2007), 0710.1437.

[64] G. P. Lepage and P. B. Mackenzie, Phys. Rev. D **48**, 2250 (1993), hep-lat/9209022.

[65] G. Lepage *et al.*, Nuclear Physics B - Proceedings Supplements **106107**.

[66] Particle Data Group, J. Beringer *et al.*, Phys. Rev. D **86**, 010001 (2012).

[67] HPQCD Collaboration, C. Davies *et al.*, PoS **ConfinementX**, 288 (2012), 1301.7203.

[68] Particle Data Group, K. A. Olive *et al.*, Chin. Phys. **C38**, 090001 (2014).

[69] Muon G-2 Collaboration, G. Bennett *et al.*, Phys.Rev. **D73**, 072003 (2006), hep-ex/0602035.

[70] T. Aoyama, M. Hayakawa, T. Kinoshita, and M. Nio, Phys.Rev.Lett. **109**, 111808 (2012), 1205.5370.

[71] K. Hagiwara, R. Liao, A. D. Martin, D. Nomura, and T. Teubner, J.Phys. **G38**, 085003 (2011), 1105.3149.

[72] B.E. Lautrup, A. Peterman and E. de Rafael, Phys. Rep. 3, N°4 (1972) 193-260.

[73] M. Davier, A. Hoecker, B. Malaescu, and Z. Zhang, Eur.Phys.J. **C71**, 1515 (2011), 1010.4180.

[74] B. Chakraborty, C. T. H. Davies, P. G. de Oliviera, J. Koponen, and G. P. Lepage, (2016), 1601.03071.

[75] A. Kurz, T. Liu, P. Marquard, and M. Steinhauser, Phys. Lett. **B734**, 144 (2014), 1403.6400.

[76] J. Prades, E. de Rafael, and A. Vainshtein, (2009), arXiv:0901.0306.

[77] C. Gnendiger, D. Stckinger, and H. Stckinger-Kim, Phys. Rev. **D88**, 053005 (2013), 1306.5546.

[78] T. Blum, S. Chowdhury, M. Hayakawa, and T. Izubuchi, Phys.Rev.Lett. **114**, 012001 (2015), 1407.2923.

[79] F. Jegerlehner and A. Nyffeler, Phys. Rept. **477**, 1 (2009), 0902.3360.

[80] RBC/UKQCD, T. Blum, M. Hayakawa, and T. Izubuchi, PoS **LATTICE2012**, 022 (2012), 1301.2607.

[81] CERN-Mainz-Daresbury, J. Bailey *et al.*, Nucl. Phys. **B150**, 1 (1979).

[82] V. Bargmann, L. Michel, and V. L. Telegdi, Phys. Rev. Lett. **2**, 435 ((1959)).

[83] R. M. Carey *et al.*, Phys. Rev. Lett. **82**, 1632 (1999).

[84] Muon (g-2) Collaboration, G. W. Bennett *et al.*, Phys. Rev. Lett. **89**, 101804 (2002).

[85] Muon (g2) Collaboration, H. N. Brown *et al.*, Phys. Rev. Lett. **86**, 2227 (2001).

[86] Muon g-2, G. Venanzoni, The New Muon g-2 experiment at Fermilab, in *Proceedings, 37th International Conference on High Energy Physics (ICHEP 2014)*, 2016, 1411.2555.

[87] Muon g-2, F. Gray, Muon g-2 Experiment at Fermilab, in *12th Conference on the Intersections of Particle and Nuclear Physics (CIPANP 2015) Vail, Colorado, USA, May 19-24, 2015*, 2015, 1510.00346.

[88] J-PARC g-'2/EDM, N. Saito, AIP Conf. Proc. **1467**, 45 (2012).

[89] B. Jäger, *Hadronic matrix elements in lattice QCD*, PhD thesis, Johhanes Gutenberg Universität,Mainz, 2014.

[90] Particle Data Group, J. Beringer *et al.*, Phys. Rev. D **86**, 010001 (2012).

[91] J. Schwinger, Phys. Rev. **73**, 416 (1948).

[92] T. Aoyama, M. Hayakawa, T. Kinoshita, and M. Nio, Phys. Rev. Lett. **109**, 111808 (2012).

[93] E. de Rafael, Phys. Lett. B, 322 (1994) 239.

[94] RBC/UKQCD, T. Blum, Phys.Rev.Lett. **91**, 052001 (2003), hep-lat/0212018.

[95] HPQCD Collaboration, B. Chakraborty *et al.*, Phys. Rev. D **89**, 114501 (2014).

[96] C. Aubin, T. Blum, M. Golterman, and S. Peris, PoS **LATTICE2012**, 176 (2012), 1210.7611.

[97] HPQCD and UKQCD Collaborations, E. Follana *et al.*, Phys.Rev. **D75**, 054502 (2007), hep-lat/0610092.

[98] MILC collaboration, A. Bazavov *et al.*, Phys.Rev. **D82**, 074501 (2010), 1004.0342.

[99] MILC Collaboration, A. Bazavov *et al.*, Phys.Rev. **D87**, 054505 (2013), 1212.4768.

[100] HPQCD Collaboration, G. Donald *et al.*, Phys.Rev. **D86**, 094501 (2012), 1208.2855.

[101] B. Colquhoun, R. J. Dowdall, C. T. H. Davies, K. Hornbostel, and G. P. Lepage, Phys. Rev. **D91**, 074514 (2015), 1408.5768.

[102] B. A. Galloway, P. Knecht, J. Koponen, C. T. H. Davies, and G. P. Lepage, PoS **LATTICE2014**, 092 (2014), 1411.1318.

[103] UKQCD Collaboration, C. R. Allton *et al.*, Phys. Rev. D **47**, 5128 (1993).

[104] C. Alexandrou, F. Jegerlehner, S. Gusken, K. Schilling, and R. Sommer, Phys. Lett. **B256**, 60 (1991).

[105] S. Gusken *et al.*, Phys. Lett. **B227**, 266 (1989).

[106] F. Jegerlehner and R. Szafron, Eur. Phys. J. **C71**, 1632 (2011), 1101.2872.

[107] B. Chakraborty *et al.*, Phys. Rev. **D93**, 074509 (2016), 1512.03270.

[108] A. Francis *et al.*, PoS **LATTICE2014**, 128 (2014), 1411.7592.

[109] J. Foley *et al.*, Comput. Phys. Commun. **172**, 145 (2005), hep-lat/0505023.

[110] J. Bulava *et al.*, A Novel algorithm for computing quark propagators for lattice hadron spectroscopy, in *Particles and fields. Proceedings, Meeting of the Division of the American Physical Society, DPF 2011, Providence, USA, August 9-13, 2011*, 2011, 1109.6614.

[111] J. M. Bulava *et al.*, Phys. Rev. **D79**, 034505 (2009), 0901.0027.

[112] Hadron Spectrum, J. J. Dudek, R. G. Edwards, P. Guo, and C. E. Thomas, Phys. Rev. **D88**, 094505 (2013), 1309.2608.

[113] T. Blum *et al.*, Phys. Rev. Lett. **116**, 232002 (2016), 1512.09054.

[114] Private communication with ETM Collaboration about their preliminary results.

[115] K. Maltman, A new strategy for evaluating the LO HVP contribution to (g2) on the lattice, talk at the 32nd International Symposium on Lattice Field Theory (Lattice 2014).

[116] RBC/UKQCD, T. Blum *et al.*, JHEP **04**, 063 (2016), 1602.01767.

[117] S. Bodenstein, C. Dominguez, and K. Schilcher, Phys.Rev. **D85**, 014029 (2012), 1106.0427.

[118] P. Boyle, L. Del Debbio, E. Kerrane, and J. Zanotti, Phys. Rev. **D85**, 074504 (2012), 1107.1497.

[119] M. Benayoun, P. David, L. DelBuono, and F. Jegerlehner, Eur. Phys. J. **C75**, 613 (2015), 1507.02943.

[120] F. Jegerlehner, EPJ Web Conf. **118**, 01016 (2016), 1511.04473.

[121] N. Cabibbo, Phys. Rev. Lett. **10**, 531 (1963), [,648(1963)].

[122] M. Kobayashi and T. Maskawa, Prog. Theor. Phys. **49**, 652 (1973).

[123] C. Aubin *et al.*, Phys. Rev. Lett. **94**, 011601 (2005).

[124] ETM, S. Di Vita *et al.*, PoSLATTICE **2010**, 301 (2010), 1104.0869.

[125] LATTICE-FERMILAB, LATTICE-MILC, T. Primer *et al.*, (2015), 1511.04000.

[126] R. Gupta, T. Bhattacharya, and D. Daniel, (1993), hep-lat/9310007.

[127] HPQCD Collaboration, B. Chakraborty *et al.*, Phys.Rev. **D89**, 114501 (2014), 1408.4169.

[128] S. Naik, Nucl. Phys. B **316**, 238 (1989).

[129] G. P. Lepage, Phys. Rev. D **59**, 074502 (1999).

[130] D. Besson *et al.*, Phys. Rev. D **80**, 032005 (2009).